Generation and Characterization of Topologically Structured Waves

by

Hugo Larocque

Thesis submitted to the
Faculty of Graduate and Postdoctoral Studies
In partial fulfillment of the requirements
For the degree of
Master of Science in Physics

Ottawa-Carleton Institute of Physics
Department of Physics
University of Ottawa

Abstract

This thesis covers a set of works pertaining to the generation and the characterization of structured waves defined by exotic topologies. It first presents a method to fabricate devices that can be used to arbitrarily shape the wavefronts of optical waves by means of a geometric phase. These devices can be used to shape the transverse polarization pattern of a light beam as well. Two new extensions to characterization schemes known as orbital angular momentum (OAM) sorters are then introduced and demonstrated. The first extension consists of a sorting scheme able to characterize both the OAM and the polarization content of an optical wave. As demonstrated, this feature could be of use in high-dimensional quantum cryptography. The other extension consists of an OAM sorter for electron waves whose use in materials science is also demonstrated by employing it to characterize a magnetic structure. A proposal on how to measure the OAM carried by an electron by minimally perturbing it is also discussed. The thesis then moves on towards works describing more exotic types of structured waves. On one hand, it explores the stability of space-varying polarized light beams upon propagation through a nonlinear medium. Namely, their propagation is found to be more stable than what is experienced by beams with phase singularities. On the other hand, the effect of twisting a neutron's wavefunction is also explored and is suggested to affect some of its electromagnetic properties. Finally, a method used to knot the transverse polarization profile of optical beams is presented. The structure of these optical polarization knots is then accurately characterized to reconstruct some of its topological features.

Résumé

Cette thèse prśente un ensemble de méthodes présentant ou démontrant la capacité de caractériser les propriétés topologiques d'ondes possédant des structures exotiques. D'abord, une méthode pour la fabrication de dispositifs pouvant arbitrairement modifier les fronts d'onde optiques est présentée. Ces dispositifs peuvent aussi modifier le profil adopté par la composante transversale de la polarisation d'un faisceau lumineux. Deux nouvelles extensions d'une méthode connue sous le nom de trieur de moment cinétique orbital (MCO) sont ensuite présentées et par la suite démontrées. La première extension est une méthode pouvant trier les composantes du MCO et de la polarisation d'une onde optique. Comme démontré, cet atout pourrait être utile en cryptographie quantique. L'autre extension est un trieur de MCO pour une onde d'électrons. Sa commodité en science des matériaux est ensuite démontrée en l'utilisant pour caractériser une structure magnétique. Une méthode proposant la mesure du MCO d'une onde d'électron sans la perturber significativement est aussi discutée. Par la suite, des ouvrages concernant des ondes plus exotiques sont présentés. D'un côté, la stabilité de faisceaux lumineux ayant des singularités de polarisation dans un milieu non linéaire est examinée. Cette étude démontre que ces structures optiques sont plus stables dans un milieu non linéaire que des faisceaux lumineux ayant des singularités de phase. De l'autre côté, l'effet d'ajouter des fronts d'onde hélicoïdaux à une onde de neutrons est aussi discuté et suggère que cela affecte ses propriétés électromagnétiques. Enfin, une méthode pour nouer le profil adopté par la polarisation transversale d'une onde optique est présentée. La structure adoptée par ces noeuds optiques est ensuite caractérisée pour reconstruire quelques-uns de ses attributs topologiques.

Acknowledgements

I wish to thank my supervisor Prof. Ebrahim Karimi who has continuously supported and pushed me throughout my Master's studies by providing me with numerous opportunities to grow as a scientist. I also wish to thank professor Robert Boyd who has played an integral role in all of the works presented in this thesis.

I acknowledge the financial support of the Natural Sciences and Engineering Research Council of Canada (NSERC), of the Ontario Graduate Scholarship program (OGS), and of the Canada Research Chairs (CRC) program.

I would like to thank Frédéric Bouchard for providing his invaluable knowhow on numerous occasions, especially when I first joined Prof. Karimi's SQO group. Most of these works in this thesis would not have been possible without him. I also thank Jérémie Gagnon-Bischoff, Dominic Mortimer, and Aazad Abbas, three great undergraduate students that have assisted me in some of the projects included in this work and others conducted during my studies. I would also like to acknowledge all of my other co-authors Vincenzo Grillo, Alicia Sit, Stefano Frabboni, Rafal E. Dunin-Borkowski, Miles J. Padgett, Robert Fickler, Jeremy Upham, Alison M. Yao, Christopher Travis, Israel De Leon, Andrea Rubano, Gian-Luca Oppo, Amir H. Tavabi, Federico Venturi, Roberto Balboni, Gian Carlo Gazzadi, Peng-Han Lu, Erfan Mafakheri, Martin P.J. Lavery, Yingwen Zhang, Ido Kaminer, Danica Sugic, Alexander J. Taylor, and Mark R. Dennis for making all of the works presented in this thesis possible.

I finally thank my parents, Andrea Muschinske and Yves Larocque, for providing me with their support during the course my studies.

Table of Contents

CV

Publications

1. **H. Larocque**, F. Bouchard, V. Grillo, A. Sit, S. Frabboni, R. E. Dunin-Borkowski, M. J. Padgett, R. W. Boyd, and E. Karimi, "Nondestructive measurement of orbital angular momentum for an electron beam," *Physical Review Letters* **117**, 154801 (2016).

2. F. Bouchard, **H. Larocque**, A. M. Yao, C. Travis, I. De Leon, A. Rubano, E. Karimi, G.-L. Oppo, and R. W. Boyd, "Polarization shaping for control of nonlinear propagation", *Physical Review Letters* **117**, 233903 (2016).

3. **H. Larocque**, J. Gagnon-Bischoff, F. Bouchard, R. Fickler, J. Upham, R. W. Boyd, and E. Karimi, "Arbitrary optical wavefront shaping via spin-to-orbit coupling", *Journal of Optics* **18**, 124002 (2016).

4. **H. Larocque**, and E. Karimi, "A New Twist on Relativistic Electron Vortices", *Physics Viewpoint* **10**, 26 (2017).

5. V. Grillo, A. H. Tavabi, F. Venturi, **H. Larocque**, R. Balboni, G. C. Gazzadi, S. Frabboni, P.-H. Lu, E. Mafakheri, F. Bouchard, R. E. Dunin-Borkowski, R. W. Boyd, M. P. J. Lavery, M. J. Padgett, and E. Karimi, "Measuring an electron beam's orbital angular momentum spectrum", *Nature Communications* **8**, 15536 (2017).

6. **H. Larocque**, J. Gagnon-Bischoff, D. Mortimer, Y. Zhang, F. Bouchard, J. Upham, V. Grillo, R. W. Boyd, and E. Karimi, "Generalized optical angular momentum sorter and its application to high-dimensional quantum cryptography", *Optics Express* **25**, 19832 (2017).

7. A. Sit, F. Bouchard, R. Fickler, J. Gagnon-Bischoff, **H. Larocque**, K. Heshami, D. Elser, C. Peuntinger, K. Günthner, B. Heim, C. Marquardt, G. Leuchs, R. W. Boyd, and E. Karimi, "High-Dimensional Intra-City Quantum Cryptography with Structured Photons", *Optica* **4**, 1006 (2017).

8. V. Grillo, A. H. Tavabi, E. Yucelen, P.-H. Lu, F. Venturi, **H. Larocque**, L. Jin, A. Savenko, G. C. Gazzadi, R. Balboni, S. Frabboni, P. Tiemeijer, R. E. Dunin-Borkowski, and E. Karimi, "Towards a holographic approach to spherical aberration correction in scanning transmission electron microscopy", *Optics Express* **25**, 21851 (2017).

9. Y. Zhang, A. Sit, F. Bouchard, **H. Larocque**, E. Cohen, A. C. Elitzur, J. L. Harden, R. W. Boyd, and E. Karimi, "Interaction-Free Ghost-Imaging of Structured Objects", arXiv:1711.09171 (2017).

10. J. Pierce, J. Webster, **H. Larocque**, E. Karimi, B. McMorran, and A. Forbes, "Non-radiating angularly accelerating electron waves", arXiv:1711.10114 (2017).

11. **H. Larocque**, I. Kaminer, V. Grillo, R. W. Boyd, and E. Karimi, "Twisting neutrons may reveal their internal structure" *Nature Physics* **14**, 1–2 (2018).

12. **H. Larocque**, I. Kaminer, V. Grillo, G. Leuchs, M.J. Padgett, R. W. Boyd, M. Segev, and E. Karimi, " 'Twisted' Electrons" *Contemporary Physics* **59**, 1–19 (2018).

Statement of originality and collaborative contributions

The author states that the works described in this Master's thesis constitute original research in the field of physics. The collaborative contributions of other participants in the works presented in each chapter is provided below.

E. Karimi initiated the work of chapter 2. H. Larocque designed the devices. H. Larocque, J. Gagnon-Bischoff, and J. Upham fabricated the devices. H. Larocque, J. Gagnon-Bischoff, F. Bouchard, and R. Fickler characterized the devices. R. Fickler, R. W. Boyd, and E. Karimi supervised all aspects of the project. All authors contributed to the text of the manuscript.

The works presented in chapter 3 encompass the development of two types of orbital angular momentum (OAM) sorters: a generalized optical angular momentum sorter and an electron orbital angular momentum (OAM) sorter.

E. Karimi initiated the work concerning the generalized optical angular momentum sorter. H. Larocque, J. Gagnon-Bischoff, and Y. Zhang designed the device. H. Larocque, D. Mortimer, and J. Upham fabricated the device. H. Larocque, D. Mortimer, and F. Bouchard characterized the devices. H. Larocque, D. Mortimer, and V. Grillo analyzed the data. R. W. Boyd, and E. Karimi supervised all aspects of the project. All authors contributed to the text of the manuscript.

V. Grillo, R. W. Boyd, R. E. Dunin-Borkowski, M. J. Padgett, and E. Karimi initiated the work concerning the electron OAM sorter. M. J. Padgett, V. Grillo, M. P. J. Lavery, and E. Karimi designed the device. F. Venturi, G. C. Gazzadi, P.-H. Lu, and E. Mafakheri fabricated the device. F. Venturi, G. C. Gazzadi, and S. Frabboni fabricated the analyzed magnetic specimen. A. H. Tavabi, V. Grillo, S. Frabboni and R. Balboni performed the experiment. V. Grillo and A.H. Tavabi analyzed the data. V. Grillo, H. Larocque, F. Bouchard, and E. Karimi developed the application theory.

H. Larocque, F. Bouchard, and E. Karimi with the help from other authors wrote the manuscript. All authors discussed the results and contributed to the text of the manuscript.

E. Karimi and M. J. Padgett initiated the work of chapter 4. H. Larocque, F. Bouchard, V. Grillo, A. Sit, S. Frabboni, and E. Karimi developped the presented theory. M. J. Padgett, R. W. Boyd, and E. Karimi supervised all aspects of the project. All authors contributed to the text of the manuscript.

The contents of chapter 5 concern the more exotic forms of structured waves: structured waves in nonlinear media and structured neutron waves.

E. Karimi, R. W. Boyd, and G.-L. Oppo initiated the work centered on structured waves in nonlinear media. E. Karimi, I. De Leon, and A. Rubano designed the experiment. H. Larocque and F. Bouchard conducted the experiment. H. Larocque analyzed the data. A. M. Yao, Christopher Travis, and G.-L. Oppo performed the simulations. G.-L. Oppo, R. W. Boyd, and E. Karimi supervised all aspects of the project. All authors contributed to the text of the manuscript.

E. Karimi initiated the work on structured neutron waves. H. Larocque, I. Kaminer, V. Grillo, and E. Karimi developped the theory. R. W. Boyd, and E. Karimi supervised all aspects of the project. All authors contributed to the text of the manuscript.

E. Karimi initiated the work on optical polarization knots presented in chapter 6. H. Larocque and D. Sugic designed the holograms used to generate the knots. H. Larocque, D. Mortimer, and R. Fickler performed the experiment. H. Larocque, D. Sugic, and A. J. Taylor analyzed the data. R. W. Boyd, M. R. Dennis, and E. Karimi supervised all aspects of the project.

List of Figures

can be used to extract the knotted C-points from the measured polarization field.

6.5 **Seifert surfaces**. Seifert surface reconstruction of experimentally generated and numerically simulated optical knots. The considered structures include a Hopf link, a trefoil knot, a cinquefoil knot, and a figure-eight knot.

6.6 **Genus of the figure-eight knot**. Genus of the figure-eight knot's Seifert surfaces acquired both experimentally and theoretically. Theoretical plots of the unstable surfaces around which the two extra holes appear are also shown.

Chapter 1

Introduction

Wave-particle duality manifests itself in several physical systems where effects pertaining to quantum theory are relevant. Namely, entities that are classically considered as particles, such as electrons, can exhibit several wave-like features prescribed by the laws of quantum mechanics, which include interference and diffraction. Such features can be observed in a variety of systems such as atoms, molecules, solid state materials, and even while experiencing free-space propagation. Likewise, entities to which a wave-like nature is classically attributed can display particle-like properties under certain conditions. For instance, optical waves can be represented by particle-like objects known as photons, whose properties can be observed in experiments and theories pertaining to quantum optics.

This dual nature can often lead to analogous physical behaviours between systems that are seemingly different. Examples of such systems are free-matter waves, i.e. matter that is not subjected to any forces, and optical waves traveling in free-space, i.e. oscillatory electromagnetic fields that are not subjected to any boundary conditions. Within a certain order of approximation, both types of waves can experience what is known as paraxial propagation, which is experienced by waves whose transverse extent is much larger than their wavelength. The equation that dictates this type of propagation is known as the paraxial wave equation and admits various types of solutions defined by different symmetries. One of these solutions is characterized by an azimuthally dependent phase that manifests itself as an $\exp(i\ell\varphi)$ term in its formulation, where ℓ is an integer known as the wave's topological charge and φ is the transverse azimuthal angle in cylindrical coordinates. This term causes the wave to have wavefronts consisting of $|\ell|$ intertwined helices with a handedness dictated by the sign of ℓ. Such *twisted* waves are also defined by several properties that are traditionally attributed to particles. Namely, in addition to a linear momentum defined by their wavevectors, they also carry $\hbar\ell$ units of orbital angular momentum (OAM) per particle, where $\hbar$ is the reduced Planck constant. When these waves are coherently added onto one another, they adopt exotic wave structures primarily attributed to the interference defined by the helical wavefronts of the wave's constituents. For this reason, such waves are commonly referred to as *Structured Waves* and often display interesting topological features. The body of works presented in this thesis primarily focuses on developing new ways of generating, manipulating, and characterizing optical and matter waves in which such topological features manifest themselves.

Several schemes can be used to generate structured waves, most of which that can be applied to both optical and matter waves. In essence, their generation falls down to the ability of imparting a spatially varying phase profile onto a plane-wave. One of the most straightforward ways of achieving this task is to make a beam go through an optical element with a spatially varying thickness, thus causing the incoming wave to experience a spatially varying optical path length and thereby acquire a corresponding spatially varying phase. This method also exists for matter waves where the optical material is replaced by a material with a mean inner potential affecting the wave's de Broglie wavelength and hence its spatial profile. Holography, the process of generating a wave from its interference pattern with a given "input" wave, is also a viable method to generate structured waves given that a hologram's construct is essentially based on its generated waves' phase profile. Another way of producing structured waves is by imparting a plane wave with a space-varying geometric phase. In essence, geometric phases are acquired by a wave-like entity upon adiabatically perturbing one of its physical properties. For an optical wave, this trait could be its polarization which can be adiabatically perturbed by sending the wave through a birefringent medium. The work presented in chapter 2 involves generating and characterizing a wide variety of structured optical waves through the use of this scheme. In addition to examining the phase acquired by the beams, the scheme's interaction with the beam's polarization and how it causes it to acquire various space-varying polarization profiles is also investigated.

Though the schemes used to characterize the exotic waves generated in chapter 2 provide ways of reconstructing their intensity, phase, or polarization profiles, they are often not of use in potential applications that employ structured waves. Namely, most of such applications seek to decompose structured waves based on their OAM content. The need to readily accomplish such a task arises from the fact that information is often stored within a beam's OAM hence the need to analyze it. For instance, the OAM of an optical beam often consists of an information channel used in optical communications while the OAM of a matter wave can often provide information regarding its interaction with physical systems. One way of performing such an OAM decomposition relies on the use of two confocal phase elements mapping the beam's azimuthal phase variations to spatially resolved spots. Such an action causes the device as a whole to effectively behave as an OAM sorter or an OAM "spectrometer", hence its convenience. The work presented in chapter 3 presents two extensions to this OAM sorter. The first is a sorter in which the two elements are liquid crystal cells that work based on the concepts presented in chapter 2. This modification causes the sorter to behave as a generalized optical angular momentum sorter, thus making it able to sort both an optical beam's OAM and polarization components. The utility of this device is then demonstrated by using it in a ten-dimensional quantum cryptography scheme to decrypt information stored in both of these photonic degrees of freedom. The second sorter of this chapter is a device where the two phase elements are replaced by electron wave holograms, thus causing the device to act as an OAM sorter for electron waves. The usefulness of this device is then shown by using it to analyze the OAM content of an electron beam affected by a magnetic pillar.

Most OAM detection schemes rely on the use of detectors providing cross-sectional images of an analyzed wave which inevitably brings up the question of whether OAM-carrying waves can be detected by more indirect means. The work presented in chapter 4 proposes such a characterization scheme for OAM-carrying electron waves. The underlying principle of this proposal relies on the fact that OAM-carrying electrons are defined by a magnetic dipole moment proportional to the OAM they carry. As a result, passing an OAM-carrying electron through a circular conductive element will result in the generation of Eddy currents whose magnitude is proportional to the OAM carried by the electron. Moreover, the change experienced in the energy and the phase of the passing electron is found to be minimal. Therefore, one could potentially measure the OAM of an electron by measuring the currents in the element without significantly perturbing the state of the electron itself. Further details regarding the quantum nature of this measurement are investigated as well.

The works presented in chapter 5 involve the characterization of structured waves defined by more exotic properties. The first work of this chapter investigates the propagation of optical structured waves in a saturable Kerr nonlinear medium. Namely, in such media, OAM-carrying light beams are known to break up into $2\,|\ell|$ filaments, where ℓ corresponds to the OAM carried by the beam. This poses a challenge when using OAM-carrying beams to electromagnetically transport high-power energy through nonlinear media. In this work, the propagation of beams whose structures are defined by azimuthally varying polarization structures are found to be more robust to break-up phenomena than beams with azimuthally varying phases.

The second work presented in this chapter examines the physical properties of particles that carry an internal structure and how this structure could manifest itself when the particle's wavefunction is shaped in such a way that it acquires OAM. Namely, the presented analysis is demonstrated for neutrons, which are defined by an internal charge density. The work in this part of the chapter suggests that adding OAM to free neutrons causes them to acquire OAM-dependent charge and current densities which result in several OAM-dependent electromagnetic properties from which further details concerning the neutron's internal structure could potentially be extracted.

The work presented in chapter 6 pertains to the generation and the characterization of knots encoded in the transverse polarization structure of an optical beam. The topology of these optical polarization knots is shown to be much more easily characterized then that of knots formed by optical phase vortices. This is demonstrated by reconstructing the Seifert surfaces of the knot, which in this case consist of phase sheets of the wavefield formed by the beam's polarization structure. With this reconstruction procedure, topological information pertaining to the examined knot's structure can be obtained to provide interesting information regarding their structural stability. This reconstruction procedure was performed for knots that have been previously generated in the phase profile of optical beams, such as torus knots, and for knots that have never been previously generated in optical structures, such as the figure-eight knot.

Chapter 2

Structuring light with geometric phases

This chapter is based on the following paper:

1. **H. Larocque**, J. Gagnon-Bischoff, F. Bouchard, R. Fickler, J. Upham, R. W. Boyd, and E. Karimi, "Arbitrary optical wavefront shaping via spin-to-orbit coupling", *Journal of Optics* **18**, 124002 (2016).

   DOI: https://doi.org/10.1088/2040-8978/18/12/124002 2040-8978/

2.1 The paraxial wave equation

Wave-like entities in free-space can often be described by an oscillatory field $\mathcal{A}(\mathbf{r})$ that satisfies the paraxial wave equation:

$$\boldsymbol{\nabla}_{\perp}^{2}\mathcal{A}(\mathbf{r}) + 2ik_z\frac{\partial}{\partial z}\mathcal{A}(\mathbf{r}) = 0, \tag{2.1}$$

where $\boldsymbol{\nabla}_{\perp}^{2}$ is the transverse Laplacian, $\mathbf{r}$ is the position vector, z is the longitudinal spatial coordinate, $k_z = 2\pi/\lambda$ is the longitudinal component of the the wave's wave vector, and λ is the wave's wavelength. Optical waves in free-space of the form $E(\mathbf{r}, t) = \mathcal{E}(\mathbf{r})\exp\left(i(k_z z - \omega t)\right)$, where t is time, $\omega = ck_z$, and c is the velocity of light, are considered paraxial when $\mathcal{E}(\mathbf{r})$ satisfies the paraxial wave equation. The conditions under which this criterion is satisfied can be found by directly substituting $E(\mathbf{r}, t)$ in the optical wave equation:

$$\boldsymbol{\nabla}^2 E(\mathbf{r}, t) - \frac{1}{c^2}\frac{\partial^2}{\partial t^2}E(\mathbf{r}, t) = 0. \tag{2.2}$$

Performing this substitution readily yields the following equation:

$$\boldsymbol{\nabla}_\perp^2 \mathcal{E}(\mathbf{r}) + 2ik_z\frac{\partial}{\partial z}\mathcal{E}(\mathbf{r}) + \frac{\partial^2}{\partial z^2}\mathcal{E}(\mathbf{r}) = 0, \tag{2.3}$$

which corresponds to the paraxial wave equation provided that the last term vanishes. To find conditions under which the term vanishes, we can rearrange the above equation in terms of dimensionless coordinates scaled to the physical parameters describing the wave. For instance, the wave's dimensionless Cartesian coordinates $(\tilde{x}, \tilde{y}, \tilde{z})$ may be expressed in terms of the Cartesian coordinates (x, y, z) as $x = w_0\tilde{x}$, $y = w_0\tilde{y}$,$z = z_R\tilde{z}$, where w_0 is the wave's beam waist, which corresponds to the wave's transverse extent, and $z_R = \pi {w_0}^2/\lambda$ is the wave's Rayleigh range and corresponds to the longitudinal distance over which the wave starts to experience significant effects attributed to diffraction. When these factors are considered, Eq. (2.3) can be written as:

$$\widetilde{\boldsymbol{\nabla}}_\perp^2 \mathcal{E}(\tilde{\mathbf{r}}) + 4i\frac{\partial}{\partial \tilde{z}}\mathcal{E}(\tilde{\mathbf{r}}) + \frac{\lambda^2}{\pi^2 {w_0}^2}\frac{\partial^2}{\partial \tilde{z}^2}\mathcal{E}(\tilde{\mathbf{r}}) = 0, \tag{2.4}$$

from which we can readily deduce that the last term vanishes whenever the wave's transverse extent is much larger than its wavelength, hence the condition under which the paraxial wave equation can faithfully represent optical waves propagating in free space.

The behaviour of non-relativistic free matter waves can also be represented by the paraxial wave equation [1]. Unlike optical waves, whose dynamics are accounted by the optical wave equation, free matter waves are represented by a wavefunction $\Psi(\mathbf{r}, t)$ that satisfies the potential-free Schrödinger equation:

$$-\frac{\hbar^2}{2m}\boldsymbol{\nabla}^2\Psi(\mathbf{r}, t) = i\hbar\frac{\partial}{\partial t}\Psi(\mathbf{r}, t), \tag{2.5}$$

where $\hbar$ is the reduced Planck constant, and m is the considered particle's mass. At first glance, the potential-free Schrödinger equation is fairly similar to the paraxial wave equation provided that time, t, replaces the longitudinal coordinate z and that the latter is considered as a transverse coordinate. However, the Schrödinger equation can be reduced such that it accounts for the same dimensions as the ones in the paraxial wave equation. Such a reduction can be accomplished for wavefunctions

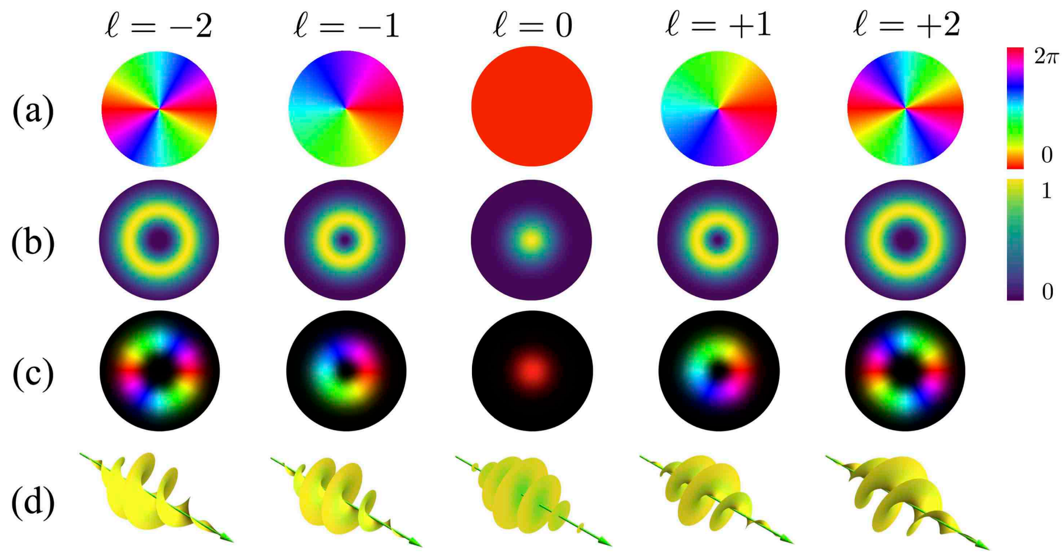

Figure 2.1: **Laguerre-Gaussian beams**. (a) Transverse phase profile, (b) intensity profile (in units of maximum intensity), (c) phase profile modulated by the intensity profile, and (d) wavefronts of Laguerre-Gaussian modes where $p = 0$.

of the form $\Psi(\mathbf{r}, t) = \psi(\mathbf{r}) \exp(i(p_0 z - \varepsilon t)/\hbar)$, where p_0 is the wavefunction's central longitudinal momentum, and $\varepsilon = {p_0}^2/(2m)$ is the particle's energy. When the wavefunction adopts such a form, the Schrödinger equation adopts the form of the paraxial wave equation provided that its transverse extent is much larger than its de Broglie wavelength $\lambda_{\mathrm{dB}} = h/p_0$, where h is Planck's constant.

There are several sets of complete solutions to the paraxial wave equation that are defined by different symmetries. Some of them, such as the Hermite-Gaussian, Laguerre-Gaussian [2], and Ince-Gaussian modes [3], are othonormal sets, while others, like Hypergeometric-Gaussian modes [4], are not. Paraxial structured waves often refer to waves that are defined by non-trivial combinations of such solutions which often display interesting properties that manifest themselves in their modal structure [5]. To illustrate, consider the Laguerre-Gaussian (LG) modes. LG modes are the natural solutions of the paraxial wave equation in cylindrical coordinates (ρ, φ, z) and are defined by two integer indices ℓ and $p \geq 0$. The intensity, phase, and wavefronts of some LG modes where $p = 0$ can be found in Fig. 2.1. Among their distinguishing traits is the presence of a phase singularity, a point of undefined phase, at their centre accompanied by a null in the mode's intensity profile. The presence of this singularity is a direct result of the presence of the beam's azimuthal phase dependence accounted by an $\exp(i\ell\varphi)$ term in their formulation. As mentioned earlier, this azimuthal phase dependence also causes the mode to have wavefronts consisting of $|\ell|$ intertwined helices with a handedness given by the sign of ℓ. This azimuthal phase also causes the mode to carry ℓ units of OAM [6]. Namely, when the mode represents a physical entity defined by a dual nature, the particle attributed to the mode carries an OAM value of $\hbar\ell$. Due to these numerous structural features, LG modes hold a central role in the formulation of paraxial structured waves.

2.2 Optical singularities

The central phase singularities of the LG modes account for several of their physical properties including their helical wavefronts and their OAM. Phase singularities can also occur in regions other than a beam's optical axis. Like the ones in LG modes, phase singularities are defined by a topological charge with an absolute value corresponding to the amount of 2π-phase cycles occurring along a path surrounding the singularity and whose sign is determined by the handedness of these phase cycles [7, 8, 9]. Phase singularities are also known to experience interesting dynamics. For instance, pairs of them can spontaneously appear or annihilate each other upon propagation [10]. These phenomena can make the trajectories of a structured wave's singularities form loops upon propagation, some of which forming exotic topological structures such as links and knots [11, 12, 13].

There are other optical properties apart from phase that can also be singular. One of these properties consists of polarization, a property attributed to the vectorial nature of light. Polarization singularities occur when the ellipse traced out by an optical wave's polarization vector has undefined properties and are relevant in the topological classification of optical waves defined by space-varying transverse polarization profiles [8, 9]. These properties namely include the polarization ellipse's orientation and its handedness. Orientation singularities occur in the form of C-points and V-points that manifest themselves as points of circular polarization or polarization vortices, respectively. Unlike phase singularities, C-points are not defined by an intensity null as they are defined by circular polarization. On the other hand, V-points are defined by an intensity null. Both types of singularities are defined by a topological charge attributed to the amount of rotations experienced by the polarization ellipses surrounding them. Singularities consisting of regions of undefined polarization handedness are known as L-lines, i.e. lines of linear polarization, and consist of closed loops of linearly polarized light. Examples of beams carrying polarization singularities are

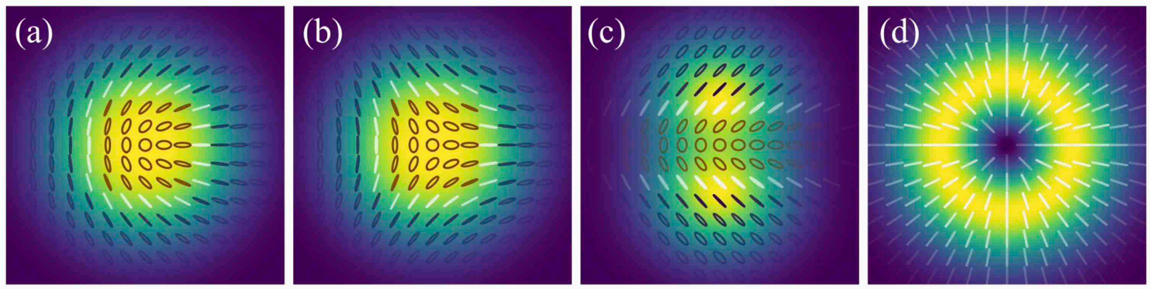

Figure 2.2: **Polarization topologies and singularities**. Space-varying polarized light beams consisting of so-called (a) lemon, (b) star, (c) monstar, and (d) radial polarization topologies. The patterns formed by the polarization ellipses of the beams are plotted on top of their intensity profiles. The ellipses are coloured based on their handedness. Brown ellipses are left-handed, purple ones are right-handed, and white ones account for linear polarization. Central C-points surrounded by L-lines are present in the lemon, star, and monstar polarization topologies and a V-point is positioned at the centre of the radially polarized beam.

illustrated in Fig. 2.2.

2.3 Generating structured waves

Structured waves are often generated by coherently modulating their wavefronts as a means to imprint a given transverse phase structure to the wave. There exists several methods that can be used to achieve this modulation.

A rather direct way of manipulating a beam's transverse phase profile is to make it go through an optical element in which it experiences a change in its wavelength. If this element has a varying transverse thickness, then different transverse regions of the beam will experience different phase shifts upon propagating through the element, thus causing it to acquire a structured transverse phase profile. Such elements are commonly referred to as phase plates and their material composition depends on the type of beam they manipulate [14]. Phase plates that work for optical waves are made of a transparent material with a refractive index different to that of the medium in which the beam mainly propagates. Phase plates that work for matter waves are made of materials imposing a potential to the wave, which reduces its kinetic energy and thereby increases its de Broglie wavelength [15]. For instance, silicon nitride is often used when dealing with electron waves [16].

Holography is also now a common tool for generating structured waves. Holograms used for such purposes consist of amplitude or phase diffraction gratings that replicate the interference pattern between an off-axis plane wave and a wave with a specific transverse phase structure. Making a plane wave propagate through such a device will thus result in the generation of the corresponding structured wave in the first order of the grating's diffraction pattern. Unlike phase plates, the produced structured wave is not co-propagating with any unconverted components of the incident plane wave. This makes holograms more advantageous in terms of the generated wave's purity. However, this feature comes at the expense of realigning experimental components with respect to the device's first diffraction order. Holograms are used in works pertaining to both optical [17] and matter waves [18, 19, 20] and can be made from the same materials as phase plates.

2.3.1 Geometric phase

Unlike phase plates and holograms, which directly modulate a wave's transverse phase profile, devices that rely on geometric phases modify another of the wave's properties as a means to structure its wavefronts. This process relies on the fact that geometric phases are acquired by wave-like entities upon having one of their properties adiabatically modified in a periodic fashion [21]. Such properties include, for instance, a quantum particle's spin or the polarization vector of an optical wave [22].

An optical beam's polarization vector can be adiabatically modified by means of a birefringent medium. Namely, when a polarized optical beam traverses such a medium, it will experience a gradual change in its polarization vector that depends on several factors. The first of the latter consists of the relative orientation of the wave's polarization vector with respect to the axis determined by the anisotropy of the birefringent medium's refractive index. In the optics community, this axis is commonly referred to as the medium's slow (or fast) axis, or simply as its optical axis. The second factor consists of the relative phase delay experienced by a beam's orthogonal polarization components upon propagating through the medium. This trait is often referred to as the device's retardation and depends on the extent of the medium's birefringence and the ratio between the beam's wavelength and the medium's thickness. These features are notably used in the design of wave-plates which consist of a medium with a uniform optical axis that specifically modifies a beam's polarization by uniformly adding different relative phases to its circularly polarized components.

Devices that produce structured waves by means of geometric phases operate very similarly to wave-plates. Conceptually, the only difference between these two types of elements is that the optical axis of a wave-plate is fixed along the beam's profile while that of a geometric phase element is patterned. As a result, this pattern is translated to an incident beam's phase and its polarization profile which can adopt interesting topological features such as phase and polarization singularities provided that these features are engineered into the spatial distribution formed by the geometric phase element's optical axis [23, 24, 25]. In recent years, several devices relying on this conversion process, including so-called q-plates, have been developed and have found many applications related to the use of structured waves. q-plates are slabs of birefringent liquid crystals that are patterned to have an azimuthally dependent molecular axis distribution [26]. This causes beams going through the q-plate to either adopt an azimuthally dependent phase or polarization profile. In the former case, this azimuthal phase causes the beam to acquire OAM. Given that this OAM is acquired by modifying the beam's polarization, which is related to a photon's spin, this phase imparting process is sometimes referred to as optical spin-to-orbit coupling. Similar schemes exist for electron waves as well in which OAM is acquired by enabling a systematic precession of the electron wave's spin through its propagation in a structured magnetic field [27]. Both of these spin-to-orbit coupling mechanisms result from the wave's interaction with a structured physical entity. Spin-to-orbit coupling can also occur whenever a wave is subjected to somewhat extreme physical conditions. For instance, optical waves experience such phenomena when they are tightly focused [28] while electron waves are subjected to it in relativistic regimes [29, 30, 31, 32, 33]

The publication to which this chapter is dedicated focuses on using such forms of "spin-to-orbit-coupling" to produce a wide range of liquid crystal devices similar to q-plates [25]. However, these devices produce a greater extent of structured waves defined by interesting phase and polarization topologies. The fabrication of these devices relies on the use of a method developed to arbitrarily pattern the molecular orientation of the device's liquid crystal slab, thus resulting in the generation of optical structures equally arbitrary wavefronts. The flexibility of the presented method allows for the fabrication of devices with applications that go beyond beam-shaping. For instance, it enables the fabrication of birefringent lithographs [34], and of optical elements used in high-dimensional quantum cryptography schemes [35, 36] and in the generation of structured higher harmonics [37].

IOP Publishing Journal of Optics
J. Opt. 18 (2016) 124002 (10pp) doi:10.1088/2040-8978/18/12/124002

Arbitrary optical wavefront shaping via spin-to-orbit coupling

Hugo Larocque[1], Jérémie Gagnon-Bischoff[1], Frédéric Bouchard[1], Robert Fickler[1], Jeremy Upham[1], Robert W Boyd[1,2] and Ebrahim Karimi[1,3]

[1] The Max Planck Centre for Extreme and Quantum Photonics, Department of Physics, University of Ottawa, 25 Templeton St., Ottawa, Ontario, K1N 6N5, Canada
[2] Institute of Optics, University of Rochester, Rochester, NY 14627, USA
[3] Department of Physics, Institute for Advanced Studies in Basic Sciences, 45137-66731 Zanjan, Iran

E-mail: ekarimi@uottawa.ca

Received 19 August 2016, revised 23 October 2016
Accepted for publication 28 October 2016
Published 21 November 2016

Abstract

Converting spin angular momentum to orbital angular momentum has been shown to be a practical and efficient method for generating optical beams carrying orbital angular momentum and possessing a space-varying polarized field. Here, we present novel liquid crystal devices for tailoring the wavefront of optical beams through the Pancharatnam–Berry phase concept. We demonstrate the versatility of these devices by generating an extensive range of optical beams such as beams carrying ± 200 units of orbital angular momentum along with Bessel, Airy and Ince–Gauss beams. We characterize both the phase and the polarization properties of the generated beams, confirming our devices' performance.

Keywords: liquid-crystal devices, laser beam shaping, optical vortices

(Some figures may appear in colour only in the online journal)

1. Introduction

Optical beams are widely used in many areas of modern science such as microscopy, lithography, optical tweezers, and communications. The extent of these applications is essentially determined by the attributes of the employed beams such as their polarization features, diffractive properties, and orbital angular momentum (OAM). For instance, OAM-carrying beams—beams possessing a helical phase structure and a donut-shaped transverse intensity profile—can be used to rotate micro-particles [1, 2], enhance optical resolution in stimulated emission depletion microscopy [3], and increase a communication channel's capacity [4, 5]. Likewise, shape-invariant optical beams modulated by Airy [6] and Bessel [7] functions have potential applications in optical trapping [8, 9]. Finally, space-varying polarized light beams—beams with certain polarization topologies—have been shown to produce needle-shaped longitudinal electric and magnetic dipoles [10, 11] and exotic 3D polarization structures [12, 13], hence their usefulness for exploring novel physical and optical phenomena. The above applications require individually specific beams characterized by well-defined intensity, phase, and polarization attributes, thus motivating the development of novel beam shaping methods and devices.

Spatial light modulators (SLMs)—pixelated liquid crystal devices that are capable of introducing a specific phase modulation onto an incident beam—have been widely used in different configurations to tailor certain optical phase, intensity, and polarization distributions [14–17]. However, SLMs have a few drawbacks bounding them to laboratory-scale usage. To begin with, they are pixelated and limited to a certain phase modulation resolution (usually associated with 8-bit, 256 grayscale encryption). This restrains SLMs to diffractive configurations which makes them effectively bulky and lowers their efficiency. In addition, their operation is characterized by fairly low phase modulation rates ($\lesssim$500 Hz), which affect their dynamical capabilities. Similar diffraction devices, such as deformable mirror arrays and digital micro-mirror devices (DMD) have similar problems [18]. A few optical devices, such as axicons [19], mirror-cones [20–22], q-plates [23], astigmatic mode converters [24], and achromatic-OAM generators [25] have been introduced to generate specific optical beams. However, the most efficient and compact of these devices are Pancharatnam–Berry phase optical elements (PBOEs) [26, 27] which have the ability to tailor optical beams through the addition of a geometric phase. In essence, they add a transverse phase profile to a beam upon flipping its circular polarization state. This phase alteration depends on the device's geometry. Only a few methods have so far been proposed to manufacture PBOEs [27–30]. Though these techniques have historically been mainly capable of generating azimuthally structured devices [23, 29, 31, 32], recent extensions to such methods have allowed for arbitrarily structured devices [33–40]. Here, we present a configuration capable of manufacturing PBOEs generating a wide and versatile range of optical beams. We use them to generate OAM-carrying, Bessel, Airy, and Ince–Gauss (IG) optical beams. We also exploit our PBOEs' spin-to-orbit coupling properties through the generation of space-varying polarized beams by providing linearly polarized input beams to our devices.

2. Theory

Many physical entities can acquire a global phase upon being subjected to cyclic adiabatic processes. Such phases are commonly known as Pancharatnam–Berry (geometric) phases [41, 42]. The latter of these terms is associated with the geometric transformation of the parameters defining the corresponding cyclic process. Among the many systems that can acquire a geometric phase are polarized optical beams through the adiabatic variation of their polarization states. These states can be expanded in terms of a two dimensional vector space and can thus be effectively mapped onto the surface of a unit sphere known as the Poincaré sphere. An arbitrary unitary transformation of an optical beam's polarization state can be performed by a sequence of (half- and quarter-) wave plates. Upon a cyclic polarization transformation along a closed path on the Poincaré sphere, a phase corresponding to half of the solid angle enclosed by the path will be added to the beam [43].

This effect can be clearly illustrated through the example of a half-wave plate (HWP) acting upon light whose polarization is expressed in the circular polarization basis $\{\mathbf{e}_\mathrm{L}, \mathbf{e}_\mathrm{R}\}$ where $\mathbf{e}_\mathrm{L}$ and $\mathbf{e}_\mathrm{R}$ are respectively the left- and right-handed circular polarization vectors. Namely, when the HWP is oriented at an angle of α with respect to its optical axis, the solid angle enclosed by the path of the beam's polarization vector on the Poincaré sphere is $\pm 4\alpha$. As a result, the beam's left-handed component becomes right-handed and acquires a phase of 2α while the beam's right-handed component becomes left-handed and acquires a phase of -2α. This action is described by

$$\begin{bmatrix}\mathbf{e}_\mathrm{L}\\ \mathbf{e}_\mathrm{R}\end{bmatrix} \xrightarrow{\mathrm{HWP}_\alpha} \begin{bmatrix}\mathbf{e}_\mathrm{R}\mathrm{e}^{+2\mathrm{i}\alpha}\\ \mathbf{e}_\mathrm{L}\mathrm{e}^{-2\mathrm{i}\alpha}\end{bmatrix}. \tag{1}$$

Besides HWPs, which are defined by a uniform optical axis and add a constant phase to a beam, there are other types of devices, such as PBOEs, designed to add a space-varying geometric phase to an incident beam. Due to the identical nature of the phase added by both of these optical elements, one can readily establish an analogy between the optical properties of a HWP and those of a PBOE. In essence, much like how the uniformity of the phase added by a HWP arises from its uniform optical axis, the spatial dependence of the phase added by a PBOE can be seen as stemming from a non-uniform optical axis distribution. More specifically, this distribution is given by $\alpha(x_1, x_2)$, where x_1 and x_2 are coordinates defining the position on the beam's transverse profile. As in the case of a HWP, the corresponding added geometric phase is given by $\pm 2\alpha(x_1, x_2)$. However, in most cases, PBOEs are not perfect half-wave retarders, i.e. they are not defined by an optical retardation of π, but rather by a parameter δ. Hence, it follows that a PBOE's unitary action $\hat{\mathrm{U}}_q$ on an incident light beam in the circular basis, $\mathbf{e}_\mathrm{L}$ and $\mathbf{e}_\mathrm{R}$, for a given optical retardation δ and a general optical axis distribution $\alpha(x_1, x_2)$ is provided by [44]

$$\hat{U}_q \cdot \begin{bmatrix}\mathbf{e}_\mathrm{L}\\ \mathbf{e}_\mathrm{R}\end{bmatrix} = \cos\left(\frac{\delta}{2}\right)\begin{bmatrix}\mathbf{e}_\mathrm{L}\\ \mathbf{e}_\mathrm{R}\end{bmatrix} + \mathrm{i}\sin\left(\frac{\delta}{2}\right)\begin{bmatrix}\mathbf{e}_\mathrm{R}\mathrm{e}^{+2\mathrm{i}\alpha(x_1,x_2)}\\ \mathbf{e}_\mathrm{L}\mathrm{e}^{-2\mathrm{i}\alpha(x_1,x_2)}\end{bmatrix}. \tag{2}$$

Therefore, any beam that may be generated by imparting a space-varying phase to its transverse profile can be readily produced by PBOEs characterized by an appropriate optical axis distribution. Some distributions can in certain cases be more conveniently expressed in specific coordinate systems (x_1, x_2) such as Cartesian (x, y), cylindrical (ρ, φ), and elliptical (u, v) systems. In the following, we provide several examples of existing and potential PBOEs that generate beams whose mathematical formulations are more easily expressed with a certain coordinate system. These beams include OAM-carrying and Bessel beams (cylindrical), IG beams (elliptical), and Airy beams (Cartesian).

PBOEs have so far been mostly designed to make devices known as q-plates [26]. q-plates, a special class of PBOEs, possess an azimuthally symmetric optical axis given by $\alpha(\rho, \varphi) = q\varphi + \alpha_0$, where q is either a half or a full integer, α_0 is an arbitrary constant, and ρ and φ are the radial and azimuthal cylindrical coordinates, respectively [23]. These devices are of interest because of their ability to generate beams carrying a phase of $\ell\varphi$, where ℓ is an integer, thus causing the beam to carry OAM [28]. It has also been demonstrated that q-plates can be used to generate space-varying polarized light beams by either feeding linearly polarized light to the device or by adequately tuning its optical retardation [45, 46].

Adding a linear radial phase dependence, e.g. $k_\rho \rho$, to these OAM carrying beams will simulate passing the beam through an axicon. The beam's resulting total phase, $k_\rho \rho + \ell\varphi$, corresponds to that of a Bessel beam. The latter's transverse field is proportional to a $J_\ell(k_\rho \rho)\exp(i\ell\varphi)$ term, where ℓ is an integer, J_ℓ is the ℓ^th order Bessel function of the first kind, and k_ρ is the radial component of the beam's wavevector [47]. A potential design for a PBOE that generates such a beam could be defined by an optical axis satisfying $2\alpha(\rho, \varphi) = k_\rho \rho + \ell\varphi$. Similar to the previous case, different circular polarization components will acquire opposite values of OAM. However, one circular polarization component will be attributed with a phase of $+k_\rho \rho$ while the other with a phase of $-k_\rho \rho$. Effects related to these radial phase components will be more thoroughly discussed later on in the following sections.

Bessel and OAM beams can be readily generated by imposing a cylindrically symmetric phase onto an incident Gaussian beam. Other types of beams require the impartment of phase patterns that are more conveniently expressed in other coordinate systems. Such beams include the elliptically symmetric IG beams. IG beams form an additional complete set of orthonormal solutions to the paraxial wave equation expressed in elliptic coordinates (u, v) [48]. They include an Ince polynomial in their formulation defined by two integer indices p and m, along with an additional parameter ε referred to as the beam's ellipticity. These polynomials are categorized either as even or odd Ince polynomials and correspondingly yield the so called even, $\mathrm{IG}^{e}_{p,m,\varepsilon}$, and odd, $\mathrm{IG}^{o}_{p,m,\varepsilon}$, IG modes respectively. The number of hyperbolic and elliptic nodal lines in the transverse intensity profile of both sets of modes is determined by their m and p indices.

Beams resulting from the superposition of even and odd IG modes with a relative phase difference of $\pi/2$, i.e., $\mathrm{IG}^{\pm}_{p,m,\varepsilon} = \mathrm{IG}^{e}_{p,m,\varepsilon} \pm \mathrm{i}\,\mathrm{IG}^{o}_{p,m,\varepsilon}$ (±sign denotes the direction along which the beam's phase varies), are called helical IG beams and exhibit optical vortices and an elliptic phase dependence [49]. Helical IG modes were used to investigate several quantum features including two- and three-dimensional entanglement between their constituent photons [50] and hence have potential applications in quantum information protocols [51].

PBOEs characterized by an optical axis satisfying the relation $2\alpha(u, v) = \Phi_{\mathrm{IG}}(u, v)$, where Φ_{IG} is the phase of a helical IG beam, would be able to generate beams defined by interesting polarization properties. For instance, consider the case where Φ_{IG} is associated with an $\mathrm{IG}^{-}_{p,m,\varepsilon}$ beam. According to equation (2), the beam resulting from feeding an arbitrarily polarized Gaussian beam into a half-wave retarding $(\delta = \pi)$ IG PBOE will consist of two components, namely $\exp(\mathrm{i}\Phi_{\mathrm{IG}})\mathbf{e}_{\mathrm{R}}$ and $\exp(-\mathrm{i}\Phi_{\mathrm{IG}})\,\mathbf{e}_{\mathrm{L}}$. As previously mentioned, the sign in the formulation of helical IG modes defines the direction along which the beam's phase elliptically varies. In our case, adding a phase of $-\Phi_{\mathrm{IG}}$ would be equivalent to generating the $\mathrm{IG}^{+}_{p,m,\varepsilon}$ helical IG mode. With these factors brought into consideration, we can equivalently write the two components of the device's output beam as $\mathrm{IG}^{-}_{p,m,\varepsilon}\mathbf{e}_{\mathrm{R}}$ and $\mathrm{IG}^{+}_{p,m,\varepsilon}\,\mathbf{e}_{\mathrm{L}}$. Therefore, by feeding linearly polarized light into the device, the relative amplitude of both components should be equal from which it follows that the resulting beam can be decomposed into two orthogonally polarized linear components, one of which being the helical IG mode's even mode and the other being the corresponding odd mode.

Other types of beams, such as Airy beams, require the addition of a phase that can most readily be expressed in Cartesian coordinates. Like Bessel beams, Airy beams are diffraction-free solutions to the paraxial wave equation [52]. One of their distinguishing characteristics is the fact that their main intensity maxima seem to freely accelerate along a parabolic trajectory. To produce these beams, one can exploit the fact that the Fourier transform of an Airy function Ai is proportional to a term with a phase varying with the cube of the frequency [6, 53]. Thus, adding a phase with a cubic spatial dependence on an incident Gaussian beam and then taking its Fourier transform using an appropriate lens leads to a lab-scale realization of the corresponding Airy beam [6] within a certain propagation range. For instance, the following space-varying phase pattern can be used to generate a 2D Airy beam

$$\Phi_{\mathrm{Ai}}(x, y) = \frac{1}{3}\left\{\left[x_0\left(\frac{2\pi}{\lambda f}x\right)\right]^3 + \left[y_0\left(\frac{2\pi}{\lambda f}y\right)\right]^3\right\}, \tag{3}$$

where f is the focal length of the spherical converging lens used to take the Fourier transform of the beam, λ is the beam's wavelength, and x_0 and y_0 are parameters that describe the beam's deflection along the x and y coordinates, respectively, upon propagation. As in the case of the aforementioned PBOEs, an Airy beam generated by a PBOE is defined by certain polarization features. In essence, the left-handed component of an incident beam will acquire a phase of $\Phi_{\mathrm{Ai}}(x, y)$ while the right-handed component a phase of $-\Phi_{\mathrm{Ai}}(x, y)$. An appealing feature of this particular device is the fact that its added phase is an odd function satisfying $-\Phi_{\mathrm{Ai}}(x, y) = \Phi_{\mathrm{Ai}}(-x, -y)$. This odd symmetry causes the left handed component of the converted beam to look inverted with respect to the right handed component, which leads to an 'acceleration' along the opposite direction.

3. Fabrication and characterization

Cylindrically symmetric PBOEs can be fabricated by a variety of methods such as through the use of sub-wavelength gratings [27, 30], total internal reflection [25], plasmonic metasurfaces [29, 54], or an inhomogeneous and anisotropic layer of patterned nematic liquid crystals (NLC) [26]. Here, we employ the last of these methods to produce our PBOEs designed to add an arbitrary geometric phase to optical beams.

We first describe the method to construct a PBOE with a desired optical-axis pattern imprinted into its liquid crystal layer. Such a construction can be achieved through the photoalignment of an azobenze-based dye [55]. To perform this alignment, the azodye molecules must be exposed to specific linearly polarized light intensity patterns whose wavelength lies within a peak of the dye's absorption spectrum, thus aligning the molecules with the pattern's polarization [31, 32, 56]. When such an aligned azodye molecule is in contact with the PBOE's liquid crystals, the liquid crystal molecules will align themselves along the axis of the azodye. In practice, the contact between the two molecules is achieved by spin coating an azodye layer onto the inner region of two substrates enclosing the device's liquid crystals. Thus, by exposing well-defined areas of the coated substrates to

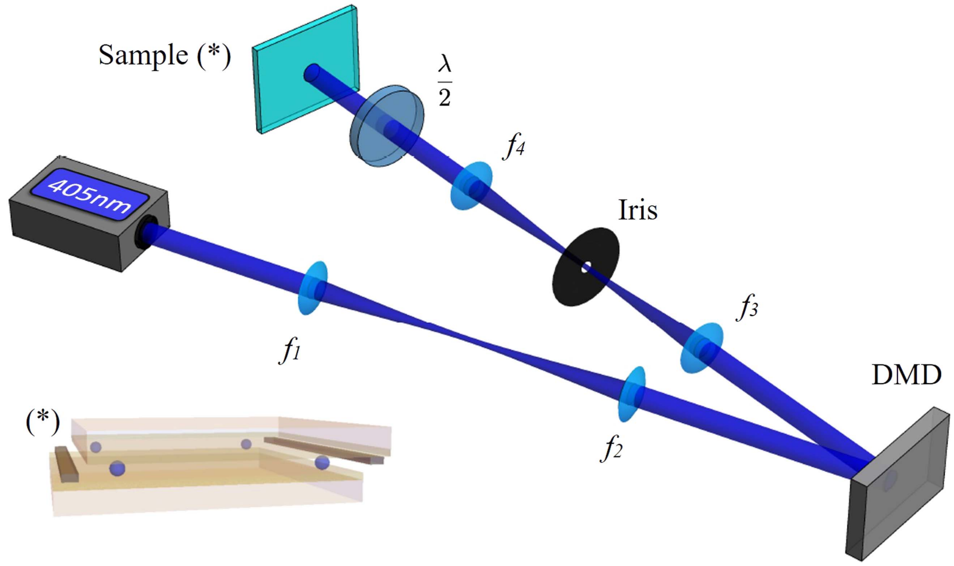

Figure 1. Fabrication apparatus. A 405 nm linearly polarized light beam is rotated and enlarged by going through a cylindrical 4-f system (f_1 and f_2). The beam then interacts with the DMD programmed to reflect a specific light intensity pattern. The reflected beam goes through another 4-f system (f_3 and f_4) and an iris in order to select only its brightest diffraction orders as a means to clearly image the pattern onto the sample. The polarization of the beam is then adjusted by a half-wave plate to the required orientation. After this rotation, the resulting beam aligns a specific region of the sample's photo-alignment layer. The device's structural frame is depicted in the inset in the lower-left region of the figure.

specifically polarized intensity patterns, one is able to construct the PBOE's space dependent optical axis. This design can also be modified to allow one to control the PBOE's optical retardation. More specifically, when substrates coated with a layer of a transparent conductive material such as indium tin oxide (ITO) are used, electrical wires can be soldered onto these substrates. This design modification allows one to apply an electric field to the PBOE's liquid crystals, thus giving the liberty to control its optical properties including its birefringence. As a result, the element's optical retardation becomes tunable, hence allowing one to use the device to generate a wider selection of optical beams and providing the ability to use the device on beams with different wavelengths [31].

We produce the device's dye-coated substrates by spin-coating the azobenzene-based aligning material PAAD-22 provided by BEAM Co onto the conductive side of an ITO-coated substrate using the procedure described in [56]. More specifically, the sample is spin coated for 60 s at a rotational speed of 3000 rpm and then soft baked at 120 °C for 5 min. This procedure typically results in the formation of a 50 nm thick alignment layer, as we verified by observation using a profilometer. Before being exposed to light patterns, the two coated substrates are attached together with the coated region facing towards the inside of the device using an epoxy glue. We glued them with a slight lateral offset in order to ensure that wires can be soldered onto the inner conductive sides of the substrates for tuning. Spacer-grade silica microspheres with diameters below 4.8 μm placed between the two plates ensure the presence of a uniformly spaced cavity in which liquid crystals can later be added. Prior to permanently gluing the plates together, the cavity's uniformity is visually optimized by minimizing the number of fringes produced by thin film interference resulting from the space between the plates. At this stage of the fabrication process, the device consists of the PBOE's structural frame and is depicted in the inset of figure 1.

Various methods are currently used to fabricate liquid-crystal-based PBOEs. For instance, to fabricate devices with an optical axis that solely depends on the azimuthal coordinate, a coated sample can be rotated under an angular light intensity pattern of a distinct polarization rotating at a different frequency than that of the sample [31, 56]. The resulting alignment will depend on the rotation frequency ratio of these two elements. However, to construct arbitrarily patterned devices, one must count on alternative methods relying on the use of interference [33–35], direct-writing [35, 36], plasmonic devices [37], 'digital spatial light polarization converters' [38], or DMDs [40].

To generate more complex optical beams, we use a photoalignment method similar to [40] able to fabricate PBOEs characterized by an arbitrarily distributed optical axis. Our method relies on discretizing a PBOE's optical axis pattern into n segments each of which is associated with a single orientation. Therefore, we reconstruct this discretized version of the PBOE by sequentially exposing linearly polarized light patterns to specific regions of the alignment layer defined by the corresponding optical axis orientation. This method can be implemented via a DMD photoalignment method where the DMD is used to generate the required optical patterns. As displayed in figure 1, the rate at which the DMD produces varying light patterns is then synchronized to the rate at which a HWP rotates the polarization of a linearly polarized light beam. Doing so allows the reconstruction of

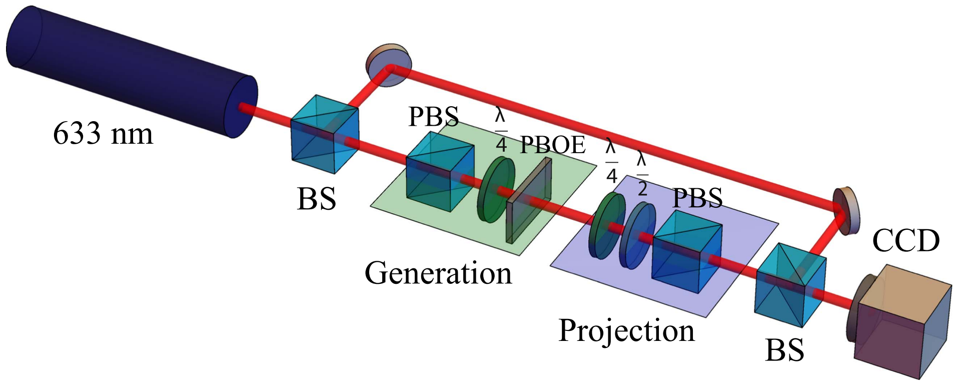

Figure 2. Characterization apparatus that includes a 633 nm laser beam going through a Mach–Zehnder-like interferometer where the desired beam is generated and its polarization is controlled. The group of elements that generates a specific beam includes a PBS, a quarter-wave plate ($\lambda/4$), and a PBOE; the group of elements that select a single polarization includes a quarter-wave plate, a half-wave plate ($\lambda/2$), and a PBS. The beam resulting from this interferometer is then observed using a CCD camera.

the PBOE's desired optical axis onto its photoalignment layer. Additional systems of lenses are added to the setup in order to refine the quality of the alignment. The first system consists of a set of two cylindrical lenses effectively rotating the beam by 90° and enlarging its size by a factor of three in order to make it uniformly cover the DMD's display. The second set of lenses consists of a 4-*f* system of two spherical lenses imaging the pattern reflected by the DMD onto the sample's alignment layer while enlarging it by a factor of 2.5 thus exposing the PBOE's frame to a rectangular beam with a length of 0.9 cm and a width of 1.6 cm. Moreover, using an iris, only the brightest diffraction orders of the pattern reflected by the DMD are selected in order to increase the resolution of the image projected on the sample. After the azodye layers are aligned, NLC (6CHBT) are inserted into the structural frame's cavity which is later sealed using epoxy glue. Finally, wires are soldered on the edge of each plate using an alloy composed of 97% indium and 3% silver.

In order to fully characterize the beams generated by the manufactured PBOEs (transverse intensity, phase, and polarization profiles), we investigate the modulation of a beam with a Gaussian profile and a wavelength of 633 nm with the setup shown in figure 2. Prior to modulating the beam with the device, we modify its polarization by using a polarizing beam splitter (PBS) and a quarter-wave plate (QWP, $\lambda/4$). This PBS-QWP combination allows us to send either horizontally or circularly polarized light through the PBOE. Hence, we are able to generate several sorts of beams along with their associated superposition combinations. After the desired beam is generated, it goes through a QWP, HWP ($\lambda/2$), and PBS combination to investigate the various polarization components of the generated transverse beam's profile [45]. Finally, a reference Gaussian beam, which was split from the beam by a non-PBS before the first QWP, is made to interfere with one of the output beam's polarization components, thus making its phase profile become observable in the resulting interference pattern. The reference beam can be blocked when the setup needs to be used only to investigate the intensity profile of the beams generated by the PBOEs. The resulting intensity or interference profiles are then recorded with a CCD camera.

The devices' transmission efficiencies were also evaluated using this apparatus. These efficiencies usually go up to 72%. However, most losses are associated with an incident beam's reflections on the device's glass substrates and can be reduced by applying an anti-reflection coating on the optical element. Doing so would allow the PBOE's transmission efficiency to reach a value closer to its conversion efficiency, which can reach values as high as 97%.

4. *q*-plates

4.1. $q = 1$-plate

To test the proposed method, we fabricate a standard $q = 1$-plate, which is able to generate a vortex beam with an OAM value of ± 2. The device was fabricated using a $n = 64$ pattern method and was designed to imprint a transverse phase of $\pm 2\varphi$ onto an incoming Gaussian beam. The device's optical axis distribution and its corresponding added geometric phase profile are shown in figure 3. The device's expected transmission profile when placed between two linear polarizers is also displayed along with an image of the actual sample placed between such polarizers.

As a first test, we electrically tuned the $q = 1$-plate to an optical retardation of $\delta = \pi$, which, according to equation (2), results in the entire input beam obtaining a phase profile of $\pm 2\varphi$. This leads to a phase singularity in the beam center imprinted onto the incident Gaussian input beam. Such beams are known as hypergeometric Gaussian beams [44]. The intensity and polarization profile of a beam resulting from illuminating the tuned $q = 1$-plate with circularly polarized light is shown in figure 3(b)-(i). As expected, the beam is circularly polarized and possesses a donut-like intensity profile.

As investigated previously, q-plates can be used to generate space-varying polarized light beams, namely vector vortex [45] and Poincaré beams [46]. When linearly polarized

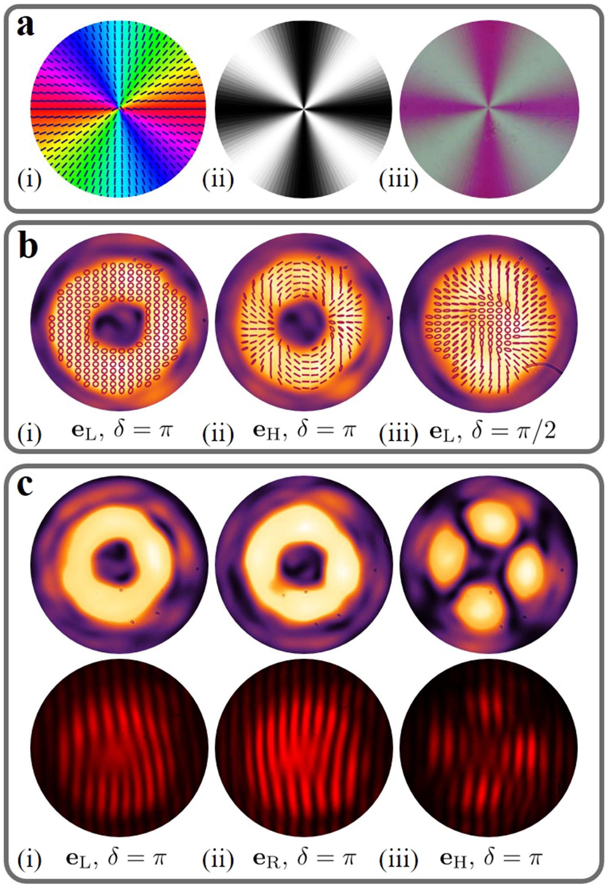

Figure 3. (a) (i) Optical axis distribution $\alpha(\rho, \varphi)$ of the $q = 1$-plate with the corresponding geometric phase $2\alpha(\rho, \varphi)$, shown in hue colors, added onto an incoming beam; (ii) expected transmission when the sample is placed between two polarizers; (iii) observed transmission pattern. (b) Far-field intensity and polarization profiles of the beams generated using the fabricated plate. The input polarization and tuning of the q-plate are indicated for each case. (i) Uniformly right-handed circularly polarized $\ell = 2$ beam; (ii) 'dipole' vector vortex beam; (iii) 'spiral' Poincaré beam. (c) Intensities and interference patterns with a plane wave of beams generated using (i) left-handed circularly, (ii) right-handed circularly, and (iii) horizontally polarized input light beams.

light is sent through a tuned q-plate, a so-called vector vortex beam is produced. In the case of a horizontally polarized input and a $q = 1$-plate, one obtains a vector beam defined by a linear polarization with an orientation given by twice the azimuthal coordinate. This specific beam is commonly referred to as a 'dipole'-polarization beam as its polarization pattern resembles the field pattern of a dipole (see figure 3(b)-(ii)).

If the q-plate is tuned to an optical retardation of $\delta = \pi/2$, the resulting beam consists of an equally weighted superposition of a converted and a non-converted component as seen in equation (2). Such a detuned q-plate's output beam is depicted in figure 3(b)-(iii). Here, the beam consists of an equally weighted superposition of a Gaussian beam and an $\ell = 2$ vortex beam. The equal composition is clearly seen through the beam's relatively flat-top central intensity that quickly decreases as it reaches the radius where the $|\ell| = 2$ vortex beam's intensity profile starts to drop. This output also corresponds to the Poincaré beam that can be generated using a $q = 1$-plate [46]. In our case, the resulting Poincaré beam is defined by a polarization profile resembling a spiral, a result which is indeed experimentally observed and depicted in figure 3(b)-(iii).

To observe the generated beam's transverse phase structure, the reference arm in figure 2 was used to perform interferometric measurements. A right-handed circularly polarized beam characterized by the index $\ell = 2$ was generated at the output of the first arm. When it was interfered with an intentionally slightly misaligned Gaussian reference beam, the interference pattern displayed in figure 3(c)-(i) was obtained. The misaligned interference pattern reveals a pitchfork with three tines. Given that the interference between a plane wave and a beam with a phase-front defined by ℓ intertwined helices results in a pitchfork interference pattern consisting of $\ell + 1$ tines [23, 28, 31], the recorded structure confirms that the beam has an ℓ value of 2. When a left-handed circularly polarized beam having an index of $\ell = -2$ was generated and interfered with the Gaussian reference beam, we obtained the pattern in figure 3(c)-(ii) which exhibits a similar pitchfork of opposite orientation as it carries OAM of opposite sign.

The QWP before the q-plate was then oriented to provide horizontally polarized light to the $q = 1$-plate, thus again generating the vector vortex beam seen in figure 3(b)-(ii). After projecting onto the horizontal component of the resulting beam by a second PBS, we find the expected four lobes defined by two possible distinct phases in the vicinity of either 0 or π. As a result, the interference fringes observed in the region separating the lobes are out of phase as observed in figure 3(c)-(iii).

All tests examining the intensity, phase, and polarization profiles of beams generated using the manufactured $q = 1$ plate reveal that the properties of these beams are in excellent agreement with their corresponding expected and well-established results.

4.2. High OAM device: $q = 100$-plate

We further demonstrate the method's ability to fabricate highly complex q-plates by manufacturing a device defined by a high topological charge, namely a $q = 100$-plate able to generate optical beams characterized by ± 200 units of OAM. Devices able to generate extreme high-order modes are good demonstrations of the ability to explore the unbounded nature of OAM. They can also be used to produce photonic gears which can potentially be useful in optical/quantum metrology [57, 58]. Due to the relatively high resolution needed to fabricate the device associated with the high frequency at which its optical axis varies, the q-plate was made using a lower reconstruction resolution consisting of a four step discretization method. The high degree at which the q-plate's optical axis orientation varies results in the formation of a Moiré pattern in the plate's added phase. Thus, for practical reasons, the device's center is refrained from being exposed to

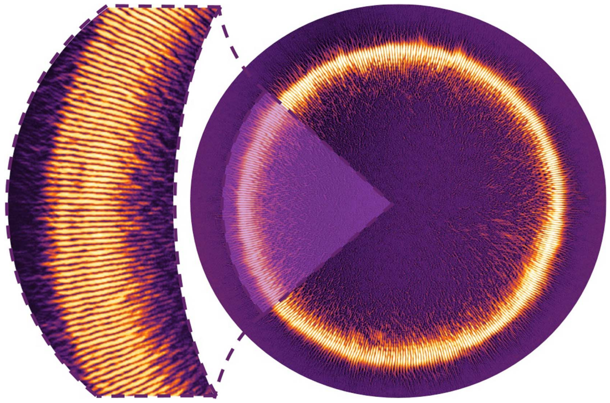

Figure 4. A 400 petal beam generated using a $q = 100$-plate fabricated using the procedure described in the text.

an incident light beam. This technique is often employed in many areas of beam shaping involving the fabrication of elements defined by abrupt variations in the phase aimed to be added to a beam [58, 59]

We demonstrate the q-plate's performance by feeding horizontally polarized light to it and only selecting the generated beam's horizontal polarization component, which should consist of 400 lobes. As depicted in figure 4, all 400 lobes of the generated beam are present, clearly defined, and uniformly shaped across the beam's profile.

5. Generation of complex structured beams

5.1. Bessel beams

After verifying that our method works, we continue using it to fabricate an extensive range of PBOEs in a way that has not been possible before. We first fabricate a PBOE generating a Bessel beam defined by parameters of $k_\rho = 5\ \ (\mathrm{mm})^{-1}$ and $\ell = 1$ using a $n = 32$ pattern method. Similarly to the q-plate described above, we show our device's optical axis distribution along with the corresponding geometric phase modulation as well as its observed appearance between two crossed polarizers in figure 5(a).

As Bessel beams exhibit their defining characteristics at their focus, we modified the characterization apparatus (depicted in figure 2) to first enlarge the beam and illuminate a wider region of the device to then weakly focus it using a 1000 mm lens. Thus, we are able to better resolve the characteristics in its focal region. The right-handed and left-handed circular components of this beam have a phase with a radial dependence given by $k_\rho \rho$ and $-k_\rho \rho$, thus it will exhibit converging and diverging lensing behaviors, respectively. As a result, the Bessel beam attributed to the right-handed component will be seen to focus before the one attributed to the left-handed component. Figure 5(b) shows the intensity profile of both circular polarizations at their respective foci. Since $\mathbf{e}_\mathrm{R}$ focuses closer to the plate, it forms a tighter Bessel beam than the one formed by $\mathbf{e}_\mathrm{L}$.

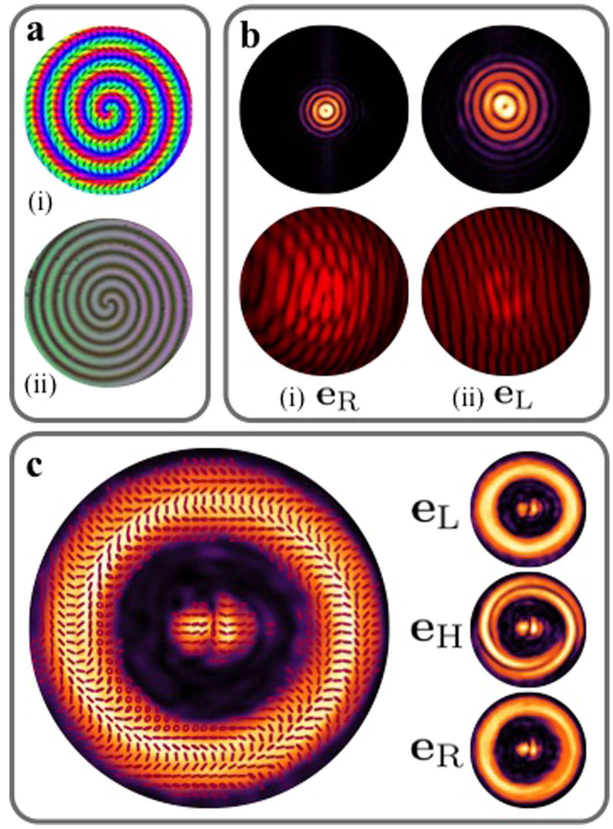

Figure 5. (a) (i) Optical axis distribution $\alpha(\rho, \varphi)$ of a PBOE generating a Bessel beam defined by parameters of $k_\rho = 5\ \ (\mathrm{mm})^{-1}$ and $\ell = 1$ along with the corresponding geometric phase $2\alpha(\rho, \varphi)$, which is shown in hue colors; (ii) its observed transmission between two polarizers. (b) Experimentally observed intensity and interference pattern of the (i) right- and (ii) left-handed circular components of the generated beam at each of their foci. (c) Reconstructed polarization profile of a generated beam using the Bessel PBOE. Measured intensities for $\mathbf{e}_\mathrm{L}$, $\mathbf{e}_\mathrm{H}$, and $\mathbf{e}_\mathrm{R}$ components are depicted on the right side.

To examine the phase of the generated beams, we recorded interference patterns resulting from the interference between the converted circular components of the beams and a reference beam with a uniform phase front (see figure 5(b)). The interference patterns exhibit circular discontinuities, which are attributed to the fact that each ring appearing in a Bessel beam's intensity profile is out of phase with its adjacent rings. Moreover, these patterns are defined by a pitchfork consisting of two tines, which is a sign that the beam carries an absolute OAM value of 1. In our experimental images these features are clearly observed for both components of the generated Bessel beam. In addition, the different orientation of the pitchfork for each component demonstrates the opposite sign of their OAM quanta.

Finally, we explore the ability to use the fabricated device as a mean to generate space-varying polarized light beams. In particular, we examine the polarization of an emitted beam consisting of equally weighted circular polarization components in a region where both components

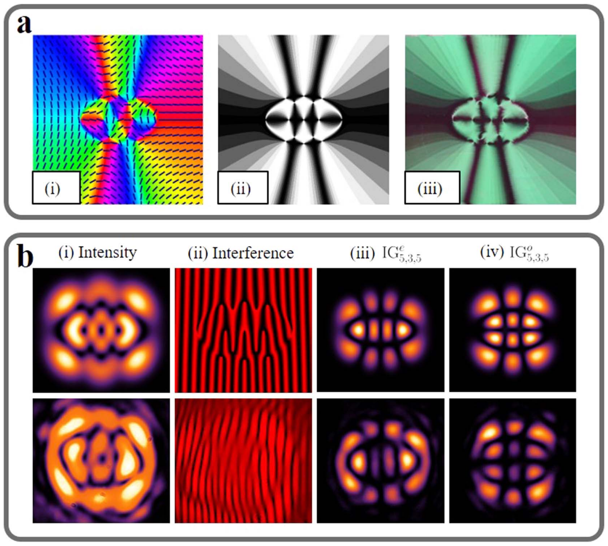

Figure 6. (a) (i) Optical axis distribution $\alpha(u, v)$, and the corresponding geometric phase $2\alpha(u, v)$ shown in hue colors; (ii) expected device appearance between two crossed polarizers; (iii) image of the $IG^{-}_{5,3,5}$ PBOE. (b) Expected (top) and experimental (bottom): (i) intensity patterns of the completely converted component of the beam produced by the fabricated $IG^{-}_{5,3,5}$ PBOE; (ii) corresponding fringes resulting from the interference of this beam with a plane wave. Theoretical intensity profiles of the (iii) even and (iv) odd IG modes and their recovered experimental intensity profiles.

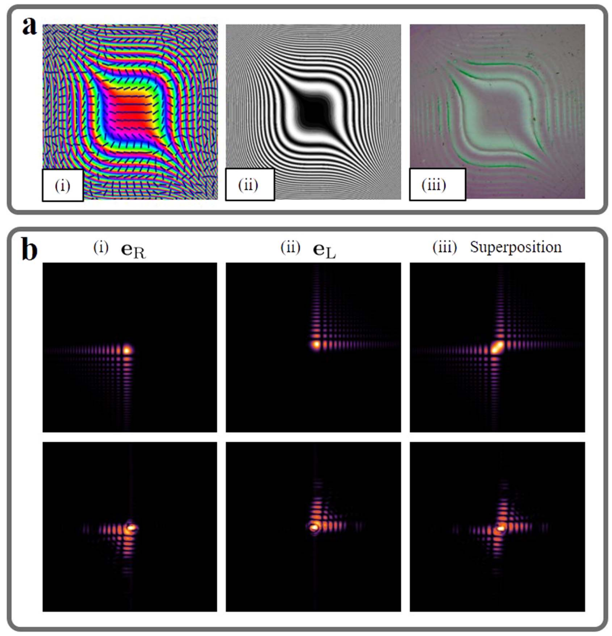

Figure 7. (a) (i) Optical axis distribution $\alpha(x, y)$ and the corresponding geometric phase $2\alpha(x, y)$, which is shown in hue colors; (ii) expected appearance between two crossed polarizers; (iii) image of the device generating a 2D Airy beam. (b) Expected (top) and observed (bottom) intensity profiles of the (i) right-handed circular polarization $\mathbf{e}_{\mathrm{R}}$, (ii) left-handed circular polarization $\mathbf{e}_{\mathrm{L}}$, and (iii) a superposition of both components of the generated Airy beam.

perfectly overlap. The resulting beam along with its reconstructed complex polarization profile is shown in figure 5(c). In addition to azimuthal variations in the polarization pattern attributed to the beam's azimuthally dependent phase, one can also see the effects of the radial dependence of the beam's phase through radial variations in the beam's transverse polarization profile. This feature can be made more visible if the beam is projected onto different polarization components. Namely, both circular components ($\mathbf{e}_{\mathrm{L}}$ and $\mathbf{e}_{\mathrm{R}}$) have a uniform appearance over the beam's cross-section, yet the linear component $\mathbf{e}_{\mathrm{H}}$ is found to form intertwined spirals.

5.2. IG beams

Using our custom alignment method, we were able to fabricate a device producing an $IG^{-}_{5,3,5}$ beam. Again, we used a $n = 32$ pattern method in the fabrication procedure to discretize the required continuous modulation. In figure 6(a) the PBOE's desired optical axis along with the corresponding added geometric phase are shown. The device's expected appearance when placed between two crossed linear polarizers is also displayed together with an image of the actual sample. The IG-PBOE's characterization was performed similarly to the previous ones. The expected and experimentally recorded intensities and interference patterns with a plane wave were examined and are shown in figure 6(b). To verify the polarization properties of the generated beams, we feed linearly polarized light into the perfectly tuned device and recover the resulting beam's even IG mode and its odd IG mode. As each of these modes is attributed to a linear polarization component, we were able to recover them by accordingly modifying the orientation of the setup's HWP. These recovered beams along with their corresponding theoretical transverse intensity profiles are shown in figure 6(b).

5.3. Airy beams

As a final demonstration of the flexibility of our fabrication method, we reproduce the fabrication of PBOEs producing Airy beams as performed in [60]. More specifically, we manufactured a device designed to add a phase of $\Phi_{\mathrm{Ai}}(x, y)$ defined in equation (3). The employed parameters were $f = 500$ mm, $\lambda = 633$ nm, $x_0 = y_0 = 60$ μm. Similar to the earlier findings, we display in figure 7 the PBOE's optical axis distribution and the corresponding geometric phase along with its expected and observed appearance between two crossed polarizers. Each polarization component generated by such a device will appear to be inverted with respect to the other. This inversion is clearly depicted in the intensity patterns of the generated beams shown in figure 7(b) along with their corresponding expected appearance, which are in excellent agreement.

6. Conclusion

In conclusion, we have devised and implemented a DMD-based photoalignment method to fabricate liquid crystal PBOEs defined by arbitrary optical axis spatial distributions. These PBOEs are more compact, cost-effective, and responsive to phase inversions than other beam shaping devices restricted to laboratory-scale usage. In particular, we manufactured devices capable of generating OAM-carrying, Bessel, IG, and Airy beams. Moreover, our generation of complex patterns with high resolution displays our ability to produce arbitrary beam patterns. These complex beams are characterized by distinct transverse intensity, phase, and polarization profiles along with the high conversion efficiency required for many applications such as quantum information and optical tweezers. For instance, cascading these PBOEs along with suitably fast Pockels cells may be used for ultra-fast (at gigahertz rate) and super-dense telecommunications.

Acknowledgments

The authors thank Sergei Slussarenko and Svetlana Lukishova for useful advice and discussions.

References

[1] He H, Friese M, Heckenberg N and Rubinsztein-Dunlop H 1995 *Phys. Rev. Lett.* **75** 826
[2] Padgett M and Bowman R 2011 *Nat. Photon.* **5** 343
[3] Hell S W and Wichmann J 1994 *Opt. Lett.* **19** 780
[4] Gibson G, Courtial J, Padgett M J, Vasnetsov M, Pas'ko V, Barnett S M and Franke-Arnold S 2004 *Opt. Express* **12** 5448
[5] Bozinovic N, Yue Y, Ren Y, Tur M, Kristensen P, Huang H, Willner A E and Ramachandran S 2013 *Science* **340** 1545
[6] Siviloglou G, Broky J, Dogariu A and Christodoulides D 2007 *Phys. Rev. Lett.* **99** 213901
[7] Durnin J, Miceli J Jr and Eberly J 1987 *Phys. Rev. Lett.* **58** 1499
[8] Baumgartl J, Mazilu M and Dholakia K 2008 *Nat. Photon.* **2** 675
[9] McGloin D and Dholakia K 2005 *Contemp. Phys.* **46** 15
[10] Dorn R, Quabis S and Leuchs G 2003 *Phys. Rev. Lett.* **91** 233901
[11] Wang H, Shi L, Lukyanchuk B, Sheppard C and Chong C T 2008 *Nat. Photon.* **2** 501
[12] Freund I 2005 *Opt. Commun.* **249** 7
[13] Bauer T, Banzer P, Karimi E, Orlov S, Rubano A, Marrucci L, Santamato E, Boyd R W and Leuchs G 2015 *Science* **347** 964
[14] Heckenberg N, McDuff R, Smith C and White A 1992 *Opt. Lett.* **17** 221
[15] Bolduc E, Bent N, Santamato E, Karimi E and Boyd R W 2013 *Opt. Lett.* **38** 3546
[16] Maurer C, Jesacher A, Fürhapter S, Bernet S and Ritsch-Marte M 2007 *New J. Phys.* **9** 78
[17] Galvez E J, Khadka S, Schubert W H and Nomoto S 2012 *Appl. Opt.* **51** 2925
[18] Hornbeck L J 1990 *33rd Annual Technical Symp.* (International Society for Optics and Photonics) pp 86–103
[19] Arlt J and Dholakia K 2000 *Opt. Commun.* **177** 297
[20] Mansuripur M, Zakharian A R and Wright E M 2011 *Phys. Rev.* A **84** 033813
[21] Kobayashi H, Nonaka K and Kitano M 2012 *Opt. Express* **20** 14064
[22] Radwell N, Hawley R, Götte J and Franke-Arnold S 2016 *Nat. Commun.* **7** 10564
[23] Marrucci L, Manzo C and Paparo D 2006 *Phys. Rev. Lett.* **96** 163905
[24] Allen L, Beijersbergen M W, Spreeuw R and Woerdman J 1992 *Phys. Rev.* A **45** 8185
[25] Bouchard F, Mand H, Mirhosseini M, Karimi E and Boyd R W 2014 *New J. Phys.* **16** 123006
[26] Marrucci L, Manzo C and Paparo D 2006 *Appl. Phys. Lett.* **88** 221102
[27] Bomzon Z, Kleiner V and Hasman E 2001 *Opt. Lett.* **26** 1424
[28] Marrucci L, Karimi E, Slussarenko S, Piccirillo B, Santamato E, Nagali E and Sciarrino F 2011 *J. Opt.* **13** 064001
[29] Karimi E, Schulz S A, De Leon I, Qassim H, Upham J and Boyd R W 2014 *Light: Sci. Appl.* **3** e167
[30] Lin D, Fan P, Hasman E and Brongersma M L 2014 *Science* **345** 298
[31] Slussarenko S, Murauski A, Du T, Chigrinov V, Marrucci L and Santamato E 2011 *Opt. Express* **19** 4085
[32] Slussarenko S, Piccirillo B, Chigrinov V, Marrucci L and Santamato E 2013 *J. Opt.* **15** 025406
[33] Nys I, Beeckman J and Neyts K 2015 *Soft Matter* **11** 7802–8
[34] Kawai K, Sakamoto M, Noda K, Sasaki T, Kawatsuki N and Ono H 2016 *J. Appl. Phys.* **119** 123102
[35] Kim J, Li Y, Miskiewicz M N, Oh C, Kudenov M W and Escuti M J 2015 *Optica* **2** 958–64
[36] Miskiewicz M N and Escuti M J 2014 *Opt. Express* **22** 12691–706
[37] Guo Y, Jiang M, Peng C, Sun K, Yaroshchuk O, Lavrentovich O and Wei Q H 2016 *Adv. Mater.* **28** 2352
[38] De Sio L, Roberts D E, Liao Z, Nersisyan S, Uskova O, Wickboldt L, Tabiryan N, Steeves D M and Kimball B R 2016 *Opt. Express* **24** 18297–306
[39] Nikolova L and Ramanujam P S 2009 *Polarization Holography* (Cambridge: Cambridge University Press)
[40] Wu H, Hu W, Hu H-C, Lin X-W, Zhu G, Choi J-W, Chigrinov V and Lu Y-Q 2012 *Opt. Express* **20** 16684
[41] Pancharatnam S 1956 *Proc. Indian Academy of Sciences-section* A vol 44 (Berlin: Springer) pp 398–417
[42] Berry M V 1984 *Proc. R. Soc.* A **392** 45–57
[43] Bhandari R 1997 *Phys. Rep.* **281** 1
[44] Karimi E, Piccirillo B, Marrucci L and Santamato E 2009 *Opt. Lett.* **34** 1225
[45] Cardano F, Karimi E, Slussarenko S, Marrucci L, de Lisio C and Santamato E 2012 *Appl. Opt.* **51** C1
[46] Cardano F, Karimi E, Marrucci L, de Lisio C and Santamato E 2013 *Opt. Express* **21** 8815
[47] Durnin J 1987 *J. Opt. Soc. Am.* A **4** 651
[48] Bandres M A and Gutiérrez-Vega J C 2004 *Opt. Lett.* **29** 144
[49] Bandres M A and Gutiérrez-Vega J C 2004 *J. Opt. Soc. Am.* A **21** 873
[50] Krenn M, Fickler R, Huber M, Lapkiewicz R, Plick W N, Ramelow S and Zeilinger A 2013 *Phys. Rev.* A **87** 012326
[51] Plick W N, Krenn M, Fickler R, Ramelow S and Zeilinger A 2013 *Phys. Rev.* A **87** 033806
[52] Berry M V and Balazs M V 1979 *Am. J. Phys.* **4** 264–7
[53] Siviloglou G A and Christodoulides D N 2007 *Opt. Lett.* **32** 979
[54] Bouchard F, De Leon I, Schulz S A, Upham J, Karimi E and Boyd R W 2014 *Appl. Phys. Lett.* **105** 101905

[55] Chigrinov V G, Kozenkov V M and Kwok H S 2008 *Photoalignment of Liquid Crystalline Materials: Physics and Application* (New York: Wiley)
[56] Nersisyan S, Tabiryan N, Steeves D M and Kimball B R 2009 *Opt. Express* **17** 11926
[57] D'Ambrosio V, Spagnolo N, Del Re L, Slussarenko S, Li Y, Kwek L C, Marrucci L, Walborn S P, Aolita L and Sciarrino F 2013 *Nat. Commun.* **4** 2432
[58] Fickler R, Lapkiewicz R, Plick W N, Krenn M, Schaeff C, Ramelow S and Zeilinger A 2012 *Science* **338** 640
[59] Grillo V, Gazzadi G C, Mafakheri E, Frabboni S, Karimi E and Boyd R W 2015 *Phys. Rev. Lett.* **114** 034801
[60] Wei B-Y, Chen P, Hu W, Ji W, Zheng L-Y, Ge S-J, Ming Y, Chigrinov V and Lu Y-Q 2015 *Sci. Rep.* **5** 17484

Chapter 3

OAM sorters

This chapter is based on the following papers:

1. **H. Larocque**, J. Gagnon-Bischoff, D. Mortimer, Y. Zhang, F. Bouchard, J. Upham, V. Grillo, R. W. Boyd, and E. Karimi, "Generalized optical angular momentum sorter and its application to high-dimensional quantum cryptography", *Optics Express* **25**, 19832 (2017).

   DOI: https://doi.org/10.1364/OE.25.019832

2. V. Grillo, A. H. Tavabi, F. Venturi, **H. Larocque**, R. Balboni, G. C. Gazzadi, S. Frabboni, P.-H. Lu, E. Mafakheri, F. Bouchard, R. E. Dunin-Borkowski, R. W. Boyd, M. P. J. Lavery, M. J. Padgett, and E. Karimi, "Measuring an electron beam's orbital angular momentum spectrum", *Nature Communications* **8**, 15536 (2017).

   DOI: https://doi.org/10.1038/ncomms15536

3.1 Measuring a wave's OAM

The usefulness of OAM-carrying waves in modern science primarily arises from the fact that they are orthogonal to one another. More specifically, a wave carrying a specific amount of OAM cannot be expressed as a superposition of other waves carrying different amounts of OAM. This feature allows waves to be effectively decomposed in terms of their OAM content and the ability to perform such a decomposition makes OAM a valid quantity in which information can be encoded. In fact, optical OAM is nowadays a common information carrier used in studies regarding optical communications. This quantity is also of interest in electron waves given that an electron's OAM content can be modified by magnetic structures, thus making structured electron wave's of significant interest in works pertaining to materials science. Such applications, however, require a reliable and efficient method to decompose a wave's OAM spectrum in order to extract the information it carries.

3.2 Phase-flattening measurements

A very simple method to analyze a wave's OAM spectrum consists of using the generation schemes introduced in the previous chapter to remove a certain amount of OAM from the beam as opposed to adding it. More specifically, when a wave goes through a device designed to remove an amount of OAM corresponding to the amount it carries, its transverse twisted phase profile is effectively removed or "flattened". As a result, the wave loses its central phase singularity and acquires a Gaussian-like intensity profile in its far field upon free-space propagation.

Phase-flattening procedures, which rely on the above process and were first demonstrated in [38], essentially consist of making a structured wave propagate through a sequence of such devices designed to remove different amounts of OAM, and thereafter through an aperture aligned along the beam's centre. Should the wave contain the removed amount of OAM in its modal composition, this component will acquire a Gaussian profile upon propagation and thereby be able to go through the aperture. All of the wave's other OAM components will effectively have some but not all of their OAM removed. As a result, these components will still have a phase singularity and thereby an intensity null at their centre once they reach the aperture. For this reason, they will mostly be blocked by the latter. Therefore, by comparing the total power, or particle flux, of the wave after the aperture with respect to that of the entire wave, one is able to extract the relative weight of the analyzed component in the examined wave. Furthermore, performing such measurements for different OAM components allows one to reconstruct the wave's OAM spectrum.

Though effective, phase-flattening measurements are defined by two major flaws. First, phase-flattening procedures are biased against waves with high absolute values of OAM. That is, the more a wave carries OAM, the less its flattened profile will be Gaussian-like and the more the converted beam will be blocked by the aperture [39]. Therefore, this flaw causes phase-flattening schemes to be less efficient for beams that carry large OAM values. The second flaw relates to the use of phase-flattening measurements in quantum experiments and applications. In these cases, a wave in a superposition of OAM-carrying modes can also be seen as a particle in a superposition of quantum states defined by different OAM values. As such particles go through phase-flattening schemes, their quantum states are projected onto a single OAM component, which, depending on the OAM removed by the device, may or may not let the particle go through the aperture. This causes a lot of particles to be "wasted" during the OAM measurement process and intrinsically causes the method to be less efficient.

3.3 OAM sorters

In recent years, the flaws that riddle phase-flattening schemes have motivated the development of more efficient OAM detection methods. One of them consists of so-called OAM sorters [40]. In essence, OAM sorters are devices that spatially resolve, or sort, a wave's OAM components on a screen. Based on the intensity of each sorted component, one can obtain the relative weight of each OAM mode in the total wave. OAM sorters overcome some phase-flattening deficiencies given that they do not rely on blocking parts of the propagating wave.

3.3.1 Conformal Mapping

A sorter's ability to spatially resolve OAM components relies on a conformal mapping performed by two confocal phase elements which essentially "unwrap" the beam. As a result, this mapping effectively allows any azimuthal variations contained in the wave's profile to be mapped along a Cartesian coordinate. These azimuthal variations include the azimuthally-dependent phase of OAM-carrying beams, and thereby causes them to be reshaped into waves that have a linear phase gradient as shown in Fig. 3.1(a). These unwrapped waves defined by linear phase gradients essentially consist of planes waves with titled wavefronts, where the degree to which the wave is titled depends on the original amount of OAM it carried. Such tilted waves can thereafter be simply separated by making them propagate through a lensing

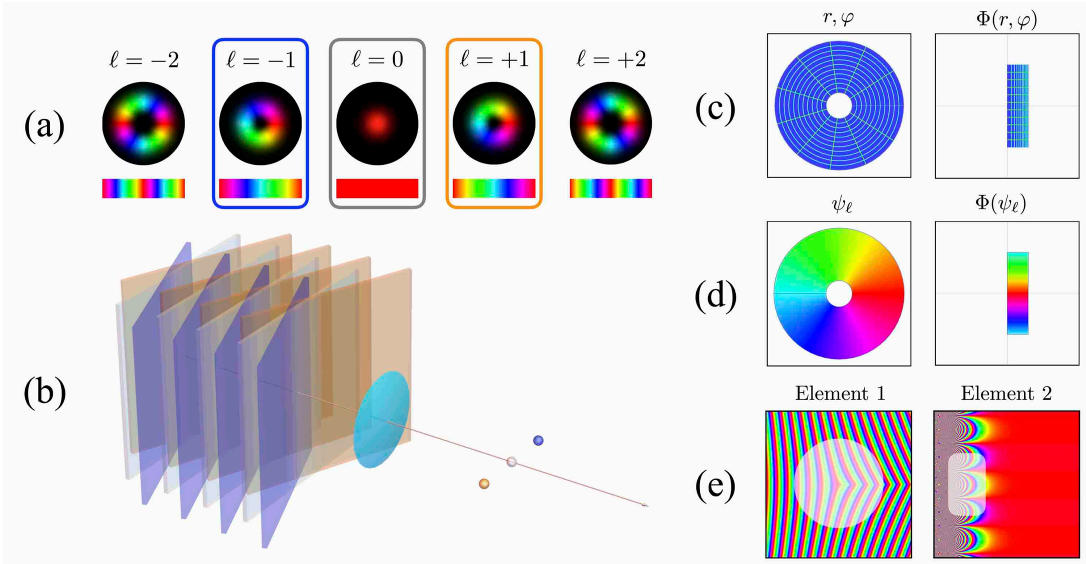

Figure 3.1: **Conformal-mapping performed by an OAM sorter**. (a) Transverse profiles of OAM-carrying waves placed above their phase profiles plotted against the azimuthal coordinate. (b) Focal points of plane waves with tilted wavefronts following their propagation through a lens. The depicted waves could be equivalent to an unwrapped OAM-carrying beam shown in (a), which are enclosed in boxes that are correspondingly coloured. (c) Effect of a log-polar mapping Φ on the radial (light blue) and azimuthal (green) coordinates in complex space. (d) Effect of a spatial log-polar mapping Φ on the phase profile of an OAM-carrying wave ψ_ℓ. (e) Confocal phase elements used to perform a spatial log-polar mapping. Regions where the original and unwrapped beams hit each element are highlighted in white.

element as depicted in Fig. 3.1(b). This unwrapping process followed by a lens consists of the fundamental principle upon which most OAM-sorters are based.

In OAM sorters, the conformal mapping used to unwrap the beam usually consists of a log-polar mapping which we will denote by Φ. Its action on a complex variable $z = x + iy = \rho e^{i\phi}$, can effectively be represented by the following equation

$$z \mapsto \Phi(z) = \ln(z) = \ln(\rho e^{i\phi}) = \ln(\rho) + i\phi, \tag{3.1}$$

where x is the real part of z, y is the imaginary part of z, $\rho = \sqrt{x^2 + y^2}$ is the amplitude or the absolute value of z, and $\phi = \arctan(y/x)$ is the phase or the argument of z. From this action, we can clearly see that Φ effectively maps variations in the amplitude of z to variations in the real part of a complex number. Likewise, variations in the argument of z are mapped to variations in the imaginary part. This action can also be interpreted as mapping variations of the radial coordinate in complex space to a Cartesian coordinate, or the real axis, and variations along the azimuthal coordinate in complex space to the other Cartesian coordinate, or the imaginary axis. A visual depiction of this action can be found in Fig. 3.1(c). The log-polar mapping used in sorters consists of a mapping similar to the one that acts on a complex number, with the exception that it acts on the coordinates of a real two-dimensional space as opposed to the two dimensions of a complex space. As a result, this causes the azimuthal phase variations of an OAM-carrying beam ψ_ℓ to be unwrapped once it is mapped to $\Phi(\psi_\ell)$ as illustrated in Fig. 3.1(d). In practice, this transformation can be achieved by means of two confocal phase elements whose phase structures are shown in Fig. 3.1(e) [41]. The first element performs the bulk of the unwrapping while the second one corrects for secondary modulational instabilities in the unwrapped beam in order to make it experience a more or less stable propagation afterwards.

To summarize the working principles of an OAM sorter, an integrative depiction that illustrates the propagation of a beam defined by OAM components of $\ell = \pm 5$ as it propagates through the various elements of an OAM sorter is shown in Fig. 3.2.

3.3.2 Extensions

The first OAM sorter was designed for optical beams and used computer generated holograms on spatial light modulators (SLM) as the required confocal phase elements [40]. This sorter, however, has a few short-comings. Namely, SLM holograms only work for one optical polarization which restrains the use of this sorter from beams that have interesting polarization structures. Furthermore, the sorted OAM components are defined by a certain amount of overlap which leads to a certain degree of "cross-talk" in the device, thereby reducing its performance in any real application.

These shortcomings motivated the development of several interesting extensions to this first sorter. The first of these developments consisted of integrating the required lensing effects into the two phase elements. This reduced the total amount of optical elements in the sorter to two and considerably reduced the device's footprint. Another advance consisted of replacing the two SLMs in the sorter by custom-made refractive elements akin to phase plates. This allowed the device to work under a co-linear configuration, as opposed to a diffractive one, while also enabling its use for arbitrary optical polarizations [42]. Developments were also made to reduce the device's cross-talk [43]. This was achieved by exposing the sorter's unwrapped beam to so-called

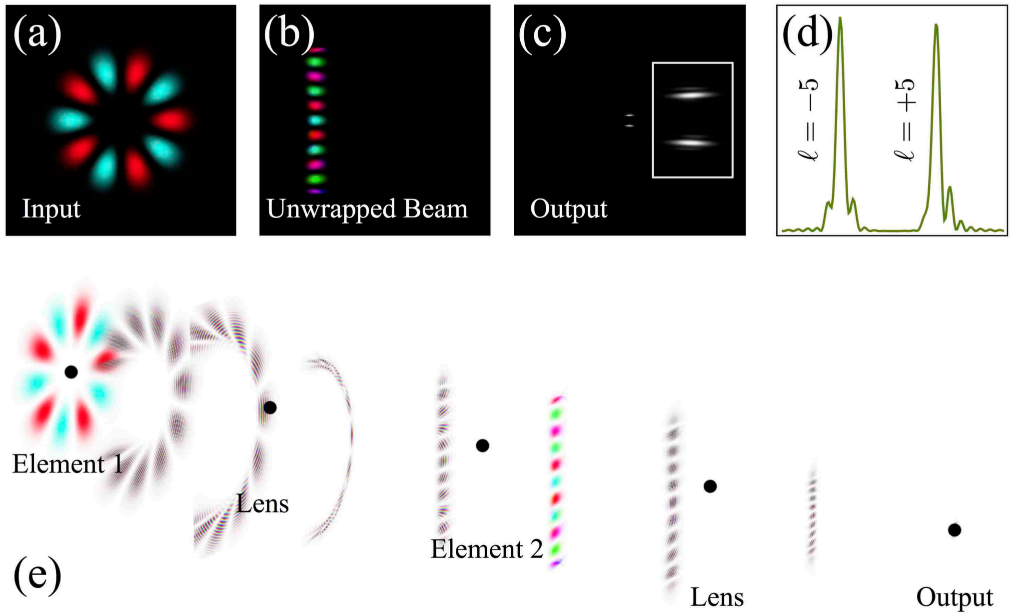

Figure 3.2: **Propagation of a structured wave through an OAM-sorter**. (a) The input structured wave consisting of a superposition of $\ell = \pm 5$ OAM modes. (b) The unwrapped beam. (c) The beam at the sorter's output. (d) The OAM spectrum obtained from the sorter. (e) The input beam hits the first of the sorter's phase elements, which along with a lens, unwraps the beam. The beam then hits the sorter's second phase element which corrects modulational instabilities. This correction completes the sorter's log-polar mapping and allows the unwrapped beam to experience a stable propagation. The unwrapped beam then hits a second lens which spatially resolves its initial OAM components.

"fan-out" optical elements [44]. The latter produce copies of the unwrapped beam, which essentially causes the total beam to have a greater spatial extent, yet phase variations that have the same spatial dependence as the original unwrapped beam. In fact, these variations are just periodically repeated due to the presence of the copies. These features cause the focused OAM components to be much more narrow, thereby considerably reducing their overlap and the sorter's cross-talk. Such developments have significantly increased the performance and the scalability of optical OAM sorters and has allowed them to be used in works pertaining to applications such as quantum key distribution (QKD).

The publications on which this chapter is based are two other extensions to an OAM-sorting scheme. The first one relies on using the liquid crystal devices mentioned in chapter 2 as the sorter's unwrapping and correcting phase elements [36]. The fact that these two elements add geometric phases to an optical beam imbues this sorting scheme with additional properties involving optical polarization. Namely, by bringing slight modifications to the phase profile of each element, one can create a sorter that is able to sort both an optical beam based on its OAM and polarization content. As further demonstrated, such features are advantageous in optical communications schemes that rely on both of these optical degrees of freedom to send information.

The second sorter extension consists of the implementation of a device that sorts the OAM content of an electron beam [45, 46]. This implementation was achieved by modifying each of the sorter's elements such that they would work on electron waves. Namely, the phase holograms that perform the sorter's conformal mapping were changed to SiN holograms that are commonly used in electron beam shaping. Likewise, the optical refractive lenses were replaced by a transmission electron microscope's (TEM) magnetic lenses. As further demonstrated in the corresponding publication, this electron sorter is of considerable interest in materials science given that it allows one to obtain an electron's OAM spectrum following its interaction with magnetic structures. Though this application is of significant interest in the characterization of materials via electron microscopy, the electron sorter's performance is fairly limited by aberrations. Therefore, future applications of this technology should be conducted with an aberration corrected electron beam [47, 48, 49] to ensure their optimal performance.

Generalized optical angular momentum sorter and its application to high-dimensional quantum cryptography

Hugo Larocque,[1] Jérémie Gagnon-Bischoff,[1] Dominic Mortimer,[1] Yingwen Zhang,[1] Frédéric Bouchard,[1] Jeremy Upham,[1] Vincenzo Grillo,[2] Robert W. Boyd,[1,3] and Ebrahim Karimi[1,4,*]

[1] *Department of Physics, University of Ottawa, 25 Templeton St., Ottawa, Ontario, K1N 6N5 Canada*
[2] *CNR-Istituto Nanoscienze, Centro S3, Via G Campi 213/a, I-41125 Modena, Italy*
[3] *Institute of Optics, University of Rochester, Rochester, New York, 14627, USA*
[4] *Department of Physics, Institute for Advanced Studies in Basic Sciences, 45137-66731 Zanjan, Iran*
[*] *ekarimi@uottawa.ca*

Abstract: The orbital angular momentum (OAM) carried by optical beams is a useful quantity for encoding information. This form of encoding has been incorporated into various works ranging from telecommunications to quantum cryptography, most of which require methods that can rapidly process the OAM content of a beam. Among current state-of-the-art schemes that can readily acquire this information are so-called OAM *sorters*, which consist of devices that spatially separate the OAM components of a beam. Such devices have found numerous applications in optical communications, a field that is in constant demand for additional degrees of freedom, such as polarization and wavelength, into which information can also be encoded. Here, we report the implementation of a device capable of sorting a beam based on its OAM and polarization content, which could be of use in works employing both of these degrees of freedom as information channels. After characterizing our fabricated device, we demonstrate how it can be used for quantum communications via a quantum key distribution protocol.

OCIS codes: (230.3720) Liquid-crystal devices; (260.6042) Singular optics; (270.5568) Quantum cryptography.

References and links

1. H. Rubinsztein-Dunlop, A. Forbes, M. Berry, M. R. Dennis, D. L. Andrews, M. Mansuripur, C. Denz, C. Alpmann, P. Banzer, T. Bauer, E. Karimi, L. Marrucci, M.J. Padgett, M. Ritsch-Marte, N. M. Litchinitser, N. P. Bigelow, C. Rosales-Guzmán, A. Belmonte, J. P. Torres, T. W. Neely, M. Baker, R. Gordon, A. Stilgoe, J. Romero, A. G. White, R. Fickler, A. E. Willner, G. Xie, B. McMorran, and A. M. Weiner, "Roadmap on structured light," J. Opt. **19**(1), 013001 (2016).
2. L. Allen, M. W. Beijersbergen, R. Spreeuw, and J. Woerdman, "Orbital angular momentum of light and the transformation of laguerre-gaussian laser modes," Phys. Rev. A **45**(11), 8185 (1992).
3. M. Krenn, R. Fickler, M. Fink, J. Handsteiner, M. Malik, T. Scheidl, R. Ursin, and A. Zeilinger, "Communication with spatially modulated light through turbulent air across vienna," New J. Phys. **16**(11), 113028 (2014).
4. J. Wang, J.-Y. Yang, I. M. Fazal, N. Ahmed, Y. Yan, H. Huang, Y. Ren, Y. Yue, S. Dolinar, M. Tur, and A. E. Willner, "Terabit free-space data transmission employing orbital angular momentum multiplexing," Nat. Photon. **6**(7), 488–496 (2012).
5. A. E. Willner, H. Huang, Y. Yan, Y. Ren, N. Ahmed, G. Xie, C. Bao, L. Li, Y. Cao, Z. Zhao, J. Wang, M. P. J. Lavery, M. Tur, S. Ramachandran, A. F. Molisch, N. Ashrafi, and S. Ashrafi, "Optical communications using orbital angular momentum beams," Adv. Opt. Photon. **7**(1), 66–106 (2015).
6. F. Tamburini, E. Mari, A. Sponselli, B. Thidé, A. Bianchini, and F. Romanato, "Encoding many channels on the same frequency through radio vorticity: first experimental test," New J. Phys. **14**(3), 033001 (2012).
7. A. Sit, F. Bouchard, R. Fickler, J. Gagnon-Bischoff, H. Larocque, K. Heshami, D. Elser, C. Peuntinger, K. Günthner, B. Heim, C. Marquardt, G. Leuchs, R. W. Boyd, and E. Karimi, "High-dimensional intra-city quantum cryptography with structured photons," arXiv preprint arXiv:1612.05195 (2016).
8. G. Vallone, V. D'Ambrosio, A. Sponselli, S. Slussarenko, L. Marrucci, F. Sciarrino, and P. Villoresi, "Free-space quantum key distribution by rotation-invariant twisted photons," Phys. Rev. Lett. **113**(6), 060503 (2014).
9. G. C. Berkhout, M. P. Lavery, J. Courtial, M. W. Beijersbergen, and M. J. Padgett, "Efficient sorting of orbital angular momentum states of light," Phys. Rev. Lett. **105**(15), 153601 (2010).

10. M. N. O'Sullivan, M. Mirhosseini, M. Malik, and R. W. Boyd, "Near-perfect sorting of orbital angular momentum and angular position states of light," Opt. Express **20**(22), 24444–24449 (2012).
11. M. Mirhosseini, M. Malik, Z. Shi, and R. W. Boyd, "Efficient separation of the orbital angular momentum eigenstates of light," Nat. Commun. **4**, 2781 (2013).
12. M. P. Lavery, D. J. Robertson, G. C. Berkhout, G. D. Love, M. J. Padgett, and J. Courtial, "Refractive elements for the measurement of the orbital angular momentum of a single photon," Opt. Express **20**(3), 2110–2115 (2012).
13. M. Mirhosseini, O. S. Magaña-Loaiza, M. N. O'Sullivan, B. Rodenburg, M. Malik, M. P. J. Lavery, M. J. Padgett, D. J. Gauthier, and R. W. Boyd, "High-dimensional quantum cryptography with twisted light," New J. Phys. **17**, 033033 (2015).
14. V. Grillo, A. H. Tavabi, F. Venturi, H. Larocque, R. Balboni, G. C. Gazzadi, S. Frabboni, P.-H. Lu, E. Mafakheri, F. Bouchard, R. E. Dunin-Borkowski, R. W. Boyd, M. P. J. Lavery, M. J. Padgett, and E. Karimi, "Measuring the orbital angular momentum spectrum of an electron beam," Nat. Commun. **8**, 15536 (2017).
15. B. J. McMorran, T. R. Harvey, and M. P. Lavery, "Efficient sorting of free electron orbital angular momentum," New J. Phys. **19**(2), 023053 (2017).
16. S. Pancharatnam, "Generalized theory of interference and its applications," Proc. Indian Acad. Sci. A **44**(6), 398–417 (1956).
17. M. V. Berry, "Quantal phase factors accompanying adiabatic changes," Proc. R. Soc. A **392**(1802), 45–57 (1984).
18. L. Marrucci, C. Manzo, and D. Paparo, "Pancharatnam-berry phase optical elements for wave front shaping in the visible domain: Switchable helical mode generation," Appl. Phys. Lett. **88**(22), 221102 (2006).
19. Z. Bomzon, V. Kleiner, and E. Hasman, "Pancharatnam–berry phase in space-variant polarization-state manipulations with subwavelength gratings," Opt. Lett. **26**(18), 1424–1426 (2001).
20. L. Marrucci, C. Manzo, and D. Paparo, "Optical spin-to-orbital angular momentum conversion in inhomogeneous anisotropic media," Phys. Rev. Lett. **96**(16), 163905 (2006).
21. E. Nagali, F. Sciarrino, F. De Martini, L. Marrucci, B. Piccirillo, E. Karimi, and E. Santamato, "Quantum information transfer from spin to orbital angular momentum of photons," Phys. Rev. Lett. **103**(1), 013601 (2009).
22. L. Marrucci, E. Karimi, S. Slussarenko, B. Piccirillo, E. Santamato, E. Nagali, and F. Sciarrino, "Spin-to-orbital conversion of the angular momentum of light and its classical and quantum applications," J. Opt. **13**(6), 064001 (2011).
23. E. Karimi, J. Leach, S. Slussarenko, B. Piccirillo, L. Marrucci, L. Chen, W. She, S. Franke-Arnold, M. J. Padgett, and E. Santamato, "Spin-orbit hybrid entanglement of photons and quantum contextuality," Phys. Rev. A **82**(2), 022115 (2010).
24. G. F. Walsh, "Pancharatnam-berry optical element sorter of full angular momentum eigenstate," Opt. Express **24**(6), 6689–6704 (2016).
25. H. Larocque, J. Gagnon-Bischoff, F. Bouchard, R. Fickler, J. Upham, R. W. Boyd, and E. Karimi, "Arbitrary optical wavefront shaping via spin-to-orbit coupling," J. Opt. **18**(12), 124002 (2016).
26. W. Hossack, A. Darling, and A. Dahdouh, "Coordinate transformations with multiple computer-generated optical elements," J. Mod. Opt. **34**(9), 1235–1250 (1987).
27. E. Karimi, B. Piccirillo, L. Marrucci, and E. Santamato, "Light propagation in a birefringent plate with topological charge," Opt. Lett. **34**(8), 1225–1227 (2009).
28. V. Chigrinov, A. Muravski, H. S. Kwok, H. Takada, H. Akiyama, and H. Takatsu, "Anchoring properties of photoaligned azo-dye materials," Phys. Rev. E **68**(6), 061702 (2003).
29. S. Nersisyan, N. Tabiryan, D. M. Steeves, and B. R. Kimball, "Fabrication of liquid crystal polymer axial waveplates for uv-ir wavelengths," Opt. Express **17**(14), 11926–11934 (2009).
30. H. Wu, W. Hu, H.-c. Hu, X.-w. Lin, G. Zhu, J.-W. Choi, V. Chigrinov, and Y.-q. Lu, "Arbitrary photo-patterning in liquid crystal alignments using dmd based lithography system," Opt. Express **20**(15), 16684–16689 (2012).
31. J. Kim, Y. Li, M. N. Miskiewicz, C. Oh, M. W. Kudenov, and M. J. Escuti, "Fabrication of ideal geometric-phase holograms with arbitrary wavefronts," Optica **2**(11), 958–964 (2015).
32. M. N. Miskiewicz and M. J. Escuti, "Direct-writing of complex liquid crystal patterns," Opt. Express **22**(10), 12691–12706 (2014).
33. T.-C. Poon and T. Kim, *Engineering Optics with MATLAB®* (World Scientific Publishing Co Inc, 2006).
34. C. H. Bennett and G. Brassard, "Quantum cryptography: Public key distribution and coin tossing," Theor. Comput. Sci. **560**, 7–11 (2014).
35. P. W. Shor and J. Preskill, "Simple proof of security of the bb84 quantum key distribution protocol," Phys. Rev. Lett. **85**(2), 441 (2000).
36. Y. Guo, M. Jiang, C. Peng, K. Sun, O. Yaroshchuk, O. Lavrentovich, and Q.-H. Wei, "High-resolution and high-throughput plasmonic photopatterning of complex molecular orientations in liquid crystals," Adv. Mater. (2016).
37. L. A. Romero and F. M. Dickey, "Theory of optimal beam splitting by phase gratings. i. one-dimensional gratings," J. Opt. Soc. Am. A **24**(8), 2280–2295 (2007).
38. D. Prongué, H.-P. Herzig, R. Dändliker, and M. T. Gale, "Optimized kinoform structures for highly efficient fan-out elements," Appl. Opt. **31**(26), 5706–5711 (1992).
39. L. De Sio, D. E. Roberts, Z. Liao, S. Nersisyan, O. Uskova, L. Wickboldt, N. Tabiryan, D. M. Steeves, and B. R. Kimball, "Digital polarization holography advancing geometrical phase optics," Opt. Express **24**(16), 18297–18306 (2016).

40. S. R. Nersisyan and N. V. Tabiryan, "Polarization imaging components based on patterned photoalignment," Mol. Cryst. Liq. Cryst. **489**(1), 156–482 (2008).
41. N. V. Tabiryan, S. V. Serak, D. E. Roberts, D. M. Steeves, and B. R. Kimball, "Thin waveplate lenses of switchable focal length-new generation in optics," Opt. Express **23**(20), 25783–25794 (2015).
42. N. V. Tabiryan, S. V. Serak, S. R. Nersisyan, D. E. Roberts, B. Y. Zeldovich, D. M. Steeves, and B. R. Kimball, "Broadband waveplate lenses," Opt. Express **24**(7), 7091–7102 (2016).
43. E. Karimi, S. A. Schulz, I. De Leon, H. Qassim, J. Upham, and R. W. Boyd, "Generating optical orbital angular momentum at visible wavelengths using a plasmonic metasurface," Light Sci. Appl. **3**(5), e167 (2014).
44. D. Lin, P. Fan, E. Hasman, and M. L. Brongersma, "Dielectric gradient metasurface optical elements," Science **345**(6194), 298–302 (2014).
45. Y. S. Rumala, G. Milione, T. A. Nguyen, S. Pratavieira, Z. Hossain, D. Nolan, S. Slussarenko, E. Karimi, L. Marrucci, and R. R. Alfano, "Tunable supercontinuum light vector vortex beam generator using a q-plate," Opt. Lett. **38**(23), 5083–5086 (2013).
46. G. Milione, M. P. Lavery, H. Huang, Y. Ren, G. Xie, T. A. Nguyen, E. Karimi, L. Marrucci, D. A. Nolan, R. R. Alfano, and A. E. Willner, "4× 20 Gbit/s mode division multiplexing over free space using vector modes and a q-plate mode (de) multiplexer," Opt. Lett. **40**(9), 1980–1983 (2015).

1. Introduction

The panoply of means for distinctively shaping light beams has significantly improved the performance of applications such as optical tweezers and communications, while also driving their usage in emerging fields like quantum cryptography [1]. Such advancements can be attributed to the several degrees of freedom that are used to characterize an optical beam, such as its wavelength, temporal profile, transverse spatial profile, and its polarization, which can often be naturally extended to the quantum description of light beams. For instance, a photon's angular momentum, which includes spin angular momentum (SAM) and orbital angular momentum (OAM), is one such property. SAM is attributed to a beam's polarization, which is associated with the vectorial nature of light, whereas OAM is related to the beam's transverse phase profile. Namely, beams that carry ℓ units of OAM are characterized by an azimuthally dependent phase defined by an $\exp(i\ell\varphi)$ term in their formulation, where φ is the transverse azimuthal coordinate [2]. Consequently, their wavefronts consist of ℓ intertwined helices. Among the distinguishing features of OAM-carrying beams is the fact that they are orthogonal to one another and are thus of significant interest in optical communications, where information is encoded into a single photon's OAM [3–6], sometimes in conjunction with another optical degree of freedom like polarization [7, 8]. In practice, these methods aim to increase the rate at which information can be transferred and have thus motivated the development of several schemes that can readily acquire an optical beam's OAM content. Much like how polarizing beam splitters can split a beam's orthogonally polarized components, some of these schemes include devices that spatially separate a beam based on its OAM composition [9]. These so-called OAM *sorters* have been granted a significant amount of attention as indicated by works that have improved their efficiencies [10, 11] and their scalability [12] along with those that have extended their applications to fields ranging from quantum communications [13] to electron microscopy [14, 15]. OAM sorters primarily rely on the use of two confocal phase elements that are often implemented by means of spatial light modulators (SLM) [9]. The phase added by the latter is essentially based on a transverse modulation of the optical path length experienced by the beam's cross-section. Other types of phase modulating mechanisms could also be employed for this purpose such as those that impart a geometric phase [16, 17] to a beam. Such phases are added by means of Pancharatnam-Berry optical phase elements (PBOE), which are able to add tailored yet opposite phases to a beam's circularly polarized components accompanied by a flip in their handedness [18, 19]. This process inevitably introduces a relation between a beam's spatial profile and its polarization, and hence constitutes a form of spin-to-orbit coupling [20], which has been heavily investigated in the framework of quantum information [21–23].

Recently, a theoretical proposal introduced a PBOE-based OAM sorter that exploits this relation with the beam's polarization as a means of additionally sorting optical SAM states [24]. Here, we report the implementation of such a generalized optical angular momentum sorter where we employ custom-made liquid crystal devices [25] as the required PBOEs. This PBOE sorting scheme experiences less losses and is more compact than those based on SLMs while also being able to modulate an optical beam's transverse phase profile based on its polarization. We characterize our sorter by feeding it with beams carrying well-defined values of OAM and circular polarizations. Afterwards, we verify that the sorter functions for beams consisting of superpositions of such states, and we evaluate the device's crosstalk. Finally, we test the device's performance in the single-photon regime and use it in an OAM-based quantum key distribution (QKD) protocol.

2. Theory

An OAM sorter's performance primarily relies on the unwrapping of a beam's azimuthal phase variations into variations along a Cartesian coordinate [9]. In the case of an OAM-carrying beam, its unwrapped form will consist of tilted wavefronts whose tilt is proportional to the beam's original OAM value. When made to propagate through a lens, these tilted waves will focus at different positions, thus enabling the spatial separation of a beam based on its original OAM content. In practice, the unwrapping crucial to this process is achieved by means of a conformal mapping between Cartesian (x, y) and scaled log-polar ($u = -a \ln(\sqrt{x^2 + y^2})$, $v = a \arctan(y/x)$) coordinates, where a and b are scaling parameters. This transformation can be realized by using the following confocal phase elements [26]:

$$\text{Unwrapper}: \ \phi_1(x, y) = \frac{2\pi a}{\lambda f}\left[y \arctan\left(\frac{y}{x}\right) - x \ln\left(\frac{\sqrt{x^2 + y^2}}{b}\right) + x\right] \tag{1}$$

$$\text{Corrector}: \ \phi_2(u, v) = -\frac{2\pi ab}{\lambda f} \exp\left(-\frac{u}{a}\right) \cos\left(\frac{v}{a}\right), \tag{2}$$

where λ is the wavelength of the beam and f is the focal length of the lens used to perform the mapping. Specifically, the ϕ_1 element performs the required unwrapping while the ϕ_2 element provides the final phase corrections to the beam in order to complete the mapping. These elements will hereafter be referred to as the *unwrapper* and the *corrector* elements, respectively.

Using PBOEs as the sorter's phase elements introduces a polarization-dependent transformation onto the beam [27]. This polarization dependence is attributed to the fact that PBOEs are birefringent devices characterized by a spatially varying optical axis. When these are tuned to half-wave optical retardation, the handedness of the SAM components is flipped and the beam gains a Pancharatnam-Berry (geometric) phase due to the distribution of the device's optical axis [18]. More specifically, a PBOE defined by an optical axis distribution of $\alpha(x_1, x_2)$, where x_1 and x_2 are transverse coordinates, will add a phase of $\pm 2\alpha(x_1, x_2)$ on left-right–handed circularly polarized light, respectively, accompanied by a flip in the handedness of these circular polarizations.

In cases where this polarization inversion occurs, a beam going through a PBOE defined by an optical axis of $\alpha = \phi_1/2$ will cause any right-handed circularly polarized light to undergo a reversed unwrapping process with respect to the conventional one experienced by left-handed circularly polarized light, thus enabling a spatial separation between both of the unwrapped circularly polarized components. Given that the beam's original right-handed circular polarization now unwraps at the horizontal position $u_R = -u_L$, where u_L is the conventional unwrapped position taken by the left-handed circular polarization, the sorter's second element must be modified accordingly to provide the required phase corrections to both of the beam's polarization components [24]. Therefore, to provide a proper phase correction to the unwrapped beam [26], u is replaced by $-|u|$ in Eq. (2) and is multiplied by a factor of -1 to account for polarization-dependent effects, i.e.

$$\tilde{\phi}_2(u, v) = \frac{2\pi ab}{\lambda f} \exp\left(\frac{|u|}{a}\right) \cos\left(\frac{v}{a}\right) - \frac{\pi}{\Lambda} u, \tag{3}$$

where the additional grating term $(\pi/\Lambda)u$ is added to provide further separation between both polarizations upon propagation through the sorter's second lens [24]. The separation of these two orthogonally polarized components enabled by the first PBOE thereby allows for a device capable of sorting optical angular momentum eigenstates and, in turn, of handling an increased amount of information channels that can be used in practical applications.

3. Fabrication

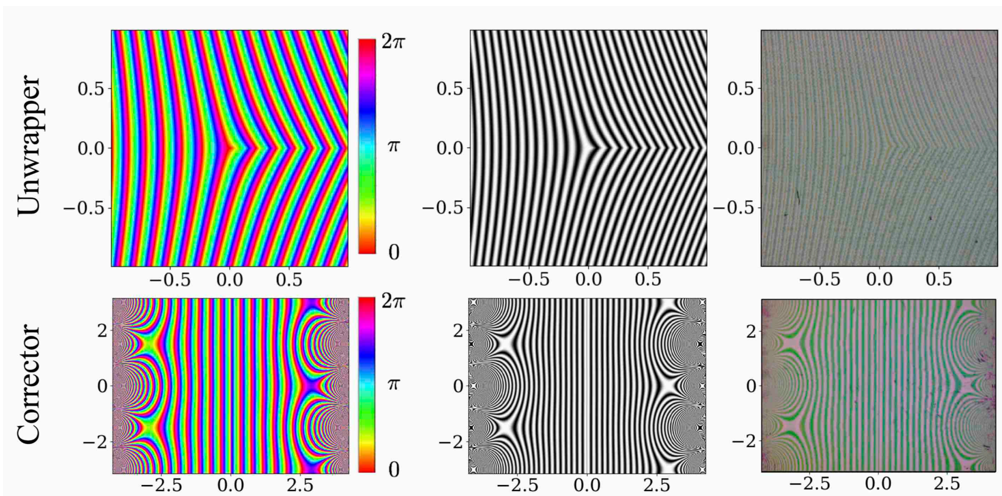

Fig. 1. The geometric phase 2α (left) attributed to the unwrapper (top) and corrector (bottom) elements; (center) the devices' expected transmission when placed between two polarizers; (right) the devices' observed transmission patterns. The axes' units are in mm.

Our sorter's implementation relies on the use of custom-made liquid crystal devices as the required PBOEs [25]. These devices consist of a layer of patterned 6CHBT nematic liquid crystals confined within two indium tin oxide (ITO)-coated substrates separated by spacer-grade silica microspheres. The substrates are additionally spin-coated with a layer of azobenzene-based dye molecules [28, 29]. We specifically use microspheres with a diameter below 4.8 µm and the azobenzene-based aligning material PAAD-22 provided by BEAM Co. The orientation of the liquid crystals is determined by that of the dye molecules which are aligned by means of a photo-alignment method used to reconstruct the device's desired optical axis distribution [25,30–32]. To fabricate the PBOEs required to perform the sorting process, we adapted such a photo-alignment method to produce liquid crystal devices with an optical axis distribution defined by $\alpha_1 = \phi_1/2$ and $\alpha_2 = \tilde{\phi}_2/2$. The sorting parameters that appear in ϕ_1 and $\tilde{\phi}_2$ were chosen to optimize the sorter's performance without significantly compromising the quality of the fabricated elements. That being said, we used parameters of $a = 3/(2\pi)$ mm, $b = 2$ µm, $\lambda = 810$ nm, $f = 500$ mm, and $\Lambda = 200$ µm. These parameters can also be optimized for other wavelengths including those that are commonly used in telecommunications. The corresponding geometric phase 2α attributed to the element along with the device's expected and observed appearance between two crossed polarizers are shown in Fig. 1. The close resemblance of these patterns suggests that the unwrapper and corrector have been fabricated with reasonable fidelity to the design.

Our devices have an efficiency of 72%. Most losses however occur due to reflections from their cells' glass substrates. These losses can be eliminated by means of an anti-reflection coating to increase their efficiency to a value closer to their conversion efficiency, which can realistically reach values of 97% [25]. To ensure that our devices operate at the half-wave condition required to perform the sorting process, we also soldered wires on the conductive side of their ITO substrates. This addition allows us to apply a tuning voltage to the device which modifies the birefringence of our device's liquid crystals. Minor errors in the fabrication process introduced some aberrations in the devices as later shown in experimental results. We attribute the latter to a minor scaling error in our photo-alignment. This displaces the region where the unwrapped beam hits the corrector element, thus preventing the completion of the conformal mapping required to perform the sorting process. To overcome this issue, we shifted our beam's wavelength until its unwrapped components interacted with the regions of the corrector that enabled an optimal phase correction while simultaneously tuning our device's half-wave retardation to the examined wavelength. We found that this optimal wavelength was 850 nm and thereby employed this value in our experiments.

4. Results

We characterized our device using the experimental setup shown in Fig. 2, which allows us to provide several types of optical beams to the sorter. We first examined the sorter's output when

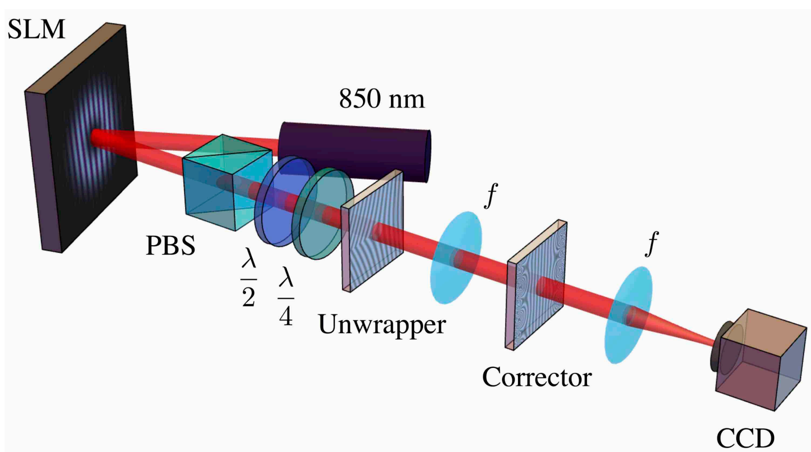

Fig. 2. Experimental setup used to characterize the sorter. A spatial light modulator (SLM) is used to provide a distinct phase and intensity profile to a beam coming from a 850 nm diode laser while a set of elements composed of a polarizing beamsplitter (PBS), a half-wave plate ($\lambda/2$), and a quarter-wave plate ($\lambda/4$) is used to provide the beam with a specific polarization. The beam then goes through the sorter which consists of the unwrapper PBOE, a lens, the corrector PBOE, and another lens. The sorter's output is then examined with a CCD camera.

fed with circularly polarized beams carrying well-defined OAM values and compared it with simulated outputs obtained using the split-step beam propagation method [33]. Such beams will hereafter be referred to as optical angular momentum eigenstates. The intensity profile of the sorted beams are shown in Fig. 3(a). We can observe that the sorted orders attributed to left- and right-handed circularly polarized light are clearly distinguishable from one another while simultaneously exhibiting good separation between the conventional OAM orders attributed to the confocal phase elements. Moreover, we also note that the transverse positions of the right-handed circular OAM orders are inverted with respect to those of the left-handed circular ones, thus verifying that these two polarizations do indeed acquire opposite phases as they propagate through the sorter. Minor effects attributed to the device's aberrations are also noticeable most notably by the lower definition of the experimental sorted orders when compared with the simulated output of an ideal sorter shown in Fig. 3(b). This lower definition is also observed in Fig. 3(c) where we show the simulated profile of a beam going through an aberrated sorter. The latter namely consists of elements with phase patterns compressed by a factor of 4% which accounts for the scaling errors in the device's fabrication. Nevertheless, the lower order modes depicted in Fig. 3(a) are sufficiently distinct for practical applications as further demonstrated.

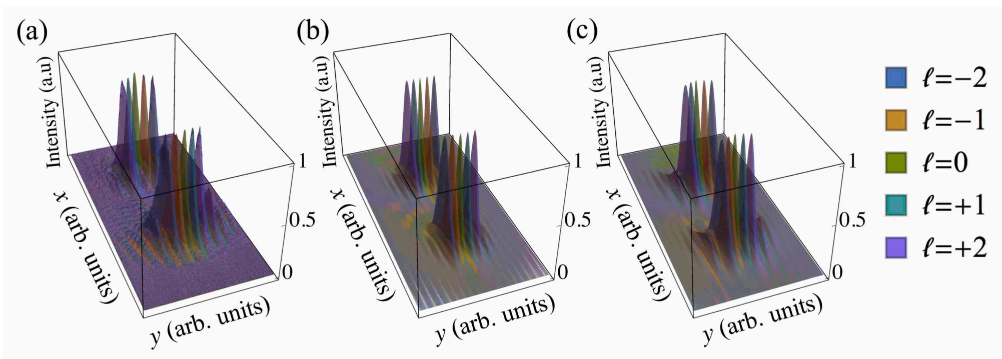

Fig. 3. Relative intensity profiles of the sorter's output when fed with circularly polarized beams defined by OAM values ranging from $\ell = -2$ to $\ell = 2$. (a) Measured output of the fabricated sorter. (b) Simulated output of a perfect sorter. (c) Simulated output of an aberrated sorter. Left-handed circular polarizations appear at the bottom of the plots while right-handed circular polarizations appear at the top.

Following this first calibration process, we tested our sorter's performance for beams consisting of a superposition of angular momentum eigenstates. Such a superposition can consist of a circularly polarized beam in a superposition of OAM states, an OAM state in a superposition of polarization states (i.e. a non-circularly polarized beam) or a combination of the two. We demonstrate these three cases in Fig. 4, where we can observe the sorter's performance for all types of superpositions. Once again, we show our experimental results, the simulated output of the ideal sorter, and the simulated output of the aberrated sorter in Fig. 4(a)-(c), respectively. The device's limitations at higher absolute OAM values is clearly observed in the far-right column of Fig. 4, where we provide the sorted orders for the case of linearly polarized light in a superposition of $\ell = +2$ and $\ell = -2$ states. The line appearing between the two orders of the far-right column of Fig. 4(a),(c) clearly indicates the less-defined nature of higher order modes which start to spread out over transverse positions attributed to other modes, e.g. the $\ell = 0$ mode in this case.

In order to further examine the effects related to the overlap of the sorted orders, we evaluated the crosstalk between the modes shown in Fig. 3. To do so, we assigned an elliptically shaped channel to each mode based on the data shown in Fig. 3 and computed the relative intensity of each mode in these channels. These relative intensities can be found in Fig. 5. Our experimental results shown in Fig. 5(a) indicate that 72% of the intensity of a given angular momentum state is found in its respective channel which is comparable to the simulated value of 75% for an aberrated sorter based on the data shown in Fig. 5(c). Both of these quantities are lower than the optimal values of 89% attributed to a perfect sorter whose results are displayed in Fig. 5(b). When adapted to the sorting parameters of previously implemented sorters, this optimal value

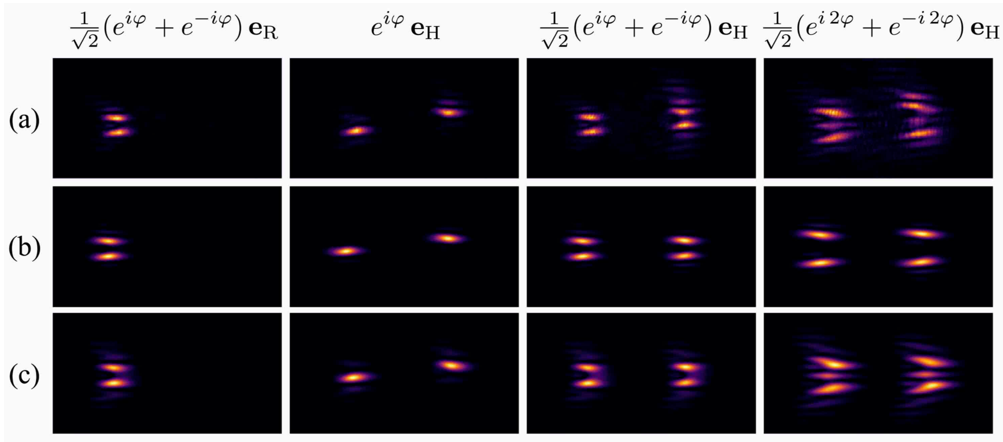

Fig. 4. Relative intensity profiles of the sorter's output when fed with a selection of superpositions of beams consisting of different circular polarizations and OAM values ranging from $\ell = -2$ to $\ell = 2$ for (a) experimental results, (b) simulated results attributed to a perfect sorter, and (c) simulated results attributed to an aberrated sorter. Here $\mathbf{e}_\mathrm{L}$ and $\mathbf{e}_\mathrm{R}$ correspond to the left- and right-handed circular polarization vectors, respectively, and $\mathbf{e}_\mathrm{H} = (\mathbf{e}_\mathrm{L} + \mathbf{e}_\mathrm{R})/\sqrt{2}$ is the horizontal polarization vector.

agrees with those obtained from simulations in earlier works [9]. Though the fact that we are using different sorting parameters prevents us from directly comparing our device's experimental crosstalk with those of other OAM sorters, we do observe that the latter have a similar difference between numerical and experimental crosstalk values [9]. This similarity thereby establishes that our sorter's performance is experimentally comparable to that of its OAM counterpart. For practical purposes however, this percentage can be slightly raised, at the expense of decreasing the device's efficiency, by reducing the size of the channels attributed to each OAM value.

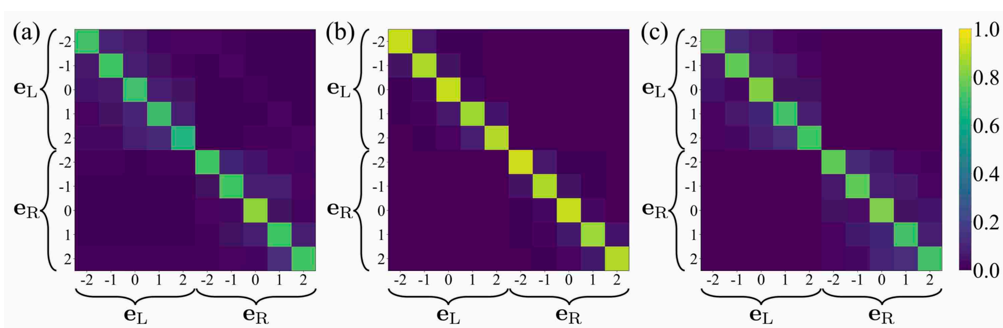

Fig. 5. Relative intensities of angular momentum states found in each angular momentum channel for (a) experimental results, (b) simulated optimal results, and (c) simulated results for an aberrated sorter. We considered states defined by left- and right-handed circular polarizations and by OAM states ranging from $\ell = -2$ to $\ell = 2$.

As mentioned earlier, one of the most attractive features of optical angular momentum states is their natural extension to the quantum nature of light which makes them of interest in quantum communications. Given that our device preserves coherence [21], we examined its performance in the single photon regime for photons in optical angular momentum eigenstates $|\pi, \ell\rangle$ where π and ℓ are states defining the photon's polarization and OAM, respectively. This was achieved by using a pair of down-converted photons generated through spontaneous parametric down-conversion by pumping a ppKTP crystal with 405 nm UV light. The first of the two was sent through the sorter and later detected by an ICCD camera which was triggered by the second photon. The resulting images are shown in Fig. 6 along with their classical counterparts. We can observe a good agreement between the images taken in the classical and quantum regimes, thus verifying our device's performance at the single photon level.

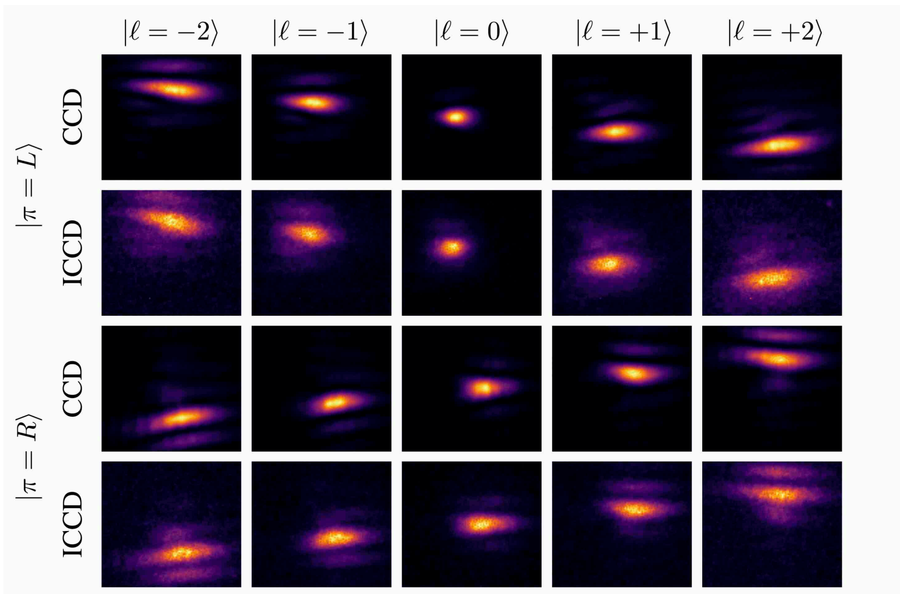

Fig. 6. The sorter's output when fed with single photons in angular momentum eigenstates. The images were taken using a triggered ICCD camera. The images are grouped with their classical counterparts which correspond to ones taken with a regular CCD camera with coherent light going through the sorter.

Now that we have established that our sorter exhibits a satisfactory level of crosstalk along with a good performance with single photons, we proceed by demonstrating how our device can be employed in a practical application. More specifically, we test our sorter for high-dimensional quantum cryptography given the extensive body of works exploring the use of OAM sorters in this field [11, 13]. In particular, we perform a high-dimensional extension of the seminal quantum key distribution BB84 protocol [34], the former of which has been recognized to securely transmit an increased amount of information. In the first place, for the case of an error-free quantum channel, Alice, the sender, may send a total of $\log_2(d)$ bits of information per photon, where d is the dimensionality of the protocol, to Bob, the receiver, hence increasing the overall secure key rate. Moreover, it is well-known that QKD protocols may be performed only up to a certain error threshold. In the case of the standard 2-dimensional BB84, this error threshold is given by 11.0%, where no secret shared key may be established beyond this level of error. However, by increasing the dimensionality of the BB84 protocol, this error threshold may be increased, e.g. in the case of $d = 10$ the error threshold is given by 26.2% [35]. Therefore, higher-dimensional QKD extensions are much more robust to noise and device imperfections. Most of the works on high-dimensional QKD revolve around an OAM based QKD protocol where the employed mutually unbiased bases consist of quantum states that can be spatially separated using a sorter. This sorter, however, is differently configured to perform measurements in each of these bases. That being said, the first basis used in this scheme usually consists of the OAM basis whose states can be readily measured using the conventional sorter configuration depicted in Fig. 2. The states $|\ell\rangle$ of this basis usually range from OAM values of $\ell = -N$ to $\ell = N$, and hence the dimensionality of $d = 2N + 1$. The second basis corresponds to the so-called angular basis whose states can be expressed in terms of the OAM basis as $|n\rangle_{\text{ang}} = d^{-1/2} \sum_{\ell=-N}^{N} \exp\left(i\, 2\pi n\ell/d\right) |\ell\rangle$ [11, 13], where n is an integer between $-N$ and N. In addition to being mutually unbiased with respect to OAM modes, angular modes are defined by distinct angular shaped intensity profiles that nearly do not overlap with one another. Therefore, because they are already spatially separated, they consist of the perfect complementary basis for performing QKD with OAM-carrying beams. Though a measurement in the angular basis could in principle be performed on the beam without manipulating it, such a measurement is often configured by using the unfocused output of the sorter which essentially consists of the unwrapped beam where the angular modes occupy distinct transverse positions as opposed to angular ones. Such a configuration is usually employed in order to enable the use of secondary methods aiming to reduce the crosstalk between these unwrapped modes. With these factors in consideration, a BB84 QKD protocol relying on these two mutually unbiased bases consists of Alice randomly generating states belonging to these two bases and sending them to Bob that randomly performs a measurement in either of these bases using his two different sorter configurations. Using our sorter, we expand on this scheme

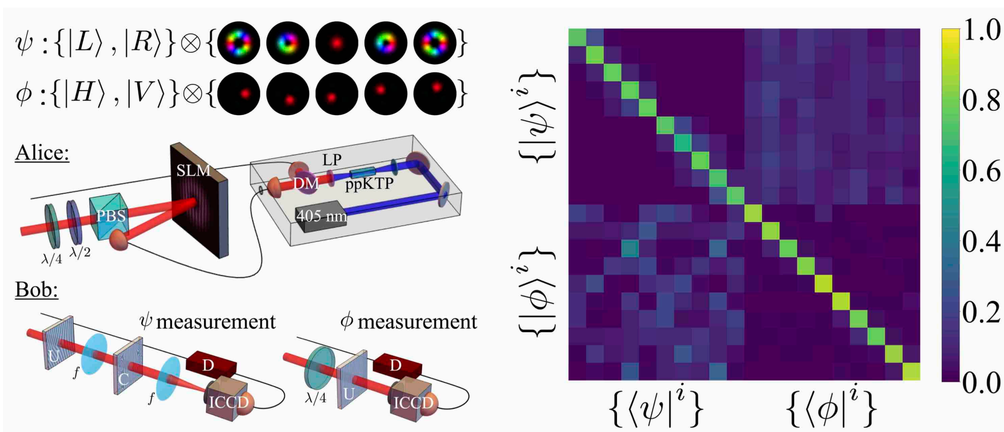

Fig. 7. Summary of the QKD demonstration conducted with our generalized angular momentum sorter. Top left: Mutually unbiased bases ψ and ϕ used in this demonstration where states attributed to spatial modes are depicted as their transverse phase profile in hue colours masked by their intensity profile. Bottom left: setups used by Alice and Bob in this QKD scheme. Alice's state preparation setup randomly generates a state either in the ψ or ϕ basis using an SLM, a quarter-wave plate ($\lambda/4$), a half-wave plate ($\lambda/2$), and a PBS. The single photons that she uses come from a down converted 405 nm source consisting of a pair of 850 nm and 775 nm photons. The latter are separated using a dichroic mirror (DM) thus enabling the use of the 850 nm photon as the *signal* photon and the 775 nm one as the *idler* photon. Bob then randomly performs a measurement in either the ψ or ϕ basis using two different sorter configurations and an ICCD camera that is triggered by the *idler* photon using a detector (D). Right: Probability-of-detection matrix of our QKD scheme. Figure legend: ppKTP = periodically-poled KTP crystal, LP=long-pass filter, U=unwrapper, C=corrector.

by using a single photon's polarization to increase the size of these mutually unbiased bases by a factor of two. Namely, the OAM basis $\{|-N\rangle, \ldots, |N\rangle\}$ is now extended to the generalized optical angular momentum basis $\psi = \{|L\rangle, |R\rangle\} \otimes \{|-N\rangle, \ldots, |N\rangle\}$, where $|L\rangle$ and $|R\rangle$ respectively corresponds to left- and right-handed circularly polarized states, and now consists of the optical angular momentum eigenstates that have been discussed in this work. As in the case of our classical measurements, single photon measurements in the optical angular momentum basis can be carried out using the sorter configuration depicted in Fig. 2. As for the complementary basis, we chose $\phi = \{|H\rangle, |V\rangle\} \otimes \{|-N\rangle_{\text{ang}}, \ldots, |N\rangle_{\text{ang}}\}$, which corresponds to the product of the angular basis $\{|-N\rangle_{\text{ang}}, \ldots, |N\rangle_{\text{ang}}\}$ with the polarization basis consisting of horizontally $|H\rangle$ and vertically $|V\rangle$ polarized states, both of which are unbiased with respect to their angular momentum counterparts. To perform a measurement in this basis, we first make our single photons go through a quarter-wave plate in order to map horizontally and vertically polarized states to left- and right-handed polarized ones. After this, the photons go through a region of the unwrapper element that is far from its centre and that closely resembles a grating. This process enables the separation of angular modes in the $\{|H\rangle, |V\rangle\}$ basis, and thus a measurement in the complementary ϕ basis given that angular modes inherently exhibit good spatial separation. A summary of this scheme along with experimental results are shown in Fig. 7, where we conducted such a protocol defined by a $N = 2$ parameter, thus enabling 10-dimensional quantum key distribution. In a d-dimensional BB84 protocol, the secret key rate is given by $R = \log_2(d) - 2h^{(d)}(e_b)$, where $h^{(d)}(x) := -x\log_2(x/(d-1)) - (1-x)\log_2(1-x)$ is the d-dimensional Shannon entropy. Here, we obtained a quantum bit error rate of $e_b = 21.2\%$, corresponding to a secret key rate of $R = 0.49$ bits/photon. These values are directly limited by our device's crosstalk, which, as we mentioned above, is significantly increased by its aberrations. Nonetheless, because our sorter allows for polarization sorting, it allows for the execution of a QKD protocol in a dimension twice as great as that of a solely OAM based protocol. The ability to increase this dimension lowers the threshold on the quantum bit error rate needed to securely perform QKD, thus enabling the use of lower-quality sorters for this purpose. Improving the quality of this angular momentum sorter to that of its current OAM counterparts would also considerably enhance the performance of this QKD protocol to a level above those that solely rely on OAM. Namely, a device with a lower crosstalk would increase the quantum bit error rate which, in conjunction with a higher dimension, would also increase the protocol's secret key rate.

5. Conclusion

In conclusion, we fabricated the first device able to sort both orbital and spin optical angular momentum eigenstates using liquid crystal based PBOEs. The device's performance was first tested by feeding it with various circularly polarized beams with well-defined OAM values. We then verified that it could process beams in superpositions of optical angular momentum eigenstates into their respective sorted orders. We later calculated the crosstalk of our sorter's output and found that about 72% of a mode was confined within its assigned channel. Finally, we verified that our device could operate with single photons and exploited this feature to use it in a 10-dimensional BB84 QKD scheme. The performance of the latter, along with that of several other sorter-based applications, could be further improved by reducing the device's crosstalk. To achieve such a purpose, aberrations in the device must first be removed by improving its fabrication process. For instance, improvements could be made on the uniformity of the layers of materials coated on the device's glass substrate and on the uniformity of the cavity enclosing the liquid crystals. Likewise, more refined photo-alignment methods could also be beneficial [36]. Though this would significantly improve the sorter's quality, additional methods could also be employed to further reduce the device's crosstalk such as those that rely on the use of fan-out elements [10, 11, 37, 38]. These can be added after the sorter's output or even be integrated within the PBOEs themselves. In comparison to other current OAM sorting devices, our system has both drawbacks and advantages. For example, the polarization-dependent nature of our phase elements prevents us from directly scaling down our scheme significantly. By comparison, a device akin to that presented in [12] with the addition of a polarization-dependent beam displacer would consist of a compactly configured three-element device that imparts less aberrations on the sorted beam.

The system presented here is a clear demonstration of simultaneous OAM and polarization sorting. Using state-of-the-art methods to produce high-quality liquid crystal elements [29,39–42] would increase the performance of our sorter to be on par with existing designs. With the elimination of these technical limitations, our sorter benefits from several advantages. For instance, given that our PBOEs have a tunable half-wave condition and that our sorter's lenses are not integrated directly in the unwrapper and corrector elements, our sorting scheme can easily be adapted to other wavelengths. As implied by Eqs. (1, 2) this adaptation is feasible provided that λf maintains the same value as that of the sorter's original configuration. Moreover, both of our sorter's optical components, namely PBOEs and lenses, can be scaled down to ultra thin elements [43,44]. Finally, the fact that our sorter relies on geometric phases makes it advantageous in applications that rely on similar processes. In particular, communications schemes employing vector vortex beams [45,46] would benefit from our sorter given that these beams consist of a superposition of two components opposite in both OAM and circular polarization. Our device's antisymmetric sorting process would enable the sorting of vector vortex beams along adjacent positions and thereby simplify the analysis of the beam's vector vortex content. Such extensions to our methods would significantly improve the sorter's channel capacity and thereby its performance in applications such as classical super-dense coding and quantum communications.

Funding

Canada Research Chairs; Canada Excellence Research Chairs (CERC); Government of Canada; Natural Sciences and Engineering Research Council of Canada (NSERC).

nature COMMUNICATIONS

ARTICLE

Received 5 Nov 2016 | Accepted 6 Apr 2017 | Published 24 May 2017 DOI: 10.1038/ncomms15536 OPEN

Measuring the orbital angular momentum spectrum of an electron beam

Vincenzo Grillo[1,2], Amir H. Tavabi[3], Federico Venturi[1,4], Hugo Larocque[5], Roberto Balboni[6], Gian Carlo Gazzadi[1], Stefano Frabboni[1,4], Peng-Han Lu[3], Erfan Mafakheri[4], Frédéric Bouchard[5], Rafal E. Dunin-Borkowski[3], Robert W. Boyd[5,7], Martin P.J. Lavery[8], Miles J. Padgett[8] & Ebrahim Karimi[5,9]

Electron waves that carry orbital angular momentum (OAM) are characterized by a quantized and unbounded magnetic dipole moment parallel to their propagation direction. When interacting with magnetic materials, the wavefunctions of such electrons are inherently modified. Such variations therefore motivate the need to analyse electron wavefunctions, especially their wavefronts, to obtain information regarding the material's structure. Here, we propose, design and demonstrate the performance of a device based on nanoscale holograms for measuring an electron's OAM components by spatially separating them. We sort pure and superposed OAM states of electrons with OAM values of between −10 and 10. We employ the device to analyse the OAM spectrum of electrons that have been affected by a micron-scale magnetic dipole, thus establishing that our sorter can be an instrument for nanoscale magnetic spectroscopy.

[1] CNR-Istituto Nanoscienze, Centro S3, Via G Campi 213/a, I-41125 Modena, Italy. [2] CNR-IMEM Parco Area delle Scienze 37/A, I-43124 Parma, Italy. [3] Ernst Ruska-Centre for Microscopy and Spectroscopy with Electrons, Forschungszentrum Jülich, 52425 Jülich, Germany. [4] Dipartimento FIM Universitá di Modenae Reggio Emilia, Via G Campi 213/a, I-41125 Modena, Italy. [5] Department of Physics, University of Ottawa, 25 Templeton Street, Ottawa, Ontario, Canada K1N 6N5. [6] CNR-IMM Bologna, Via P. Gobetti 101, 40129 Bologna, Italy. [7] Institute of Optics, University of Rochester, Rochester, New York 14627, USA. [8] School of Physics and Astronomy, Glasgow University, Glasgow, G12 8QQ Scotland, UK. [9] Department of Physics, Institute for Advanced Studies in Basic Sciences, 45137-66731 Zanjan, Iran. Correspondence and requests for materials should be addressed to V.G. (email: vincenzo.grillo@unimore.it) or to E.K. (email: ekarimi@uottawa.ca).

Quantum complementarity states that particles, for example, electrons, can exhibit wave-like properties such as diffraction and interference upon propagation. Electron waves defined by a helical wavefront are referred to as twisted electrons and are imbued with several additional mechanical and magnetic properties[1]. For instance, upon elastic interaction, these magnetic properties, in conjunction with the opposite handedness of twisted electrons, allow for probing magnetic chirality as well as magnetic dichroism[2,3]. Furthermore, the added unbounded twisted motion of these charged particles is pertinent to the investigation of the nature of radiation[4], virtual forces and increasing the lifetime of unstable and metastable particles[5]. From a more fundamental viewpoint, structured electrons also provide novel insights into the quantum nature of electromagnetic–matter interaction, for example, the realization of Landau–Zeeman states[6,7] and spin-to-orbit coupling[8]. Orbital angular momentum (OAM)-carrying electron waves can be generated through a variety of methods by directly interacting with the electrons' wavefronts[9]. These processes rely on devices such as spiral phase plates[10], amplitude and phase holograms[11–14], cylindrical lens[15] mode converters or even electron microscope corrector lenses[16]. Spin-to-orbit coupling has also been theoretically proposed as a method to add OAM to electrons[17]. Other methods to do so exploit the magnetic properties of electrons, most notably by employing a magnetic needle simulating a magnetic monopole[18].

Reciprocally, devices that are used to generate twisted electrons can also be adapted to measure an electron's OAM content[19]. The most commonly employed of these devices relies on a series of projective phase flattening measurements, allowing one to obtain the magnitude of each OAM component of a beam's spectrum[20]. To perform such an analysis, an OAM component's wavefront is flattened, thus causing it to gain a Gaussian-like profile upon propagation[21]. This profile allows it to be easily selected from the remaining parts of the beam and therefore to evaluate the intensity of this component. To obtain these relative intensities, each component needs to be coupled to the device's electron detection mechanism. However, this coupling process is biased towards electrons carrying lower absolute values of OAM, thus introducing discrepancies in the measured spectrum[22]. Moreover, much like how different types of OAM-carrying beams are generated using different devices, different devices are required to flatten the wavefronts of the beam's various OAM components. Therefore, though such an analysis of a beam's OAM content is efficient, it also requires a substantial number of elements to perform repetitive measurements. There are also other OAM measurement methods relying on interferometry[23,24], though they possess serious limitations such as a limited amount of information that can be extracted from the obtained interference patterns or also by the need for an extremely stable interferometer. Interferometry is also of limited usefulness when analysing the OAM content of inelastically scattered electrons due to their short coherence lengths.

A viable alternative to these methods is available in optics and relies on transforming an OAM-carrying photon's azimuthal phase variations into transverse phase gradients that can be spatially resolved and separated with a lensing element[25,26]. The device thus effectively behaves as an OAM spectrometer, which could be of significant interest in electron optics and materials science as it would provide detailed information on a material's magnetic spectrum.

The operation of our presented electron OAM spectrometer relies on a similar OAM separation process. Much like its optical counterpart, it is essentially based on unwrapping the azimuthal phase variations associated with an electron's OAM into variations over a Cartesian coordinate of the plane transverse to the electron's propagation. This effectively causes the electron's original helical wavefronts to become planar and inclined with respect to the beam's original direction of propagation. Namely, the degree to which these wavefronts are tilted will increase with the azimuthal variation of the electron's original phase profile, that is, its OAM. As a result, focusing these unwrapped waves with a lensing element will cause electrons originally carrying different OAM values to focus at correspondingly separate lateral positions. By using this method, we are thus able to decompose an electron beam's OAM content by measuring the relative electron intensity at each of these possible focusing positions.

Results

Theory. The unwrapping process, as detailed in ref. 25, requires the beam's transverse profile in polar coordinates (r, φ) to be physically mapped to Cartesian coordinates. Such a transformation can be achieved by means of a conformal mapping between the Cartesian coordinates of the initial beam's profile (x, y) and those of its final profile (u, v). The coordinates (u, v) are log-polar coordinates and can be related to the Cartesian coordinates (x, y) via the transformations $x = \exp(u)\cos(v)$ and $y = \exp(u)\sin(v)$ or equivalently by $u = \ln\left(\sqrt{x^2+y^2}\right)$ and $v = \arctan(y/x)$[27]. A Cartesian coordinate $x + iy$ in the complex plane can be mapped onto its corresponding log-polar coordinate $u + iv$ with the conformal mapping $f(z) = \ln(z)$. Using a scalable version of this mapping, $\Phi(z) = a \ln(z/b)$, an OAM-carrying beam's transverse wavefunction $\psi_\ell(r,\varphi) = f(r)\exp(i\ell\varphi)$ can be mapped to the following wavefunction

$$\begin{aligned}\Phi(f(r)\exp(i\ell\varphi)) &= U + iV \\ &= a\ln(f(r)/b) + ia\ell\varphi.\end{aligned} \tag{1}$$

Such mappings are commonly conducted using a set of confocal phase elements performing a log-polar coordinate transformation[27].

Implementation. We adopt a similar diffractive approach to develop our sorter using two electron phase holograms, as displayed in Fig. 1, and where the lensing effects required to perform the mode transformation are configured using our electron microscope's lenses (see Supplementary Note 1 and Supplementary Fig. 1 for more details). The first of the holograms effectively maps the electron's azimuthal phase variations along a Cartesian coordinate, while the second provides phase corrections to defects introduced by the first hologram. Additional information concerning these elements is provided in Supplementary Note 2. We depict this process in Fig. 1 where we show an electron beam's recorded transverse profile as it propagates through the sorter. Here, we use electrons consisting of a superposition of states defined by OAM values of ± 5, that is, $\left(\psi_{+5}(r,\varphi) + \psi_{-5}(r,\varphi)\right)/\sqrt{2}$ (ref. 28). Such a beam consists of a series of 10 lobes that are equidistantly arranged along a ring-shaped outline in the beam's transverse plane. The presence of these lobes is a direct result of the beam consisting of a superposition of two OAM components defined by the same magnitude, yet by opposite signs. More specifically, as they arise from the beam's OAM content, these lobes are additionally related to its constituent $\ell = \pm 5$ electrons' transverse azimuthal phase profiles. The beam was generated using the phase mask whose transmission electron microscopy image along with an image of the beam transmitted through such a hologram can be found in the generator plane of the sorter found in Fig. 1. After passing through the sorter's first hologram, these lobes rearrange themselves into a line since the beam's azimuthal phase variations have been unwounded along one of the Cartesian coordinates of

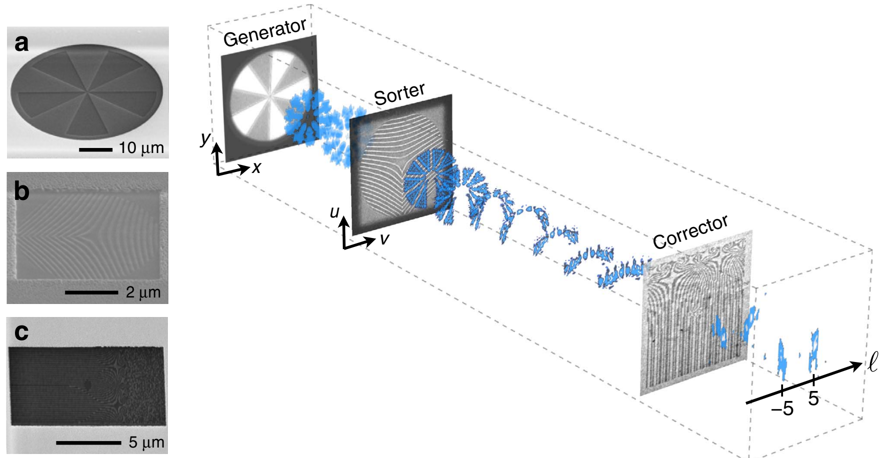

Figure 1 | Schematics of the electron sorter. These schematics also show an electron beam's experimental transverse intensity profile recorded at various planes in the sorting apparatus. A hologram in the sorter's generator plane that corresponds to the electron microscope's condensor, produces an electron beam carrying orbital angular momentum (OAM). In this particular case, the beam consists of a superposition of ± 5 OAM states. The beam then goes through a hologram in the apparatus' sorter plane, positioned at the microscope's sample holder, that performs the required conformal mapping $(x, y) \mapsto (u, v)$. Once the beam is unwrapped, it passes through a hologram in the sorter's corrector plane corresponding to the microscope's selected area diffraction (SAD) aperture. This hologram brings corrections to any phase defects to the beam to stabilize its propagation through the rest of the sorter. At the sorter's output, the original beam's OAM content is spatially resolved on a screen and captured by a CCD camera. A more detailed schematic of our sorter's implementation is included in Supplementary Fig. 1 and Supplementary Note 1 where we provide details concerning the electron microscope lenses required to perform the mapping. Scanning electron microscopy (SEM) images of the depicted holograms, the ones in the generator, sorter and corrector planes, are shown in **a**–**c**, respectively.

its transverse plane. The beam propagates through the second hologram, shown in the corrector plane of Fig. 1, to stabilize its propagation. The beam then propagates through a lens and is focused onto a screen. This allows for the initial beam's OAM content to be readily analysed as depicted in the final plane of Fig. 1.

A more thorough calibration of the sorting apparatus was then performed by repeating the above process for wavefunctions carrying various values of OAM generated with various devices that are further discussed in Supplementary Note 3. The spectra resulting from this calibration have been background subtracted and deconvoluted using conventional spectroscopy methods (see Supplementary Note 4 and Supplementary Fig. 2). These results are displayed in Fig. 2 for the case of wavefunctions defined by single and superposed OAM states ranging from -10 to 10. Based on the various parameters defining the phase profile of the holograms used in the sorter, the cross-talk between components of the electrons' OAM spectra is expected to be below 20%. However, due to fabrication and alignment imperfections in our apparatus, including the holograms generating the OAM-carrying electrons, we observe higher values of cross-talk between OAM components. The values of the cross-talk observed in the spectra shown in Fig. 2 were found to be 28% (Fig. 2a), 43% (Fig. 2b), 39% (Fig. 2c) and 18% (Fig. 2d). Such experimental limitations could be overcome by adopting a fan-out configuration as employed in optical sorters[25,26] and by improving the quality of the sorter and the corrector holograms via alternative fabrication methods. Cross-talk can also be further reduced by an improved control over the electron beam's aberrations. Though this may be the case, the sorter's performance is clearly observed through the distinct separation of the OAM states contained in the specific electron beams.

This sorter can be used to analyse magnetic structures affecting the OAM content of an electron beam. Here, we use our sorter to analyse the magnetic properties of a magnetized sample deposited using the method described in ref. 29, a cobalt magnetic dipole in our case. To do so, the dipole has been positioned in the sorting apparatus in a way to replace the holograms that were previously generating the test wavefunctions. This magnetic structure consists of a single magnetic bar. A scanning electron microscopy image of the bar can be found in Fig. 3a. Its magnetic configuration is characterized by a strong elongation enforcing the presence of a strong net magnetic dipole moment even after the magnetizing field is removed. Its remanence field was also characterized using electron holography and Lorentz imaging and is depicted in Fig. 3b.

The potential use of the sorter for this particular measurement arises from the fact that the multiplicative term introduced by a magnetic dipole onto a passing Gaussian electron beam wavefunction can be written as

$$g(r, \varphi) = \exp(i\,\chi(r)\sin\varphi) \tag{2}$$

where $\chi(r) = (e\mu_0\mathcal{M})/(hr)$, h is the Planck constant, μ_0 is the permeability of vacuum and $\mathcal{M}$ is the dipole's magnetic moment (see Supplementary Note 5 for more details). To observe the effect that such a term will have on an electron's OAM content, $g(r, \varphi)$ must be Fourier-expanded in terms of φ, namely $g(r, \varphi) = \sum_{\ell=-\infty}^{\infty} c_\ell(r)\exp(i\ell\varphi)$, where $c_\ell(r)$ are expansion coefficients. However, given that the resulting expansion terms carry a quantized azimuthal phase defined by ℓ, then it follows that these components also carry OAM values of ℓ. By default, the expansion coefficients c_ℓ correspond to the weight of each OAM component of a beam that has been affected by the magnetic dipole. These coefficients can be found using the Jacobi–Anger expression, that is, $\exp(i\,\chi\sin\varphi) = \sum_{\ell=-\infty}^{\infty} J_\ell(\chi)\exp(i\ell\varphi)$, and thus correspond to $J_\ell(\chi(r))$, where J_ℓ is the ℓ^{th} order Bessel function of the first kind. This formulation of the added phase clearly depicts the imparted OAM content of the dipole onto the electron beam's wavefunction and hence the ability to use the sorter to measure this magnetic dipole moment $\mathcal{M}$.

Though a more detailed analysis can be used to predict the OAM spectrum induced by the magnetic dipole, one can instead employ a simplified model to do so based on the apparatus' layout. The use of this model is justified by the truncation of the beam after passing through the first of the sorter's holograms. Such truncations result in lensing effects that will consequently displace

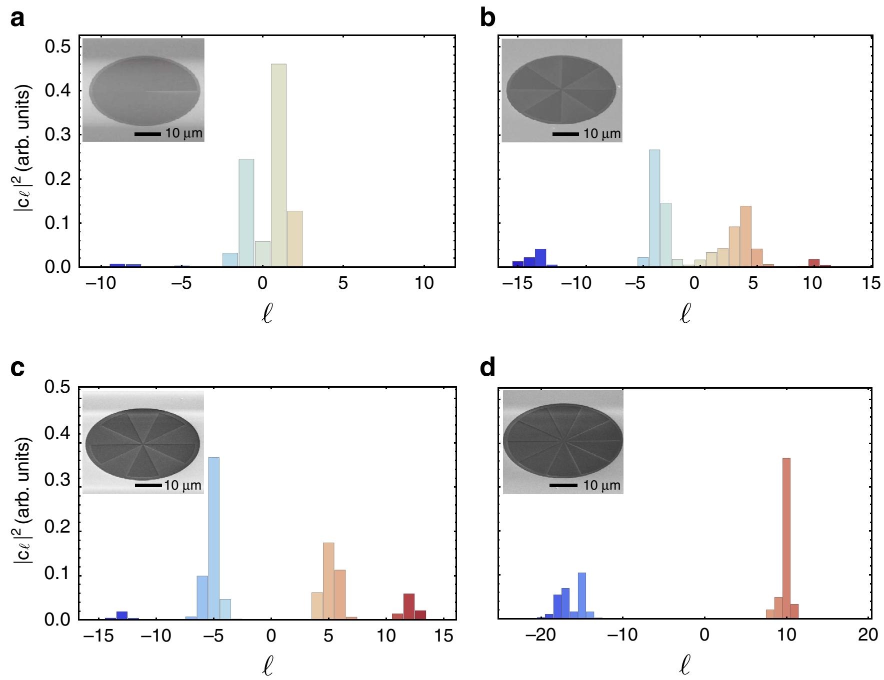

Figure 2 | Experimental OAM spectra of electron beams. Spectrum of a beam consisting of electrons defined by: (**a**) OAM of $+1$, ψ_{+1}, produced with a spiral phase plate; (**b**) a superposition of ± 4 OAM states, $(\psi_{+4}+\psi_{-4})/\sqrt{2}$, generated by a phase mask; (**c**) a superposition of ± 5 OAM states, $(\psi_{+5}+\psi_{-5})/\sqrt{2}$, generated by a phase mask; and (**d**) OAM of $+10$, ψ_{+10}, produced by a spiral phase plate. Scanning electron microscopy (SEM) images of the devices used to generate the analysed electron beams are provided in the insets of their respective spectra.

electrons that were originally positioned at the hologram's cutoff radius $r_{\max}$. As a result, these electrons will occupy a greater area of the beam following the truncation. Their profile will therefore also be spatially extended in the observed OAM spectrum. This will cause the general outline of the sorter's output to be predominantly associated with these electrons. Strictly speaking, the output spectrum of the sorter will be determined by its numerical aperture. Therefore, we may approximate the phase added by the dipole onto the beam as $\chi(r)\sin\varphi \approx \chi(r_{\max})\sin\varphi$ that effectively removes the need to consider the radial dependence of the beam's OAM. From this analysis, the relative probability of finding an electron of OAM $\ell\hbar$ in the resulting beam is given by the coefficient $|c_\ell|^2 = \left|J_{|\ell|}(\chi(r_{\max}))\right|^2$ that will also yield the beam's observed OAM distribution as a function of ℓ. This analysis, in agreement with a more rigorous approach based on numerical calculations and also an analytical approach (see Supplementary Note 5), reveals that the dominant decomposition coefficients of such an electron's spectrum will be attributed to ℓ values satisfying $|\ell| \approx \chi$.

Using the sorter, the OAM content of the wavefunction after its interaction with the dipole was recorded and is shown in Fig. 3c. We find that the beam's OAM content is mostly distributed near $\ell = \pm 5$, thus implying that the dipole is defined by a χ value of ~ 5 rad. This value roughly translates to a magnetic dipole moment of $\mathcal{M} \approx 6.2\times10^9\,\mu_B$, where μ_B is the Bohr magneton, and is in good agreement with our estimated value of the structure's saturated magnetic dipole moment of $6.7\times10^9\,\mu_B$. The corresponding numerically simulated OAM spectrum based on these parameters is also included in Fig. 3c. These numerical results were obtained using our simplified model where we assume that $\chi(r)\sin\varphi \approx \chi(r_{\max})\sin\varphi$ and are in good agreement with data based on the saturation field of the wire.

Discussion

In comparison with other methods used to examine magnetic fields (c.f., refs 21,30,31), the OAM sorter proves its effectiveness by readily providing the beam's OAM spectrum. For an identical number of detected electrons, this content is defined by an image showing 20 $|c_\ell|^2$ OAM coefficients yielding more information about a beam's phase than an image obtained using holographic methods. Moreover, such images do not allow a direct measurement of a sample's magnetic information. Instead, this quantity has to be extrapolated from the field in the dipole's proximity. In addition, the OAM sorter method does not rely on any phase wrapping or unwrapping methodology, thereby simplifying a magnetic field's analysis. Further developments could also allow the improvement of this device and the possibility to exploit it in atomic scale measurements or in conjunction with scanning electron probes. Given that the sorter only requires the phase masks in two distinct planes, then its performance will become more effective if absorptive elements like phase holograms were substituted by structured electrostatic fields[32].

Our sorter method also possesses the following prospective extensions. On the one hand, when using the sorter to analyse magnetic structures, the radial dependence of the phase added by such structures can be lowered by exposing them to a beam already carrying a known OAM value. This will cause the beam to have a maximal intensity at a certain radius r_ℓ. Therefore, the majority of the beam's electrons that have interacted with the structure acquire a phase whose radial dependence will be attributed to r_ℓ. Much like how we approximated the phase acquired by electrons to be predominantly defined by the truncation radius of our apparatus $r_{\max}$, we could likewise assign additional importance to electrons attributed to a radius of r_ℓ. Such an approximation could provide additional simplifications that are needed for matching the outcome of these magnetic measurements with theory. On the other hand, a minor modification to the sorter's schematics can be proposed to sort electron modes in a different mutually unbiased basis, namely the so-called angular basis[26]. Performing an additional set of measurements of an electron's phase in this basis could provide additional information, for example, regarding the phase of the

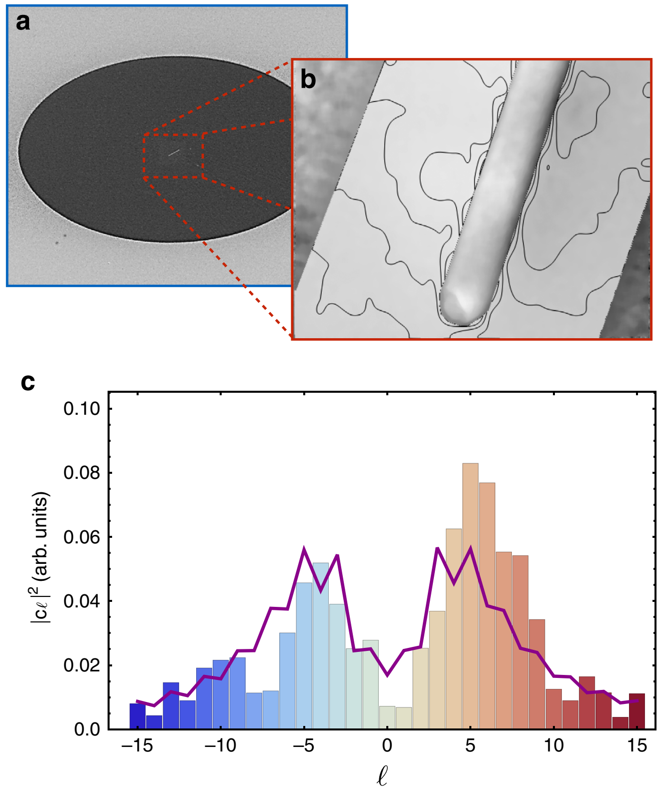

Figure 3 | OAM spectrum of a beam affected by a magnetic dipole. (**a**) Scanning electron microscopy (SEM) image of the analysed magnetic bar configurated as a dipole. The bar is defined by dimensions of 100 nm (thickness) by 200 nm (width) by 2.8 μm (length). (**b**) Magnetic field lines of the magnetic bar measured using electron holography. (**c**) Expected (curve) and obtained (bars) OAM spectrum acquired by the electron beam upon interacting with the magnetic bar. The expected curve was calculated assuming that its magnetic field is saturated. Unlike the measurement performed in (**b**), the experimental data were obtained while the dipole was exposed to a field in the condenser plane of the electron microscope.

OAM expansion coefficients c_ℓ[33], concerning the interaction of a magnetic field with electron beams.

Data availability. All relevant data are available from the authors on reasonable request.

References

1. Bliokh, K. Y., Bliokh, Y. P., Savel'ev, S. & Nori, F. Semiclassical dynamics of electron wave packet states with phase vortices. *Phys. Rev. Lett.* **99,** 190404 (2007).
2. Lloyd, S., Babiker, M. & Yuan, J. Quantized orbital angular momentum transfer and magnetic dichroism in the interaction of electron vortices with matter. *Phys. Rev. Lett.* **108,** 074802 (2012).
3. Asenjo-Garcia, A. & de Abajo, F. G. Dichroism in the interaction between vortex electron beams, plasmons, and molecules. *Phys. Rev. Lett.* **113,** 066102 (2014).
4. Kaminer, I. *et al.* Quantum čerenkov radiation: spectral cutoffs and the role of spin and orbital angular momentum. *Phys. Rev. X* **6,** 011006 (2016).
5. Kaminer, I., Nemirovsky, J., Rechtsman, M., Bekenstein, R. & Segev, M. Self-accelerating dirac particles and prolonging the lifetime of relativistic fermions. *Nat. Phys.* **11,** 261–267 (2015).
6. Bliokh, K. Y., Schattschneider, P., Verbeeck, J. & Nori, F. Electron vortex beams in a magnetic field: A new twist on landau levels and aharonov-bohm states. *Phys. Rev. X* **2,** 041011 (2012).
7. Schattschneider, P. *et al.* Imaging the dynamics of free-electron landau states. *Nat. Commun.* **5,** 4586 (2014).
8. Bliokh, K. Y., Dennis, M. R. & Nori, F. Relativistic electron vortex beams: angular momentum and spin-orbit interaction. *Phys. Rev. Lett.* **107,** 174802 (2011).
9. Harris, J. *et al.* Structured quantum waves. *Nat. Phys.* **11,** 629–634 (2015).
10. Uchida, M. & Tonomura, A. Generation of electron beams carrying orbital angular momentum. *Nature* **464,** 737–739 (2010).
11. Verbeeck, J., Tian, H. & Schattschneider, P. Production and application of electron vortex beams. *Nature* **467,** 301–304 (2010).
12. McMorran, B. J. *et al.* Electron vortex beams with high quanta of orbital angular momentum. *Science* **331,** 192–195 (2011).
13. Harvey, T. R. *et al.* Efficient diffractive phase optics for electrons. *New J. Phys.* **16,** 093039 (2014).
14. Grillo, V. *et al.* Highly efficient electron vortex beams generated by nanofabricated phase holograms. *Appl. Phys. Lett.* **104,** 043109 (2014).
15. Schattschneider, P., Stöger-Pollach, M. & Verbeeck, J. Novel vortex generator and mode converter for electron beams. *Phys. Rev. Lett.* **109,** 084801 (2012).
16. Clark, L. *et al.* Exploiting lens aberrations to create electron-vortex beams. *Phys. Rev. Lett.* **111,** 064801 (2013).
17. Karimi, E., Marrucci, L., Grillo, V. & Santamato, E. Spin-to-orbital angular momentum conversion and spin-polarization filtering in electron beams. *Phys. Rev. Lett.* **108,** 044801 (2012).
18. Béché, A., Van Boxem, R., Van Tendeloo, G. & Verbeeck, J. Magnetic monopole field exposed by electrons. *Nat. Phys.* **10,** 26–29 (2014).
19. Guzzinati, G., Clark, L., Béché, A. & Verbeeck, J. Measuring the orbital angular momentum of electron beams. *Phys. Rev. A* **89,** 025803 (2014).
20. Mair, A., Vaziri, A., Weihs, G. & Zeilinger, A. Entanglement of the orbital angular momentum states of photons. *Nature* **412,** 313–316 (2001).
21. Saitoh, K., Hasegawa, Y., Hirakawa, K., Tanaka, N. & Uchida, M. Measuring the orbital angular momentum of electron vortex beams using a forked grating. *Phys. Rev. Lett.* **111,** 074801 (2013).
22. Qassim, H. *et al.* Limitations to the determination of a laguerre-gauss spectrum via projective, phase-flattening measurement. *J. Opt. Soc. Am. B* **31,** A20 (2014).
23. Leach, J., Padgett, M. J., Barnett, S. M., Franke-Arnold, S. & Courtial, J. Measuring the orbital angular momentum of a single photon. *Phys. Rev. Lett.* **88,** 257901 (2002).
24. Clark, L., Béché, A., Guzzinati, G. & Verbeeck, J. Quantitative measurement of orbital angular momentum in electron microscopy. *Phys. Rev. A* **89,** 053818 (2014).
25. Berkhout, G. C., Lavery, M. P., Courtial, J., Beijersbergen, M. W. & Padgett, M. J. Efficient sorting of orbital angular momentum states of light. *Phys. Rev. Lett.* **105,** 153601 (2010).
26. Mirhosseini, M., Malik, M., Shi, Z. & Boyd, R. W. Efficient separation of the orbital angular momentum eigenstates of light. *Nat. Commun.* **4,** 2783 (2013).
27. Hossack, W., Darling, A. & Dahdouh, A. Coordinate transformations with multiple computergenerated optical elements. *J. Mod. Opt.* **34,** 1235–1250 (1987).
28. Shiloh, R., Lereah, Y., Lilach, Y. & Arie, A. Sculpturing the electron wave function using nanoscale phase masks. *Ultramicroscopy* **144,** 26–31 (2014).
29. Pozzi, G. *et al.* Experimental realization of the Ehrenberg-Siday thought experiment. *Appl. Phys. Lett.* **108,** 083108 (2016).
30. Beleggia, M., Kasama, T. & Dunin-Borkowski, R. E. The quantitative measurement of magnetic moments from phase images of nanoparticles and nanostructures—i. fundamentals. *Ultramicroscopy* **110,** 425–432 (2010).
31. Juchtmans, R. & Verbeeck, J. Local orbital angular momentum revealed by spiral-phase-plate imaging in transmission-electron microscopy. *Phys. Rev. A* **93,** 023811 (2016).
32. Beleggia, M. *et al.* Towards quantitative off-axis electron holographic mapping of the electric field around the tip of a sharp biased metallic needle. *J. Appl. Phys.* **116,** 024305 (2014).
33. Bent, N. *et al.* Experimental realization of quantum tomography of photonic qudits via symmetric informationally complete positive operator-valued measures. *Phys. Rev. X* **5,** 041006 (2015).

Acknowledgements

V.G. acknowledges the support of the Alexander von Humboldt Foundation. H.L., F.B., R.W.B. and E.K. acknowledge the support of the Canada Research Chairs (CRC) and Canada Excellence Research Chairs (CERC) Program. R.D.-B. is grateful to the European Research Council for funding under the European Union's Seventh Framework Programme (FP7/2007–2013)/ERC grant agreement number 320832.

Author contributions

V.G., R.W.B, R.E.-D., M.J.P. and E.K. conceived the idea; M.J.P, V.G., M.P.J.L., and E.K. designed the hologram; F.V., G.C.G., P.-H.L., and E.M. fabricated the hologram; F.V., G.C.G., and S.F. fabricated the magnetic pillar; A.H.T., V.G., S.F. and R.B. performed the experiment; V.G., and A.H.T analysed the data; V.G., H.L., F.B., and E.K developed the application theory; H.L., F.B., and E.K. with the help from other authors wrote the manuscript. All authors discussed the results and contributed to the text of the manuscript.

Additional information

Supplementary Information accompanies this paper at http://www.nature.com/naturecommunications

Competing interests: The authors declare no competing financial interests.

Reprints and permission information is available online at http://npg.nature.com/reprintsandpermissions/

How to cite this article: Grillo, V. *et al.* Measuring the orbital angular momentum spectrum of an electron beam. *Nat. Commun.* **8**, 15536 doi: 10.1038/ncomms15536 (2017).

Chapter 4

Nondestructive OAM measurement for electron waves

This chapter is based on the following paper:

1. **H. Larocque**, F. Bouchard, V. Grillo, A. Sit, S. Frabboni, R. E. Dunin-Borkowski, M. J. Padgett, R. W. Boyd, and E. Karimi, "Nondestructive measurement of orbital angular momentum for an electron beam," *Physical Review Letters* **117**, 154801 (2016).

DOI: https://doi.org/10.1103/PhysRevLett.117.154801

The OAM measurement methods introduced in the previous chapter rely on drastically modifying the transverse profile of a structured wave such that it can spatially separate the beam's OAM components. These components can thereafter be found in regions where the wave is almost entirely defined by components that originally carried a known OAM value. A device relying on phase-flattening can only perform this separation for one OAM component under a single configuration. OAM sorters, however, can in principle perform a full OAM decomposition under a unique configuration. The relative intensity, or particle flux, in these regions is then measured using conventional detectors such as photo-diodes in order to reconstruct the wave's OAM content.

The publication on which this chapter is based proposes an OAM-measurement method for electron waves that does not rely on such spatial decompositions nor on the use of conventional detectors [50]. Instead, it relies on coupling the OAM-dependent electrodynamic properties of electron waves with a device from which an OAM-dependent indicator can be extracted. Unlike conventional detectors, this device does not absorb the electron nor does it hinder its movement. Furthermore, unlike phase-flattening or sorting schemes, it does not perform any modal transformations on the electron wave itself. For these reasons, this method can tentatively be considered as nondestructive. Let it be noted that this terminology does not refer to the quantum nature of the device's measurement process. Namely, for an electron wave in a superposition of OAM states, the action of performing a measurement on it should still project the electron's state onto a single OAM state which will be detected by the device.

4.1 Magnetic properties of electron waves

The magnetic property that is of interest to the work presented in this chapter relies on the azimuthal transverse phase profile of OAM-carrying electron wavefuntions. Namely, a free electron carrying $\hbar\ell$ units of OAM can be represented by a time-independent wavefunction of the form $\psi(\mathbf{r}) = f(\rho, z)\exp(i\ell\varphi)$, where $\mathbf{r}$ is the position vector, (ρ, φ, z) are the cylindrical coordinates, and f is an unknown function that is square-integrable in three-dimensional space. As mentioned in chapter 2, such wavefunctions are defined by a central phase singularity which leads to a null in their probability density function $|\psi(\mathbf{r})|^2$, provided that $\ell \neq 0$. This form also leads to distinct properties in the wavefunction's probability density current $\mathbf{j} = -i\hbar(\psi^*\boldsymbol{\nabla}\psi - \psi\boldsymbol{\nabla}\psi^*)/2m_e$, where m_e is the electron's mass. Namely, OAM-carrying wavefunctions are defined by an azimuthal component in their probability density current $\mathbf{j}_\varphi = \hbar\ell\,|f(\rho, z)|^2\,/m\rho$, which is directly proportional to the OAM carried by the particle [1]. Given that electrons are charged entities, this azimuthal probability current density manifests itself as an electrical current density from which some magnetic properties arise. One of these properties consists of an OAM-dependent magnetic dipole moment $\mu = \ell\mu_B$, where $\mu_B = e\hbar/2m_e$ is the Bohr magneton and e is the charge of the electron [51]. As seen in the following publication, coupling this magnetic dipole moment with a conductive loop of current can be used to nondestructively measure an electron wave's OAM.

Nondestructive Measurement of Orbital Angular Momentum for an Electron Beam

Hugo Larocque,[1] Frédéric Bouchard,[1] Vincenzo Grillo,[2] Alicia Sit,[1] Stefano Frabboni,[2,3] Rafal E. Dunin-Borkowski,[4] Miles J. Padgett,[5] Robert W. Boyd,[1,6] and Ebrahim Karimi[1,7,*]

[1]The Max Planck Centre for Extreme and Quantum Photonics, Department of Physics, University of Ottawa, 25 Templeton Street, Ottawa, Ontario K1N 6N5, Canada

[2]CNR-Istituto Nanoscienze, Centro S3, Via G Campi 213/a, I-41125 Modena, Italy

[3]Dipartimento FIM Universitá di Modenae Reggio Emilia, Via G Campi 213/a, I-41125 Modena, Italy

[4]Ernst Ruska-Centre for Microscopy and Spectroscopy with Electrons, Forschungszentrum Jülich, Jülich 52425, Germany

[5]School of Physics and Astronomy, Glasgow University, Glasgow G12 8QQ, United Kingdom

[6]Institute of Optics, University of Rochester, Rochester, New York 14627, USA

[7]Department of Physics, Institute for Advanced Studies in Basic Sciences, 45137-66731 Zanjan, Iran

(Received 18 April 2016; published 7 October 2016)

Free electrons with a helical phase front, referred to as "twisted" electrons, possess an orbital angular momentum (OAM) and, hence, a quantized magnetic dipole moment along their propagation direction. This intrinsic magnetic moment can be used to probe material properties. Twisted electrons thus have numerous potential applications in materials science. Measuring this quantity often relies on a series of projective measurements that subsequently change the OAM carried by the electrons. In this Letter, we propose a nondestructive way of measuring an electron beam's OAM through the interaction of this associated magnetic dipole with a conductive loop. Such an interaction results in the generation of induced currents within the loop, which are found to be directly proportional to the electron's OAM value. Moreover, the electron experiences no OAM variations and only minimal energy losses upon the measurement, and, hence, the nondestructive nature of the proposed technique.

DOI: 10.1103/PhysRevLett.117.154801

Introduction.—Electrons can possess net quantized orbital angular momentum (OAM) while undergoing free-space propagation [1]. The wave function ψ associated with such an electron includes an $\exp(i\ell\varphi)$ term arising from its helical phase fronts, where ℓ and φ are an integer and the azimuthal coordinate, respectively. Beams consisting of these "twisted" electrons are referred to as electron vortex beams. Different techniques, such as direct imprinting of a phase variation [2], amplitude [3] and phase [4] holograms, and magnetic needles [5] have experimentally been shown to generate such electron beams. In turn, these electron beams possess quantized OAM and circulating current densities J_φ in a plane orthogonal to their propagation direction. It thus follows that these current densities cause twisted electron beams to carry a magnetic dipole moment $\ell\mu_B$ in addition to their intrinsic spin magnetic dipole moment $\pm\mu_B$, where μ_B is the Bohr magneton [6]. Hence, unlike its intrinsic spin, the magnetic moment associated with its twisted wave front is in principle unbounded, allowing values as high as $200\mu_B$ to be achieved experimentally [7,8]. Such a large unbounded magnetic moment may find applications in materials science [9], overcoming the fact that the generation of spin-polarized electron beams has historically been affected by empirical and fundamental difficulties [10]. Among future potential applications are investigations related to magnetic dichroism in materials [11], the fundamental nature of radiation [12], exotic physics such as virtual forces [13], and the interaction of twisted electrons with light beams [14]. Many of these examples require the analysis of the electron beam's OAM content, a process adopted from its optical counterparts and that is usually carried out by making the beam go through phase-flattening projective measurements by means of phase holograms [15–17]. However, the analysis of each OAM component requires the use of a distinct hologram, which can make the investigation of a beam's OAM components long, tedious, and inefficient. Moreover, the beam's OAM content, after passing through a phase mask, will have a value different from that of the initial state [16].

In this Letter, we propose an alternative way of measuring an electron beam's OAM relying on electric fields induced by time-varying magnetic fields. The principle of our technique is related to one where a magnet is dropped through a conductive tube (or ring). The falling motion of the magnet generates currents within the tube, that in turn produce a magnetic force countering the magnet's descent [18–20]. By using a similar reasoning, in the nonrelativistic regime, one can calculate the induced current inside a microscale conductive ring due to the motion of an OAM-carrying electron traveling through it. Because the electron's OAM and magnetic moment are quantized, the magnetic field emanating from the electron will also be quantized and will produce discrete induced currents inside the ring that can be related directly to the OAM carried by the electron.

Theory.—We use a semiclassical approach to describe the interaction between a propagating electron vortex beam and a conductive material. Let us consider an electron with a rest mass m_e propagating along a specific axis, e.g., the z axis, and possessing a well-defined central kinetic energy $\mathcal{E}$ and momentum p_0, where c is the velocity of light in vacuum. Under the slowly varying amplitude approximation, the wave packet associated with this electron must satisfy the paraxial Schrödinger equation. The corresponding wave function is quantized, and holds a specific shape based on its initial probability and phase distribution conditions. For instance, it may be quantized in the transverse plane as well as in the longitudinal direction [1], which yields the following wave packet in cylindrical coordinates r, φ, z,

$$\psi_{p,\ell,n}(r,\varphi,z;t) = u^{\mathrm{LG}}_{p,\ell}(r,\varphi;t)u^{\mathrm{HG}}_{n}(\zeta)e^{i(p_0 z-\mathcal{E}t)/\hbar}, \quad (1)$$

where u^{LG} and u^{HG} are Laguerre-Gauss and Hermite-Gauss modes [21], respectively, in which p and n are positive integers defining the electron's distribution in the transverse plane and the longitudinal direction. ℓ is an integer number that is associated with the OAM carried by the beam and also defines its transverse distribution. The electron wave packet's center of mass is denoted by $\zeta = z - p_0 t/m_e$, while $\hbar$ is the reduced Planck constant. On account of the electron's OAM, its rest frame four-current density consists only of a scalar and an azimuthal component, according to the expression

$$\mathbf{j}^{\alpha}_{\mathrm{rest}} = (c\rho, J_r, J_\varphi, J_z) = \left(-ce\mathcal{P}, 0, \frac{\hbar\ell}{m_e r}\mathcal{P}, 0\right), \quad (2)$$

where ρ, J_r, J_φ, and J_z correspond to charge density and radial, azimuthal, and longitudinal current densities, respectively, while $\mathcal{P} = \mathcal{P}(r',\varphi';z') = |\psi_{p,\ell,n}(r,\varphi,z;t)|^2$ is the probability density function of the electron's position in its rest frame defined by the coordinates r', φ', z', and $-e$ is the electron charge. The four-current densities in the laboratory frame that the electron perceives as traveling along the z direction can then be calculated via an inverse Lorentz transformation, $\mathbf{j}^{\alpha}_{\mathrm{lab}} = (\Lambda^{\alpha}_{\beta})^{-1}\mathbf{j}^{\beta}_{\mathrm{rest}}$, yielding $\mathbf{j}^{\alpha}_{\mathrm{lab}} = [-ce\gamma\mathcal{P}, 0, (\hbar\ell/m_e r)\mathcal{P}, -\gamma\beta ce\mathcal{P}]$, where Λ^{α}_{β} is the Lorentz transformation matrix, $\beta = p_0/(m_e c)$, and $\gamma = (1-\beta^2)^{-1/2}$ [22]. Likewise, a Lorentz boost along the z axis must also be applied to the electron's rest-frame coordinates to express its current densities with respect to the laboratory frame coordinates, i.e., $\mathbf{x}^{\alpha}_{\mathrm{lab}} = (\Lambda^{\alpha}_{\beta})^{-1}\mathbf{x}^{\beta}_{\mathrm{rest}}$, where $\mathbf{x}^{\alpha} = (ct, \mathbf{r})$. One may associate the first, third, and last terms of the four-vector current density with an electrostatic potential $\mathcal{V}$ and the azimuthal and longitudinal vector potentials $\mathbf{A}_\varphi$ and $\mathbf{A}_\parallel$, respectively. The azimuthal current density $J_\varphi = (\hbar\ell/m_e r)\mathcal{P}\mathbf{e}_\varphi$ generates a magnetic field $\mathbf{B} = \nabla \times \mathbf{A}$ oriented along the electron's propagation direction, i.e., the z axis, where ∇ is the gradient operator and $\mathbf{e}_\varphi$ is the azimuthal unit vector. The vector potential $\mathbf{A}_\varphi$ at a given position $\mathbf{r}$ can then be expressed directly as a solution to one of Poisson's equations, namely, $\mathbf{A}_\varphi(\mathbf{r}) = \mu_0/(4\pi)\int d^3\mathbf{r}' G(\mathbf{r},\mathbf{r}')J_\varphi(\mathbf{r}')$, where $G(\mathbf{r},\mathbf{r}') = |\mathbf{r}-\mathbf{r}'|^{-1}$ is the corresponding Green function. The electron's transverse motion for any value of ℓ is then considered as a "localized" current loop defined by $I_e = e\hbar/(\pi m_e w_0^2)\mathbf{e}_\varphi$, as prescribed by the relation $\ell\mu_B = I_e(\pi r_\ell^2)$, where $r_\ell = w_0\sqrt{\ell/2}$ is the radius at which an electron is maximally distributed and w_0 is the minimum radius of its Gaussian distribution.

The vector potential associated with such an azimuthal current can be expressed in the form

$$\mathbf{A}_\varphi(r,z) = \frac{\mu_0 I_e \eta}{\pi v^{3/2}}[uK(2\eta^2) - (u+v)E(2\eta^2)], \quad (3)$$

where $u = r_\ell^2 + r^2 + z^2$, $v = 2r_\ell r$, $\eta = v^{1/2}(u+v)^{-1/2}$, and $K(\cdot)$ and $E(\cdot)$ are the complete elliptic integrals of the first and second kind, respectively [22]. As depicted in Fig. 1, we consider such electrons passing through a tube of thickness w, radius a, conductivity σ, and length L. The tube radius is large enough to ensure that the electron's wave function nearly vanishes at its inner radius. In particular, for $p = 0$ mode distributions defined by an arbitrary ℓ index, the tube radius a is chosen to be much greater than the radius r_ℓ, i.e., $a \gg r_\ell$. The conductive tube can be considered as a sequence of infinitesimal circle loops positioned at a longitudinal distance h from the tube's center. As predicted by Faraday's law of induction, when the twisted electron travels through the tube, its longitudinal magnetic field induces an eddy current in each of the tube's infinitesimal loops. According to Lenz's law, the direction of these currents must generate a magnetic field

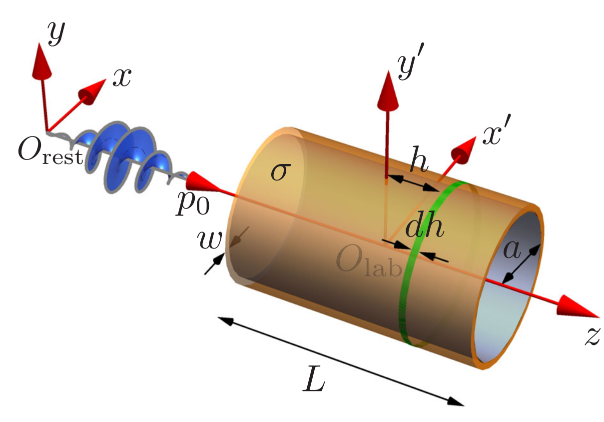

FIG. 1. System in which an electron vortex beam with a central energy $\mathcal{E}$ and momentum p_0, which is in its lower longitudinal mode $[u^{\mathrm{LG}}_{p,\ell}(r,\varphi;t)u^{\mathrm{HG}}_{0}(\zeta)e^{i(p_0 z-\mathcal{E}t)/\hbar}]$, propagates through a cylinder with conductivity σ and permeability μ. The relative motion of both entities results in the generation of a current in the infinitesimal loop of thickness dh.

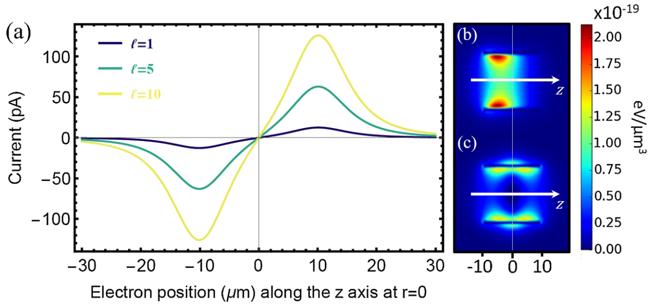

FIG. 2. (a) Theoretically calculated total induced current in a conductive tube by an electron vortex beam. We assumed that the electron beam carries OAM of $\ell = 1$, 5 and 10, and that the conductive tube is made of platinum. Longitudinal cross section of the tube depicting the relative magnetic energy density generated by its induced eddy currents when an electron consisting of a high OAM quantum ($\ell = 100$) is (b) entering the tube and (c) in the middle of the tube. Here, we assumed an electron beam with central energy $\mathcal{E} = 100$ keV and a platinum tube with length $L = 20$ μm, thickness $w = 1$ μm, and radius $a = 10$ μm.

that is opposed to the motion of the electron beam. Its value, however, will depend on the time variation of the magnetic flux Φ_B through each loop, i.e., $-\partial_t \Phi_B$. Neither the electrostatic potential $\mathcal{V}$ nor the longitudinal vector potential $\mathbf{A}_\parallel$ contributes to the magnetic flux Φ_B. Only the azimuthal vector potential $\mathbf{A}_\varphi$ is relevant to the analysis. Because of the cylindrical symmetry of the electron-tube system, the vector potential is also independent of φ. The induced electric field on the circle loop located at position h, and hence the induced current, is therefore azimuthal and expressed as $E_\varphi = -\partial_t \mathbf{A}_\varphi(a, z-h)$, where z is the electron's relative longitudinal position. One can show, by means of Ohm's law, $dI = \sigma E_\varphi(w dh)$, that the total current within the tube induced by an electron with a magnetic dipole moment $\ell \mu_B$ is given by the expression

$$I = \frac{3}{4\pi}\left(\frac{p_0}{m_e}\right)(\sigma\mu w a)(\ell\mu_B)\int_{-L/2}^{L/2}\frac{\gamma^2(z-h)dh}{[a^2+\gamma^2(z-h)^2]^{5/2}}, \quad (4)$$

where μ is the tube's permeability. The proportionality of this relation describes the quantization of the induced current within the tube due to the discrete nature of the electron's OAM. By integrating Eq. (4), an analytical expression for this current can be obtained and is plotted as a function of electron position relative to the cylinder's center in Fig. 2(a) for various values of electron OAM. As a result, one can conceive a device for OAM measurement by detecting the corresponding quantized current induced inside a tube or a thin loop circuit. As shown in Fig. 2(a), currents of the order of 10's of pA are induced in the loop and could be potentially read out using an ampere meter (e.g., Tektronix 6485 Picoammeter). Therefore, this technique can potentially be used to measure OAM values of twisted electron beams. The direction of the induced current additionally provides information on the sign of the OAM value. Moreover, since the generated current is directly proportional to the material's conductivity, it follows that by using a more conductive material, one could increase the current by several orders of magnitude. Though these induced currents are rather short-lived, a combination of fast electronics, optimized cylinder dimensions, and secondary methods, such as autocorrelation techniques, can be used to overcome experimental difficulties related to the short interaction between the electron and the cylinder [23]. Our proposed technique has no influence on the OAM of the electron beam since the electron's canonical OAM is conserved in the presence of an external longitudinal magnetic field [24]. The only property that the measurement affects is the energy carried by the electron [25]. This is due to the fact that the induced currents will counter the motion of the electron. The energy loss due to the electron-tube interaction is $\Delta\mathcal{E} = -(2\pi\sigma a w)(p_0/m_e)\int_{-\infty}^{+\infty} dz \int_{-L/2}^{L/2}[\partial_z \mathbf{A}_\varphi(a, z+h)]^2 dh$, which slightly decelerates the electron. This deceleration can potentially reach a relatively high value, resulting in a large radiated electromagnetic power emitted from the electron, as indicated by the Larmor formula. However, due to its very short time of interaction with the tube, the energy lost by the electron can only realistically reach a value on the order of 10^{-20} eV when an electron with an OAM $\ell = 100$ is considered (we assume the parameters reported in Fig. 2). Such energy values are obtained when deducing the force applied on the electron by the tube. Another way of obtaining insight on the electron's energy loss is to calculate the total energy contained within the fields generated by the relative motion of the electron. This energy can be calculated numerically by first finding the magnetic field generated by the cylinder's loops of currents using the Biot-Savart law [26] and then integrating the total energy stored in these magnetic fields and within the electric fields associated with the currents themselves. In particular, this method was employed to produce the energy density plots found in Figs. 2(b) and 2(c). One can see that the act of measuring the electron's OAM has nearly no effect on the electron itself. Indeed, unlike projective measurement techniques, where the electron's phase front is flattened and projected on a Gaussian mode, the electron's OAM does not change during the measurement. For these reasons, the electron's motion through the tube leaves it largely unperturbed. Up until this point, we only considered the case where an electron travels perfectly along the center of the tube. A simple extension of this analysis reveals that the calculated induced currents are not significantly affected by breaking the apparatus's cylindrical symmetry. We further discuss how the currents are affected by asymmetries in experimental apparatuses in the Supplemental Material [23].

This nondestructive approach to measuring OAM may create a conceptual paradox. One may mistakenly argue

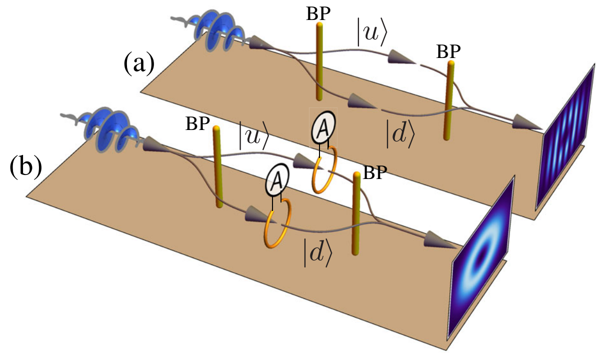

FIG. 3. Proposed experiment in which the effect of conductive circuits in an OAM-carrying electron double-slit experiment is considered. (a) The electron double-slit experiment in which no circuits are present. (b) The electron double-slit experiment in which a circuit is present in each of the possible paths, $|u\rangle$ or $|d\rangle$, taken by the electron where the coefficient $\alpha = 0$ (i.e., the electron and the loops are perfectly coupled). BP annotations refer to biprisms.

that because this measurement leaves the electron's quantum state (OAM and energy) unchanged, it could challenge the validity of a wave particle duality experiment (quantum complementarity). Consider a double-slit experiment in which, due to an electrostatic interaction, the electron wave function is split into two parts $|u\rangle$ and $|d\rangle$. Both parts are then coherently recombined and interfere at a screen, as illustrated in Fig. 3(a) [27]. The electron's state can be described as a superposition of both paths, as if it is in a coherent superposition of states $|u\rangle$ and $|d\rangle$, resulting in the formation of an interference pattern on the screen. In the case when the electron is equally likely to take each path, its state may be described as $|\psi\rangle = (|u\rangle + e^{i\delta}|d\rangle)/\sqrt{2}$, where δ is the relative phase between the states. The corresponding density matrix is pure, $\rho \coloneqq |\psi\rangle\langle\psi| = (|u\rangle\langle u| + e^{-i\delta}|u\rangle\langle d| + e^{i\delta}|d\rangle\langle u| + |d\rangle\langle d|)/2$. In this expression, the terms $e^{-i\delta}|u\rangle\langle d|$ and $e^{i\delta}|d\rangle\langle u|$ carry the interference pattern's phase information and can therefore be associated with the fringe visibility, which is unity for this ideal case. The terms $|u\rangle\langle u|$ and $|d\rangle\langle d|$, respectively, describe the probability of finding an electron in the $|u\rangle$ or $|d\rangle$ path, both of which are equiprobable events for this case [28].

Now, consider two conductive circuits introduced into each of the possible paths, as shown in Fig. 3(b). As mentioned above, these circuits have the capacity to measure an electron's OAM with minimal energy loss, allowing for the detection of whether an OAM-carrying electron has taken a given path. When no electron travels through the circuit, the circuit is in a state $|0\rangle_c$. When an electron with an OAM number ℓ travels through the circuit, it will induce a quantized current, changing the circuit to a state defined by $|i^\ell\rangle_c$, which can be expressed as a superposition of the loop's current eigenstates $|n\rangle_c$, i.e., $|i^\ell\rangle_c = \sum_n c_n|n\rangle_c$, where $c_n = \langle n|i^\ell\rangle_c$ is an expansion coefficient depending on various experimental parameters describing the interaction between the free electron and the loop itself. Hence, the system consisting of both circuits can be described by the tensor product $|i_u\rangle_c|i_d\rangle_c$, where $|i_u\rangle_c$ and $|i_d\rangle_c$, respectively, represent the state associated with the electrical current going through circuits in the $|u\rangle$ and $|d\rangle$ paths. Because the circuit has the ability to provide information about which path the electron has taken, it provides information about the particle nature of the electron, while the presence of fringes gives information about its wave nature. Therefore, the presence of currents and fringes would seemingly allow one to detect both the electron's wave and particle nature simultaneously, violating the principle of complementarity.

However, prior to going through any of the circuits, the system consisting of the electron and the two circuits can initially be expressed as $|\psi_i\rangle = (1/\sqrt{2})(|u\rangle + e^{i\delta}|d\rangle)|0_u\rangle_c|0_d\rangle_c$. After the electron has gone through either of the circuits, the system's final wave function becomes $|\psi_f\rangle = (1/\sqrt{2})(|u\rangle|i_u^\ell\rangle_c|0_d\rangle_c + e^{i\delta}|d\rangle|0_u\rangle_c|i_d^\ell\rangle_c)$, where the electron is entangled with the circuits. The circuits thus act as a nonlocal "environment" and cause the electron state to partially decohere [29]. In order to observe the effect of the circuits' presence on the obtained interference pattern, we take the partial trace over the circuits' states. The reduced density matrix will correspond to $(|u\rangle\langle u| + e^{-i\delta}\alpha|u\rangle\langle d| + e^{i\delta}\alpha^*|d\rangle\langle u| + |d\rangle\langle d|)/2$, where $\alpha = \langle 0_u|i_u^\ell|\rangle\langle i_d^\ell|0_d\rangle$. One can observe that the visibility terms of the reduced density matrix in the $\{|u\rangle, |d\rangle\}$ basis will be modified by the factor $\alpha < 1$, where for identically coupled circuits, i.e., $|i_d^\ell\rangle = |i_u^\ell\rangle$, $\alpha = |c_0|^2$. This coefficient, defined by $\langle 0|i^\ell\rangle_c$, will vary with the coupling between the free electron and the circuit's state, which is determined by various experimental parameters. Such parameters, which include the circuit's radius, for instance, can be modified to provide a varying α coefficient affecting the fringe visibility.

In conclusion, we present a nondestructive technique that can be used to measure the OAM of an electron beam. The technique is based on the interaction of the quantized magnetic dipole moment of the twisted electron and a conductive tube. The beam's OAM components are measured by detecting the quantized induced eddy currents in the tube. These electrons suffer minimal energy losses and the method is nondestructive. To illustrate the limitations of the method, we also describe the possibility of using such a device in a gedanken quantum experiment, in which the knowledge of an electron's presence is needed. Doing so would result in reducing the visibility of observed interference as prescribed by complementarity. A prospective extension to the method could be using the tube to generate radiation with an approach similar to that of Ref. [30] through the formation of plasmons by introducing a discontinuity in the tube, such as the absence of conductive material at a given azimuthal angle.

However, this would result in larger energies being lost by passing electrons. This method's minimal electron energy loss is an essential aspect to its nondestructive nature which, along with the preservation of the electron's original OAM, presents this technique as a viable alternative to modern projective measurements.

E. K. thanks Professor Gerd Leuchs and Professor Israel De Leon for fruitful discussions involving the topic. H. L., F. B, A. S., R. W. B., and E. K. acknowledge the support of the Canada Research Chairs (CRC) and Canada Excellence Research Chairs (CERC) Program. R. E. D.-B. thanks the European Research Council for an Advanced Grant.

*ekarimi@uottawa.ca

[1] K. Y. Bliokh, Y. P. Bliokh, S. Savel'ev, and F. Nori, Phys. Rev. Lett. **99**, 190404 (2007).
[2] M. Uchida and A. Tonomura, Nature (London) **464**, 737 (2010).
[3] J. Verbeeck, H. Tian, and P. Schattschneider, Nature (London) **467**, 301 (2010).
[4] V. Grillo, G. C. Gazzadi, E. Karimi, E. Mafakheri, R. W. Boyd, and S. Frabboni, Appl. Phys. Lett. **104**, 043109 (2014).
[5] A. Béché, R. Van Boxem, G. Van Tendeloo, and J. Verbeeck, Nat. Phys. **10**, 26 (2014).
[6] K. Y. Bliokh, P. Schattschneider, J. Verbeeck, and F. Nori, Phys. Rev. X **2**, 041011 (2012).
[7] B. J. McMorran, A. Agrawal, I. M. Anderson, A. A. Herzing, H. J. Lezec, J. J. McClelland, and J. Unguris, Science **331**, 192 (2011).
[8] V. Grillo, G. C. Gazzadi, E. Mafakheri, S. Frabboni, E. Karimi, and R. W. Boyd, Phys. Rev. Lett. **114**, 034801 (2015).
[9] J. Harris, V. Grillo, E. Mafakheri, G. C. Gazzadi, S. Frabboni, R. W. Boyd, and E. Karimi, Nat. Phys. **11**, 629 (2015).
[10] E. Karimi, L. Marrucci, V. Grillo, and E. Santamato, Phys. Rev. Lett. **108**, 044801 (2012).
[11] S. M. Lloyd, M. Babiker, J. Yuan, and C. Kerr-Edwards, Phys. Rev. Lett. **109**, 254801 (2012).
[12] I. P. Ivanov and D. V. Karlovets, Phys. Rev. A **88**, 043840 (2013).
[13] I. Kaminer, J. Nemirovsky, M. Rechtsman, R. Bekenstein, and M. Segev, Nat. Phys. **11**, 261 (2015).
[14] A. G. Hayrapetyan, O. Matula, A. Aiello, A. Surzhykov, and S. Fritzsche, Phys. Rev. Lett. **112**, 134801 (2014).
[15] A. Mair, A. Vaziri, G. Weihs, and A. Zeilinger, Nature (London) **412**, 313 (2001).
[16] H. Qassim, F. M. Miatto, J. P. Torres, M. J. Padgett, E. Karimi, and R. W. Boyd, J. Opt. Soc. Am. B **31**, A20 (2014).
[17] K. Saitoh, Y. Hasegawa, K. Hirakawa, N. Tanaka, and M. Uchida, Phys. Rev. Lett. **111**, 074801 (2013).
[18] W. M. Saslow, Am. J. Phys. **60**, 693 (1992).
[19] C. S. MacLatchy, P. Backman, and L. Bogan, Am. J. Phys. **61**, 1096 (1993).
[20] G. Donoso, C. L. Ladera, and P. Martín, Am. J. Phys. **79**, 193 (2011).
[21] A. E. Siegman, *Lasers* (University Science Books, Mill Valley, 1986), p. 647.
[22] J. D. Jackson, *Classical Electrodynamics* (Wiley, New York, 1999).
[23] See Supplemental Material at http://link.aps.org/supplemental/10.1103/PhysRevLett.117.154801 for further details.
[24] C. R. Greenshields, R. L. Stamps, S. Franke-Arnold, and S. M. BarnettPhys. Rev. Lett. **113**, 240404 (2014).
[25] Because of the interaction with the very weak induced magnetic field, the twisted electron beam gains a negligible global phase of 10^{-28} rad; see, e.g., C. Greenshields, R. L. Stamps, and S. Franke-Arnold, New J. Phys. **14**, 103040 (2012).
[26] R. Good, Eur. J. Phys. **22**, 119 (2001).
[27] Y. Hasegawa, K. Saitoh, N. Tanaka, S. Tanimura, and M. Uchida, J. Phys. Soc. Jpn. **82**, 033002 (2013).
[28] B.-G. Englert, Phys. Rev. Lett. **77**, 2154 (1996).
[29] W. H. Zurek, Rev. Mod. Phys. **75**, 715 (2003).
[30] Z. Mohammadi, C. P. Van Vlack, S. Hughes, J. Bornemann, and R. Gordon, Opt. Express **20**, 15024 (2012).

Chapter 5

Structured waves in exotic systems

This chapter is based on the following papers:

1. F. Bouchard, **H. Larocque**, A. M. Yao, Ch. Travis, I. De Leon, A. Rubano, E. Karimi, G.-L. Oppo, and R. W. Boyd, "Polarization shaping for control of nonlinear propagation", *Physical Review Letters* **117**, 233903 (2016).

   DOI: https://doi.org/10.1103/PhysRevLett.117.233903

2. **H. Larocque**, I. Kaminer, V. Grillo, R. W. Boyd, and E. Karimi, "Twisting neutrons may reveal their internal structure" *Nature Physics* **14**, 1–2 (2018).

   DOI: https://doi.org/10.1038/nphys4322

The previous chapters explore methods that mostly involve structured waves of relatively simple particles experiencing free-space propagation. This chapter centres on the properties of structured waves that do not experience this free-space propagation or of those that are made of particles with an internal structure. In particular, we investigate the nonlinear dynamics of optical waves with either phase or polarization singularities upon propagation through a nonlinear medium [52]. Moreover, we examine how the internal structure of a particle such as a neutron is manifested in its electromagnetic properties upon structuring its wavefunction [53].

5.1 Structured light in nonlinear media

The nonlinearities of an optical medium can often be accounted for by a nonlinear term in the medium's polarization vector, i.e. $\mathbf{P} = \varepsilon_0\chi^{(1)}\mathbf{E} + \mathbf{P}_{\mathrm{NL}}$, where ε_0 is the permittivity of free-space, $\chi^{(1)}$ is the linear first-order electric susceptibility of the medium, $\mathbf{E}$ is the electric field, and $\mathbf{P}_{\mathrm{NL}}$ is the nonlinear term of the medium's polarization. The nature of this last term depends on the main nonlinear processes that occur in the considered medium [54]. Much like how a wave equation can be derived from Maxwell's equations in a linear medium, a nonlinear wave equation that accounts for this nonlinear polarization can also be derived. In three dimensions, this nonlinear wave equation is given by:

$$\boldsymbol{\nabla}^2\mathbf{E}(\mathbf{r},t) - \frac{1}{(c/n_0)^2}\frac{\partial^2}{\partial t^2}\mathbf{E}(\mathbf{r},t) = \frac{1}{\varepsilon_0 c^2}\frac{\partial^2}{\partial t^2}\mathbf{P}_{\mathrm{NL}}, \tag{5.1}$$

where c is the velocity of light and n_0 is the medium's linear refractive index. As in the case of the linear wave equation, the nonlinear wave equation can also be simplified to account for paraxial waves. Namely, by assuming an electric field and a polarization of the form $\mathbf{E}(\mathbf{r},t) = \mathbf{A}(\mathbf{r})\exp\left(i(k_0 z - \omega t)\right)$ and $\mathbf{P}_{\mathrm{NL}}(\mathbf{r},t) = \mathbf{p}_{\mathrm{NL}}(\mathbf{r})\exp\left(i(k_0' z - \omega t)\right)$, the nonlinear wave equation reduces to

$$\boldsymbol{\nabla}_\perp^2\mathbf{A}(\mathbf{r}) + 2ik_0\frac{\partial}{\partial z}\mathbf{A}(\mathbf{r}) = -\frac{\omega^2}{\varepsilon_0 c^2}\mathbf{p}_{\mathrm{NL}}(\mathbf{r})e^{i\Delta k\, z} \tag{5.2}$$

where $\boldsymbol{\nabla}_\perp^2$ is the transverse Laplacian, $\Delta k = k_0 - k_0'$ is the phase matching term, and where we made the slowly varying approximation, i.e., we assumed that the second derivative of $\mathbf{A}(\mathbf{r})$ with respect to z can be neglected. Analytical solutions to Eq. (5.2) can seldom be derived. For this reason, theoretical studies involving the propagation of paraxial waves through a nonlinear medium must often be conducted numerically, including those regarding the nonlinear propagation of structured light.

5.1.1 Kerr nonlinearities

Kerr nonlinearities are third-order optical nonlinearities where, for scalar waves, $\mathbf{p}_{\mathrm{NL}}(\mathbf{r})$ in Eq. (5.2) can be represented by $p_{\mathrm{NL}} = 3\varepsilon_0\chi^{(3)}\left|A\right|^2 A$, where $\chi^{(3)}$ is the material's third-order susceptibility. Processes pertaining to these types of nonlinearities are usually phase-matched, hence $\Delta k = 0$. The fact that the medium's nonlinear polarization is proportional to the field and its absolute square essentially causes it to behave as a medium with an intensity-dependent refractive index. For Kerr nonlinearities, this quantity can be represented by $n = n_0 + \overline{n}_2 |A|^2$, where $\overline{n}_2 = 3\chi^{(3)}/4n_0$. From these definitions along with Eq. (5.2), a differential equation describing the evolution of an optical beam's transverse profile can be obtained

$$\frac{\partial}{\partial z}A(\mathbf{r}) = \frac{i}{2k_0}\boldsymbol{\nabla}_{\perp}^2 A(\mathbf{r}) + \frac{i}{2}\frac{4k_0\overline{n}_2}{n_0}|A(\mathbf{r})|^2 A(\mathbf{r}), \tag{5.3}$$

where we used the fact that $k_0 = n_0\omega/c$.

Several types of media are not described by pure Kerr nonlinearities but instead by saturable Kerr nonlinearities which can effectively be accounted for by replacing any occurrences of $|A|^2$ in nonlinear terms by $|A|^2/(1+\alpha|A|^2)$, where α is a constant that depends on the properties of the saturable Kerr medium. For these types of media, the nonlinear equation describing the propagation of an optical beam becomes

$$\frac{\partial}{\partial z}A(\mathbf{r}) = \frac{i}{2k_0}\boldsymbol{\nabla}_{\perp}^2 A(\mathbf{r}) + \frac{i}{2}\frac{4k_0\overline{n}_2}{n_0}\frac{|A(\mathbf{r})|^2}{1+\alpha|A(\mathbf{r})|^2}A(\mathbf{r}). \tag{5.4}$$

5.1.2 Beam breakup

Eqs. (5.3, 5.4) can lead to several types of nonlinear processes affecting a propagating beam's transverse profile such as self-focusing, self-trapping, and beam breakup. The latter occurs due to the amplification of irregularities in the beam's wavefronts by the nonlinear medium [55]. As a result, the beam's intensity gets shifted towards regions defined by such irregularities. This shift causes the total beam to break up into a number of filaments associated with the initial wavefront of the beam.

Given that structured light often consists of optical beams with shaped wavefronts, their nonlinear propagation through a Kerr medium often results in a beam breakup process that depends on its structured profile. This process can significantly affect the performance of applications relying on structured light in conditions defined by some types of nonlinearities. For instance, beams that have an azimuthal phase profile, i.e. $A(\mathbf{r}) \propto e^{(i\ell\varphi)}$, are known to split into $2|\ell|$ filaments upon propagating through a Kerr medium [56]. Based on previous discussions, this can intuitively be seen as arising from the beam having $|\ell|$ azimuthal positions defined by a given phase value, and $|\ell|$ azimuthal positions that are completely out of phase with respect to this value. Therefore, there are $2|\ell|$ regions that form irregularities in the beam's wavefront, which causes it to separate into $2|\ell|$ filaments.

5.1.3 Cross-phase modulation

The derivations that led to Eqs. (5.3, 5.4) account for the nonlinear propagation of a scalar wave. To account for waves that are defined by a polarization structure, one must consider the tensorial nature of the third-order susceptibility which leads to a different nonlinear polarization term in the nonlinear wave equation. In the case of third-order nonlinearities that lead to a nonlinear refractive index, several symmetry arguments can be made to simplify the elements of the third-order susceptibility tensor χ_{ijkl}, where i, j, k, l refer to Cartesian coordinates. These arguments lead to a compact form of the nonlinear polarization, which can be expressed as:

$$\mathbf{P}_{\rm NL} = \varepsilon_0 A(\mathbf{E}\cdot\mathbf{E}^*)\mathbf{E} + \frac{1}{2}\epsilon_0 B(\mathbf{E}\cdot\mathbf{E})\mathbf{E}^* \tag{5.5}$$

where, following the Maker and Terhune form, $A = 6\chi_{xxyy}$ and $B = 6\chi_{xyyx}$ [57]. Paraxial structured light beams are only defined by transverse polarization components, which allows us to neglect the z component of the electric field in Eq. (5.5). Many common polarization structured light beams can also be expressed in terms of a superposition of two oppositely circularly polarized light beams [58, 59, 25]. For this reason, it is convenient to express the beam's electric field vector in the circular polarization basis, namely as $\mathbf{E} = E_L\hat{\mathbf{e}}_{\rm L} + E_R\hat{\mathbf{e}}_{\rm R}$, where $\hat{\mathbf{e}}_{\rm L} = (\hat{\mathbf{x}} + i\hat{\mathbf{y}})/\sqrt{2}$ and $\hat{\mathbf{e}}_{\rm R} = (\hat{\mathbf{x}} - i\hat{\mathbf{y}})/\sqrt{2}$ are the left and right handed circular polarization vectors. Substituting this electric field in Eq. (5.5) provides the following polarization vectors for the left and right handed circular components

$$P_L = \varepsilon_0(A\left|E_L\right|^2 + (A+B)\left|E_R\right|^2)E_L, \tag{5.6}$$

$$P_R = \varepsilon_0(A\left|E_R\right|^2 + (A+B)\left|E_L\right|^2)E_R. \tag{5.7}$$

Substituting these polarizations in the nonlinear paraxial wave equation, Eq. (5.2), yields the following coupled nonlinear wave equations describing the evolution of both of the beam's circularly polarized components

$$\frac{\partial}{\partial z}E_L(\mathbf{r}) = \frac{i}{2k_0}\boldsymbol{\nabla}_\perp^2 E_L(\mathbf{r}) + \frac{i}{2k_0}\frac{k_0^2}{n_0^2}(A\left|E_L\right|^2 + (A+B)\left|E_R\right|^2)E_L, \tag{5.8}$$

$$\frac{\partial}{\partial z}E_R(\mathbf{r}) = \frac{i}{2k_0}\boldsymbol{\nabla}_\perp^2 E_R(\mathbf{r}) + \frac{i}{2k_0}\frac{k_0^2}{n_0^2}(A\left|E_R\right|^2 + (A+B)\left|E_L\right|^2)E_R. \tag{5.9}$$

These equations can adopt a more convenient form that accounts for parameters describing experimental conditions. To obtain this form, several quantities in these coupled nonlinear equations must be re-expressed in terms of others. First, spatial coordinates must be made dimensionless by normalizing them with respect to the beam's parameters. Namely, we express the equation in terms of the dimensionless cylindrical coordinates $(\varrho, \varphi, \zeta)$, where $\varrho = \rho/w_0$ is a dimensionless radial coordinate expressed in terms of the radial coordinate ρ and the beam's beam waist w_0, φ is the cylindrical azimuthal coordinate, and $\zeta = z/k_0 w_0^2$ is the dimensionless longitudinal coordinate. A and B can also be simplified based on the considered nonlinear response. In the publication on which this part of the chapter is based [52], we consider the propagation of an optical beam through rubidium atomic vapour. In this medium, nonlinearities arise from electronic responses which cause the A and B terms to be equal, i.e. $A = B = 6\chi^{(3)}$ [54]. Moreover, we need to replace any occurrences of $\chi^{(3)}$ by the nonlinear contribution to refractive index $n_2 I$, where $I = 2n_0\varepsilon_0 c\,|E|^2$ is the beam's intensity and $n_2 = 3\chi^{(3)}/4n_0^2\varepsilon_0 c$. Finally, we can express the electric field with respect to the incident power carried by the beam P_0, i.e. $|E|^2 \to P_0\,|E|^2/2n_0\varepsilon_0 c\pi w_0^2$. By accounting for these terms, the coupled nonlinear equations can be re-expressed as:

$$\frac{\partial}{\partial\zeta}E_L(\mathbf{r}) = \frac{i}{2}\boldsymbol{\nabla}_\perp^2 E_L(\mathbf{r}) + i\,\frac{2k_0^2 n_2 P_0}{n_0\pi}(|E_L|^2 + 2\,|E_R|^2)E_L, \tag{5.10}$$

$$\frac{\partial}{\partial\zeta}E_R(\mathbf{r}) = \frac{i}{2}\boldsymbol{\nabla}_\perp^2 E_R(\mathbf{r}) + i\,\frac{2k_0^2 n_2 P_0}{n_0\pi}(|E_R|^2 + 2\,|E_L|^2)E_R. \tag{5.11}$$

Furthermore, a saturation term can also be added when considering a saturable Kerr medium, i.e.,

$$\frac{\partial}{\partial\zeta}E_L(\mathbf{r}) = \frac{i}{2}\boldsymbol{\nabla}_\perp^2 E_L(\mathbf{r}) + i\,\frac{2k_0^2 n_2 P_0}{n_0\pi}\frac{|E_L|^2 + 2\,|E_R|^2}{1 + \alpha(|E_L|^2 + 2\,|E_R|^2)}E_L, \tag{5.12}$$

$$\frac{\partial}{\partial\zeta}E_R(\mathbf{r}) = \frac{i}{2}\boldsymbol{\nabla}_\perp^2 E_R(\mathbf{r}) + i\,\frac{2k_0^2 n_2 P_0}{n_0\pi}\frac{|E_R|^2 + 2\,|E_L|^2}{1 + \alpha(|E_R|^2 + 2\,|E_L|^2)}E_R. \tag{5.13}$$

where α is a saturation parameter. These coupled equations can be numerically solved to provide information pertaining to the nonlinear propagation dynamics of optical beams with a polarization structure, and how they compare with light beams that are only defined by a phase structure.

Polarization Shaping for Control of Nonlinear Propagation

Frédéric Bouchard,[1] Hugo Larocque,[1] Alison M. Yao,[2] Christopher Travis,[2] Israel De Leon,[1,3] Andrea Rubano,[4] Ebrahim Karimi,[1,5,*] Gian-Luca Oppo,[2] and Robert W. Boyd[1,6]

[1]The Max Planck Centre for Extreme and Quantum Photonics, Department of Physics, University of Ottawa, 25 Templeton, Ottawa, Ontario K1N 6N5, Canada
[2]SUPA and Department of Physics, University of Strathclyde, 107 Rottenrow, Glasgow G4 0NG, Scotland, United Kingdom
[3]School of Engineering and Sciences, Tecnológico de Monterrey, Monterrey, Nuevo Leon 64849, Mexico
[4]Dipartimento di Fisica, Università di Napoli Federico II, Complesso Universitario di Monte Sant'Angelo, via Cintia, 80126 Napoli, Italy
[5]Department of Physics, Institute for Advanced Studies in Basic Sciences, 45137-66731 Zanjan, Iran
[6]Institute of Optics, University of Rochester, Rochester, New York 14627, USA

(Received 15 June 2016; published 2 December 2016)

We study the nonlinear optical propagation of two different classes of light beams with space-varying polarization—radially symmetric vector beams and Poincaré beams with lemon and star topologies—in a rubidium vapor cell. Unlike Laguerre-Gauss and other types of beams that quickly experience instabilities, we observe that their propagation is not marked by beam breakup while still exhibiting traits such as nonlinear confinement and self-focusing. Our results suggest that, by tailoring the spatial structure of the polarization, the effects of nonlinear propagation can be effectively controlled. These findings provide a novel approach to transport high-power light beams in nonlinear media with controllable distortions to their spatial structure and polarization properties.

DOI: 10.1103/PhysRevLett.117.233903

Light beams that can propagate without a significant change to their spatial profile [1] are of interest for modern optical technologies and high-power laser systems. Self-trapped light filaments, or spatial solitons, are formed when their spreading due to linear diffraction is carefully balanced by a self-focusing (Kerr) nonlinearity that causes the beam to narrow. Because of their potential to carry an increased information content, there has been significant interest in the formation of spatial solitons carrying orbital angular momentum (OAM) [2–9]. The formation of such spatial structures has also been reported in a spinor quantum fluid [10]. OAM-carrying beams are characterized by an azimuthal phase dependence of the form $\exp(i\ell\varphi)$ [11], where the integer ℓ corresponds to the topological charge of the phase singularity present at the beam center (e.g., see [12] and references therein). Such beams include the Laguerre-Gauss (LG) modes [13], which comprise a complete set of solutions to the paraxial wave equation.

It is well known that, in $(2+1)$ dimensions, spatial solitons are unstable in homogeneous Kerr media [14]. One way to increase their stability is to use a saturable self-focusing medium to prevent the catastrophic collapse due to self-focusing. By using an intensity-dependent nonlinear refractive index n_2, it becomes possible to balance out the effects of self-focusing and diffraction. However, even in the case of saturable self-focusing media, it is known that optical beams carrying OAM will fragment into several solitons possessing particlelike attributes [3,15]. In particular, a scalar beam carrying an OAM value of ℓ is predicted to break up into 2ℓ daughter solitons [2,7].

In comparison with scalar ring solitons that carry a definite nonzero OAM, it has been suggested that stability can be increased by using two beams with opposite OAM to produce a beam with a net zero OAM [5,6,8,9]. For example, "necklace" (petal) beams, which consist of a scalar superposition of two modes with equal and opposite OAM, have been shown to exhibit quasistable propagation in a self-focusing medium, although they expand upon propagation [16]. For vectorial superpositions of beams carrying OAM, however, the resulting *vector solitons* have been shown both theoretically [3,6,9] and experimentally using nonlocal media [17] to exhibit quasistable propagation for much larger distances than the corresponding scalar vortex solitons.

Vector vortex beams are fully correlated solutions to the vector paraxial wave equation that have space-varying polarization distributions. Cylindrical vector beams are a subclass of vector beams with an axially symmetric polarization profile about the beam's propagation axis [18,19]. Examples include *radial*, *azimuthal,* and *spiral* polarization distributions. Another class of light beams with nonuniform polarization structures is that of full Poincaré beams [19,20]. These are of intrinsic interest, because they carry polarization singularities. Such beams typically consist of a superposition of two orthogonally polarized LG modes of different orbital angular momenta [19,20] and thus carry a net value of OAM.

In this Letter, we demonstrate, both experimentally and numerically, the stable propagation of space-varying polarized light beams in a saturable self-focusing nonlinear

0031-9007/16/117(23)/233903(5)

medium. More specifically, our study focuses on vector vortex and Poincaré beams traveling through rubidium vapor. We compare the intensity and polarization distributions of the beams at the entrance and exit of the nonlinear cell. This allows us to see how beam breakup is affected both by the net OAM of the beam and by its polarization distribution.

Theory.—Light beams with spatially inhomogeneous polarization distributions can be obtained by a superposition of two spatial transverse modes, E_1 and E_2, with orthogonal polarizations

$$\mathbf{E}(r,\varphi,z) = E_1(r,\varphi,z)\mathbf{e}_1 + E_2(r,\varphi,z)\mathbf{e}_2, \qquad (1)$$

where $\mathbf{e}_1$ and $\mathbf{e}_2$ are orthonormal polarization vectors and r, φ, and z are the cylindrical coordinates. Here we adopt the circular polarization basis, i.e., $\mathbf{e}_1 = \mathbf{e}_L$ and $\mathbf{e}_2 = \mathbf{e}_R$, and the LG basis for the spatial transverse modes [20]. If the two beams have equal but opposite OAM, the polarization of the beam varies along the azimuthal coordinate and, if the beams are equally weighted, spans the equator of the Poincaré sphere. These radially symmetric *vector vortex* beams [18] can have polarization distributions that are radial, azimuthal [see Figs. 1(a) and 1(b)], or spiral. If E_1 and E_2 carry a zero and a nonzero OAM value, respectively, the resulting full Poincaré beam [20] has a polarization that varies in both the angular and radial coordinates [19] and covers all polarization states on the Poincaré sphere [20]. The state of elliptic polarization varies with position [21], and polarization singularities occur at C points, where the azimuth is not defined and the polarization is circular [22], and along L lines, where the polarization is linear and its handedness is not defined [23]. C points can have three fundamental polarization topologies classified by the number of polarization lines that terminate at the singularity: These topologies are known as "star" (three lines), "lemon" (one line), and "monstar" (infinitely many, with three straight, lines) [21,24]. Examples of lemon and star topologies are shown in Figs. 1(c) and 1(d), respectively.

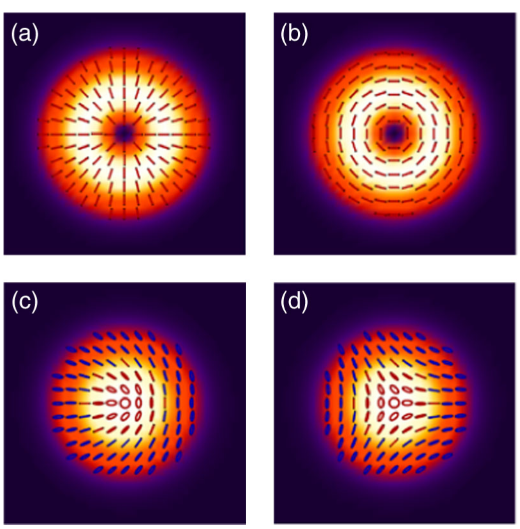

FIG. 1. (a) Radial and (b) azimuthal vector beams. (c) Lemon and (d) star Poincaré beams. Red (blue) ellipses correspond to left (right) circular polarization.

We simulate propagation through the medium using a $(2+1)$-dimensional nonlinear Schrödinger equation with a saturable self-focusing nonlinearity, derivable from the two-level model, under the slowly varying envelope and paraxial approximations and normalized to dimensionless quantities $\rho = r/w_0$ and $\zeta = z/(2z_R)$, where w_0 is the beam waist and z_R is the Rayleigh range of the beam [2,3,6]. As we are dealing with vector beams, our model consists of two coupled equations for oppositely circularly polarized beams that interact through the cross phase modulation term in a homogeneous medium [25]:

$$\begin{aligned}\frac{\partial E_1}{\partial \zeta} &= \frac{i}{2}\nabla_\perp^2 E_1 + i\mu \frac{|E_1|^2 + 2|E_2|^2}{1+\sigma(|E_1|^2 + 2|E_2|^2)}E_1,\\ \frac{\partial E_2}{\partial \zeta} &= \frac{i}{2}\nabla_\perp^2 E_2 + i\mu \frac{|E_2|^2 + 2|E_1|^2}{1+\sigma(|E_2|^2 + 2|E_1|^2)}E_2. \end{aligned} \qquad (2)$$

The parameters of importance are the nonlinear parameter μ and the saturation parameter σ, given by

$$\mu = \frac{2k_0^2 n_2 P_0}{3n_0}; \qquad \sigma = \frac{4P_0}{3I_{\mathrm{sat}} w_0^2}, \qquad (3)$$

where k_0 is the free-space wave number, n_0 and n_2 are the linear and nonlinear refractive indices ($n_2 > 0$ for self-focusing), I_{sat} is the saturation intensity, and P_0 is the power of the incident laser beam. In the simulations reported below, we have selected $\mu = 386$ and $\sigma = 51.7$ that reproduce the experimental configuration of the natural rubidium (Rb) cell. We performed numerical integrations of the propagation equations (2), using the split-step method with fast Fourier transforms and parameters corresponding to the experiments performed.

Experiment.—We use a spatially filtered, linearly polarized, tunable cw single-mode diode laser (Toptica DL pro 780, 760–790 nm) together with a set of half- and quarter-wave plates to generate a Gaussian beam with an arbitrary polarization state $\cos(\theta/2)\mathbf{e}_L + \exp(i\chi)\sin(\theta/2)\mathbf{e}_R$, where θ and χ are set by the orientations of the wave plates. This beam is converted into a space-varying polarized light beam using a q plate—a slab of patterned liquid crystal—that couples optical spin to OAM [26]. The *unitary* action of a q plate in the circular polarization basis is described by

$$\hat{\mathrm{U}}_q \cdot \begin{bmatrix}\mathbf{e}_L\\ \mathbf{e}_R\end{bmatrix} = \cos\left(\frac{\delta}{2}\right)\begin{bmatrix}\mathbf{e}_L\\ \mathbf{e}_R\end{bmatrix} + i\sin\left(\frac{\delta}{2}\right)\begin{bmatrix}\mathbf{e}_R e^{+2i(q\varphi+\alpha_0)}\\ \mathbf{e}_L e^{-2i(q\varphi+\alpha_0)}\end{bmatrix}, \qquad (4)$$

where q is a half-integer number corresponding to the topological charge of the liquid crystal pattern, α_0 is the

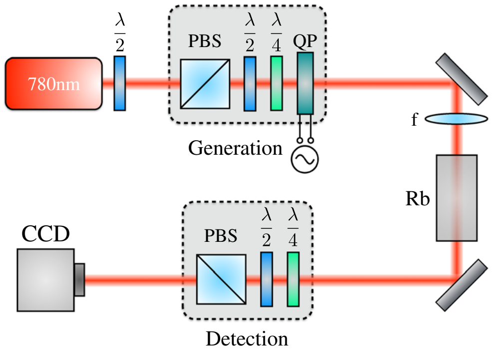

FIG. 2. Experimental setup. A cw wavelength-tunable (760–790 nm) Toptica diode laser is coupled to a polarization-maintaining single-mode optical fiber. The power of the laser beam is adjusted by means of a half-wave ($\lambda/2$) plate followed by a polarizing beam splitter (PBS) in order to reach the saturation threshold ($I_{\mathrm{sat}} = 5\ \mathrm{W\,cm^{-2}}$) for the D_2 resonance line of Rb. A combination of a $\lambda/2$ and a $\lambda/4$ plate is used to generate an arbitrary polarization state, which is then sent to a q plate (QP), with a topical charge of $q = \pm 1/2$, to generate vector vortex and Poincaré beams. This is then focused ($w_0 = 60\ \mu\mathrm{m}$) into a thermally controlled Rb atomic vapor cell by means of a lens ($f = 150$ mm). The transmitted beam is analyzed with a combination of a $\lambda/4$ plate, a $\lambda/2$ plate, and a PBS and attenuated using neutral density filters before being recorded by a CCD camera.

azimuthal orientation of the liquid crystal elements at $\varphi = 0$ (laboratory frame), and δ is the optical retardation of the q plate. The parameter δ can be experimentally adjusted by applying an electric field onto the plate in such a way that the resulting optical retardation corresponds to a half ($\delta = \pi$) or quarter ($\delta = \pi/2$) wavelength [27]. The generated beam is then focused by a 150-mm-focal-length lens into a 9-cm-long cell containing Rb atomic vapor. A detailed depiction of this experimental apparatus is provided in Fig. 2. The intensity of the incident beam and the temperature of the atomic vapor are set so that the medium exhibits saturable Kerr nonlinearities (powers in the vicinity of 7.44 mW and a temperature of 95 °C). In order to observe beam breakup of OAM-carrying beams, the laser's output wavelength was tuned near the D_2 transition line of Rb. Moreover, the laser was blue-detuned by less than 0.7 GHz from the $5S_{1/2}(F = 3) \to 5P_{3/2}(F = 4)$ hyperfine transition.

The beam exiting the Rb cell is then imaged using a lens with a focal length of 200 mm (not shown in the experimental setup) and its polarization distribution is reconstructed using polarization tomography. The tomography is performed using an appropriate sequence of a quarter-wave plate, a half-wave plate, a polarizer, and a spatially resolving detector (CCD camera) set at an exposure time of 0.1 s.

In order to generate vector vortex beams (radial, azimuthal, and spiral), a linearly polarized Gaussian beam is sent to a tuned ($\delta = \pi$) q plate of topological charge $q = 1/2$ [28]. Apart from a global phase, the generated beam will be given by $[\mathrm{LG}_{0,-1}(r,\varphi,z)\mathbf{e}_L + \exp(i\beta)\mathrm{LG}_{0,1}(r,\varphi,z)\mathbf{e}_R]/\sqrt{2}$, where $\beta \equiv 4\alpha_0$ depends on the orientation of the q plate with respect to the input polarization. The generated beams correspond to radial ($\beta = 0$), azimuthal ($\beta = \pi$), and spiral ($\beta = \pm\pi/2$) vector vortex beams. To generate the lemon and star Poincaré beams, a circularly polarized Gaussian beam is sent to a perfectly detuned ($\delta = \pi/2$) q plate with $q = 1/2$ and $q = -1/2$, respectively [29]. Here, $\beta = 2\alpha_0$ and does not affect the polarization topology but does cause a rotation in the polarization pattern. Thus, we choose $\beta = 0$, resulting in an output beam of the form $[\mathrm{LG}_{0,0}(r,\varphi,z)\mathbf{e}_L + \mathrm{LG}_{0,2q}(r,\varphi,z)\mathbf{e}_R]/\sqrt{2}$, again omitting any global phase factors. Note also that monstar topologies cannot be readily generated in the laboratory. This scheme allows us to switch between different structured light beams without altering their intensities.

Analysis.—It is well known that azimuthal modulational instabilities associated with the helical phase structure found in beams carrying OAM result in their filamentation as they propagate through saturating self-focusing media [2,3,6]. It has been shown, however, that the dominant low-frequency perturbations that typically disrupt ring solitons are inhibited by diffraction for vector solitons with no net OAM [6,9]. For strongly saturating media, stable counterrotating vortex pairs have also been predicted [9]. Here we confirm the inhibition of the azimuthal instability experimentally and numerically by propagating a beam of the form $\cos\gamma\mathrm{LG}_{0,-1}(r,\varphi,z)\mathbf{e}_L + \sin\gamma\exp(i\beta)\mathrm{LG}_{0,1}(r,\varphi,z)\mathbf{e}_R$ through a self-focusing medium. When $\gamma = 0$ or $\pi/2$, the beam is a scalar LG mode defined by $\ell = -1$ or $+1$ with left- or right-hand circular polarization, respectively. For $\gamma = \pi/4$ we have a vector vortex beam with linear polarization and for $\gamma = \pi/8$ and $3\pi/8$, a vector vortex beam of left- and right-hand elliptical polarization, respectively, following the topology of the vector beam with $\gamma = \pi/4$. Note that each beam has the same total intensity.

A comparison of the experimental results with the simulations based on Eqs. (2) is shown in Fig. 3 for a vector beam defined by $\beta = -\pi/2$. From our results, we can see that the nonlinearity counterbalances diffraction up until the point at which the beams fragment. As expected, we see that the scalar OAM-carrying beams ($\gamma = 0$, $\pi/2$) are starting to break up at the exit of the nonlinear cell. The vector beam ($\gamma = \pi/4$), on the other hand, seems almost unperturbed, in terms of both its amplitude and polarization distribution. Indeed, we can find numerically that the fragmentation point occurs much later for vector beams (~13.5 cm) than for scalar beams (~9 cm) [30,31] and that the vector beam and its components break up at the same point. For the elliptically polarized vector beams ($\gamma = \pi/8$, $3\pi/8$), the stability length is between the cases of scalar and vector vortex beams. In this case, the effect of the nonlinear propagation is also evident in the local rotation of the polarization: The initial spiral distribution has now become

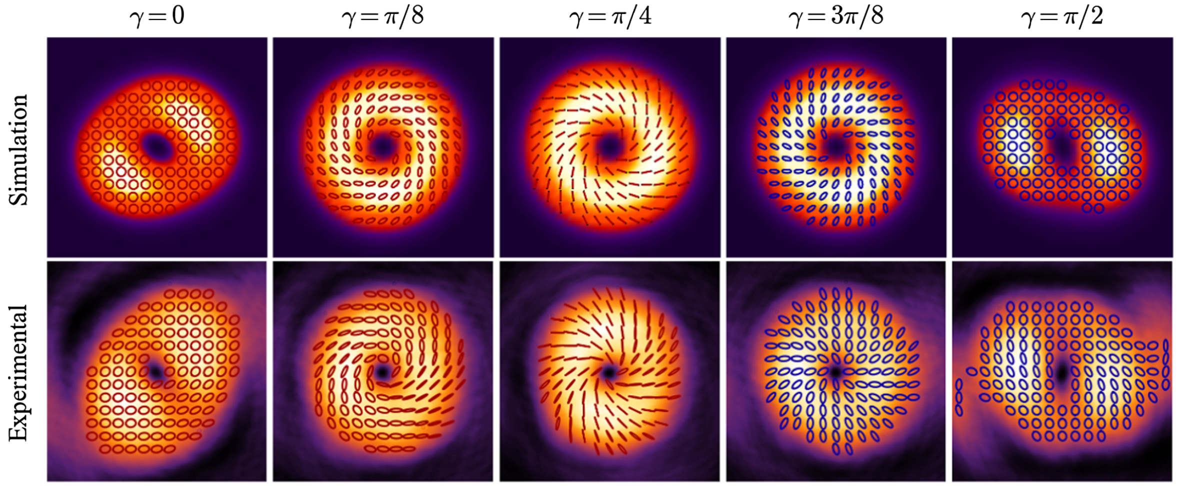

FIG. 3. Simulated (upper row) and experimentally reconstructed (lower row) intensity and polarization distributions of scalar and vector superposition beams after propagating through the Rb cell. The incident beams are $\cos(\gamma)\mathrm{LG}_{0,-1}(r,\varphi,z)\mathbf{e}_L+\sin(\gamma)\exp(i\beta)\mathrm{LG}_{0,1}(r,\varphi,z)\mathbf{e}_R$, with $\beta=-\pi/2$ and γ specified at the top. Red (blue) ellipses correspond to left (right) circular polarization. Note that for the cases of uniformly polarized input beams ($\gamma=0$ and $\pi/2$) the beam shows a significant distortion at the output of the medium. The spiral vector beam ($\gamma=\pi/4$) shows essentially no distortion in the intensity distribution or polarization. The elliptically polarized input beams ($\gamma=\pi/8$ and $3\pi/8$) show some polarization distortion but no distortion of the intensity distribution. Minor differences in polarization rotations are mainly due to experimental imperfections.

almost azimuthal or radial, respectively (see Fig. 1). This suggests that vector beams with equally weighted orthogonally polarized components, regardless of their specific topology [31], allow for greater control over the effects of nonlinear propagation. In spite of the approximations used in the derivation of Eqs. (2), small differences in polarization distributions between the experiment and the numerical simulation are really evident only in the biased mode cases of $\gamma=\pi/8, 3\pi/8$, thus demonstrating the robustness of the vector vortex beam ($\gamma=\pi/4$).

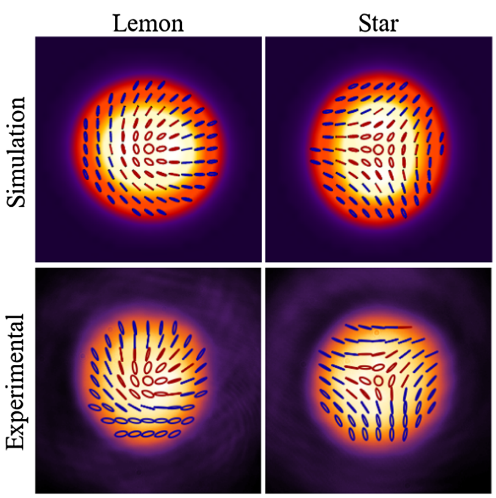

FIG. 4. Intensity and polarization distributions of lemon and star topologies after propagating through the Rb cell, numerical (upper row) and experimental (lower row). Red (blue) ellipses correspond to left (right) circular polarization. Note that these beams are far more stable than the uniformly polarized beams of the left- and rightmost columns in Fig. 3. Minor differences in polarization rotations are mainly due to experimental imperfections.

It has been proposed that the increase in stability seen in vector beams is because they carry no net OAM [6,8,9]. To test this hypothesis, we repeated our analysis using Poincaré beams having lemon and star topologies which do possess a net OAM. The experimental and numerical results are shown in Fig. 4, where we have plotted the intensity and the polarization distributions for the lemon and star topologies after propagating through the Rb cell. These results again show that beam breakup has been inhibited when compared to scalar OAM-carrying beams (see the left- and rightmost panels in Fig. 3). This result demonstrates that the increased stability is due to the orthogonality of the constituent modes, which is responsible for the polarization shaping, and not simply due to a net OAM of zero. We emphasize that both vector vortex and Poincaré beams display increased stability with respect to that of a scalar beam [31]. In Fig. 4, we show that the polarization distributions of the Poincaré beams, although rotated by the Gouy phase [20], remain unaltered after nonlinear propagation (as in the case of vector vortex beams for $\gamma=\pi/4$) and even preserve the numbers and types of polarization singularities.

Conclusion.—We have compared the propagation of scalar OAM-carrying beams with two different classes of beams with nonuniform transverse polarization distributions in a saturable self-focusing nonlinear medium of Rb vapor. With respect to scalar vortex beams (LG modes), we found that beam breakup can be inhibited, while nonlinear confinement, self-focusing, and polarization distributions are not altered for specific cases of nonuniform spatial polarization, both with and without net OAM. This finding suggests that the spatial structure of the polarization plays an important role in preventing beam fragmentation. These findings provide a novel approach to transport high-power light beams in nonlinear media with controllable distortions to their spatial structure and polarization properties.

F. B., H. L., E. K., and R. W. B. acknowledge the support of the Canada Excellence Research Chairs (CERC) program. A. R. acknowledges funding from the European Union (FP7-PEOPLE-2012-CIG, PCIG12-GA-2012-326499-FOXIDUET). E. K. acknowledges the support of the Canada Research Chairs (CRC) program and Canada Foundation for Innovation (CFI).

*ekarimi@uottawa.ca

[1] R. Y. Chiao, E. Garmire, and C. H. Townes, Phys. Rev. Lett. **13**, 479 (1964).
[2] W. J. Firth and D. V. Skryabin, Phys. Rev. Lett. **79**, 2450 (1997).
[3] A. S. Desyatnikov and Y. S. Kivshar, Phys. Rev. Lett. **87**, 033901 (2001).
[4] Z. H. Musslimani, M. Soljačić, M. Segev, and D. N. Christodoulides, Phys. Rev. E **63**, 066608 (2001).
[5] M. Soljačić and M. Segev, Phys. Rev. Lett. **86**, 420 (2001).
[6] M. S. Bigelow, Q-Han Park, and R. W. Boyd, Phys. Rev. E **66**, 046631 (2002).
[7] M. S. Bigelow, P. Zerom, and R. W. Boyd, Phys. Rev. Lett. **92**, 083902 (2004).
[8] F. Ye, J. Wang, L. Dong, and Y. P. Li, Opt. Commun. **230**, 219 (2004).
[9] A. S. Desyatnikov, D. Mihalache, D. Mazilu, B. A. Malomed, and F. Lederer, Phys. Lett. A **364**, 231 (2007).
[10] L. Dominici, G. Dagvadorj, J. M. Fellows, D. Ballarini, M. De Giorgi, F. M. Marchetti, B. Piccirillo, L. Marrucci, A. Bramati, G. Gigli, M. H. Szymańska, and D. Sanvitto, Sci. Adv. **1**, e1500807 (2015).
[11] L. Allen, M. W. Beijersbergen, R. J. C. Spreeuw, and J. P. Woerdman, Phys. Rev. A **45**, 8185 (1992).
[12] A. M. Yao and M. J. Padgett, Adv. Opt. Photonics **3**, 161 (2011).
[13] S. M. Barnett and R. Zambrini, in *Quantum Imaging*, edited by K. I. Kolobov (Springer, Singapore, 2007), p. 284.
[14] J. J. Rasmussen and K. Rypdal, Phys. Scr. **33**, 481 (1986).
[15] B. A. Malomed, D. Mihalache, F. Wise, and L. Torner, J. Opt. B **7**, R53 (2005).
[16] M. Soljačić, S. Sears, and M. Segev, Phys. Rev. Lett. **81**, 4851 (1998).
[17] Y. V. Izdebskaya, J. Rebling, A. S. Desyatnikov, and Y. S. Kivshar, Opt. Lett. **37**, 767 (2012).
[18] Q. Zhan, Adv. Opt. Photonics **1**, 1 (2009).
[19] E. J. Galvez, S. Khadka, W. H. Schubert, and S. Nomoto, Appl. Opt. **51**, 2925 (2012).
[20] A. M. Beckley, T. G. Brown, and M. A. Alonso, Opt. Express **18**, 10777 (2010).
[21] M. R. Dennis, K. O'Holleran, and M. J. Padgett, Prog. Opt. **53**, 293 (2009).
[22] J. F. Nye, Proc. R. Soc. A **389**, 279 (1983).
[23] J. F. Nye, Proc. R. Soc. A **387**, 105 (1983).
[24] J. F. Nye, *Natural Focusing and Fine Structure of Light: Caustics and Wave Dislocations* (CRC Press, Boca Raton, FL, 1999).
[25] G. P. Agrawal, *Nonlinear Fiber Optics*, fourth ed. (Academic, New York, 2007).
[26] L. Marrucci, C. Manzo, and D. Paparo, Phys. Rev. Lett. **96**, 163905 (2006).
[27] S. Slussarenko, A. Murauski, T. Du, V. Chigrinov, L. Marrucci, and E. Santamato, Opt. Express **19**, 4085 (2011).
[28] F. Cardano, E. Karimi, S. Slussarenko, L. Marrucci, C. de Lisio, and E. Santamato, Appl. Opt. **51**, C1 (2012).
[29] F. Cardano, E. Karimi, L. Marrucci, C. de Lisio, and E. Santamato, Opt. Express **21**, 8815 (2013).
[30] Note that, although we observe inhibited azimuthal instabilities, the waist of the vector vortex beam oscillates before breakup as shown in Ref. [31] and at difference from the theoretical analysis of Refs. [6,9].
[31] See Supplemental Material at http://link.aps.org/supplemental/10.1103/PhysRevLett.117.233903 for further details.

5.3 Twisted neutrons

The ability to twist the wavefronts of photon and electron waves has recently motivated studies attempting to twist the wavefunction of other types of particles. In particular, there have been experiments claiming the ability to impart OAM onto neutron waves [60]. However, neutrons are not defined by the properties that make OAM-carrying photons and electrons so useful in applications such as quantum cryptography and materials science. For this reason, there currently lacks a clear picture of potential applications where twisted neutrons could potentially be useful.

The second publication on which this chapter is based seeks to provide such an application. Namely, it suggests that shaping the wavefunction of neutrons could provide additional means of investigating their subatomic structure [53].

5.3.1 Neutron charge densities

Neutrons are subatomic particles classified as baryons. Its three quarks consists of an up quark and two down quarks, which respectively have charges of $+2e/3$ and $-e/3$, where e is the elementary charges. Due to this composition, neutrons are neutrally charged. However, the configuration that these quarks adopt adds a certain level of structure to the neutron such as an internal charge density. Information pertaining to this quantity can be obtained through the the use of theoretical models [61, 62], or through experimental measurements of a neutron's form factors [63, 64, 65].

As seen in chapter 4, the probabilistic nature of a particle's wavefunction causes it to be defined by a probability density and a probability current density that can manifest themselves as electric charge and current densities when the particle consists of a charged entity. For wavefunctions consisting of particles defined by an internal charge density such as neutrons, the resulting electric densities can be seen as convolutions of the wave's probability densities with the particle's internal charge density, i.e.

$$\rho_\psi(\mathbf{r}) = \int \rho(\mathbf{r}' - \mathbf{r})\, |\psi(\mathbf{r}')|^2 \, d^3\mathbf{r}' \tag{5.14}$$

$$\mathbf{J}_\psi(\mathbf{r}) = \int \rho(\mathbf{r}' - \mathbf{r})\, \mathbf{j}(\mathbf{r}') \, d^3\mathbf{r}' \tag{5.15}$$

where ρ_ψ and $\mathbf{J}_\psi$ are electric charge and current densities that arise from a particle defined by an internal charge density $\rho(\mathbf{r})$ and a wavefunction ψ. The probability density and the probability current density of the wavefunction are respectively denoted by $|\psi(\mathbf{r})|^2$ and $\mathbf{j}(\mathbf{r})$.

5.3.2 Multipole expansion

To gain insight on the electromagnetic properties of structured neutrons, the electromagnetic potential $\Phi(\mathbf{r})$ and $\mathbf{A}(\mathbf{r})$ attributed to the densities of Eqs. (5.14,5.15) can be expanded in terms of their multipole components [66], i.e.

$$\Phi(\mathbf{r}) = \frac{1}{\varepsilon_0}\sum_{l=0}^{\infty}\sum_{m=-l}^{l}\frac{1}{2l+1}q^{\star}_{lm}\frac{Y_{lm}(\theta,\varphi)}{r^{l+1}}, \tag{5.16}$$

$$\mathbf{A}(\mathbf{r}) = \mu_0\sum_{l=0}^{\infty}\sum_{m=-l}^{l}\frac{1}{2l+1}i^{\star}_{lm}\frac{Y_{lm}(\theta,\varphi)}{r^{l+1}}, \tag{5.17}$$

where μ_0 is the permeability of free space, (r,θ,φ) are the spherical coordinates, $Y_{lm}(\theta,\varphi)$ are the spherical harmonics, and $q^{\star}_{lm}$ and $i^{\star}_{lm}$ are the electric and magnetic multipole moment expansion coefficients. These moments can be found from the electric densities attributed to the potentials, i.e.

$$q^{\star}_{lm} = \int Y^{*}_{lm}(\theta',\varphi')r'^{l}\rho_{\psi}(\mathbf{r}')d^3\mathbf{r}', \tag{5.18}$$

$$i^{\star}_{lm} = \int Y^{*}_{lm}(\theta',\varphi')r'^{l}\mathbf{J}_{\psi}(\mathbf{r}')d^3\mathbf{r}'. \tag{5.19}$$

This approach provides a way to analyze the electromagnetic properties of free neutrons with twisted wavefunctions. These properties depend both on the neutron's wavefunction and its internal charge density. Given the extensive knowledge surrounding the mathematical formulation of twisted wavefunctions, these properties could be used to provide more accurate information on the internal structure of neutrons.

Twisting neutrons may reveal their internal structure

To the Editor — According to quantum mechanics, matter can be described by a wavefunction that can be modified, just like a wave, through processes such as interference. Under certain conditions, specific forms of interference can result in the formation of a vortex. Vortices are defined by some form of coiling motion around a stagnation point. In the case of matter waves, this coiling motion is attributed to the probability density associated with the wavefunction — that is, its probability density current[1]. Within a quantum context, this motion often translates to a wave with twisted wavefronts that describes a quantized form of azimuthal motion known as orbital angular momentum (OAM).

Electromagnetic or optical waves are now well-known examples of waves carrying OAM[2], and their use has been explored in several fields of modern science such as microscopy, optical tweezing and communications[3]. Similarities between the equations describing optical waves and the wavefunction of a free particle[1,3] have also led to the generation of OAM-carrying matter waves, especially electron waves[4,5]. In particular, the interest surrounding these 'twisted' electrons arises from the electron's charge, which, in conjunction with the wave's coiling motion, causes them to form loops of electrical current characterized by magnetic properties. Due to these properties, OAM-carrying electrons are now starting to find applications as nanoscale magnetic probes for characterizing materials[3,5].

Prospective applications of OAM-carrying particles have recently been discussed at this year's International Conference on Optical Angular Momentum (ICOAM) in Capri, Italy. Some of the proposed applications are based on more massive and non-elementary particles such as neutrons. In fact, a method to generate OAM-carrying neutron waves has recently been reported[6]. However, these neutron waves are not as coherent as optical waves and, unlike electrons, they do not carry a net charge. These properties suggest that neutrons would perform poorly in applications relying on OAM-carrying photons or electrons. On consideration of these factors, one might wonder whether neutrons or other OAM-carrying particles have any distinct properties that would make it possible to take advantage of their OAM in modern science. Interesting proposals have been put forward, one of them suggesting that shaping the wavefunction of a particle could increase its lifetime[7]. We are of the opinion that twisted neutron waves can additionally be used to provide information pertaining to their subatomic structure.

Unlike photons and electrons, neutrons are not elementary particles. More specifically, they consist of one up quark and two down quarks, which have different colours, bound together by the strong force, and whose charges add up to zero. This compound structure can to some extent complicate the formalism describing their physical states. For instance, for a free neutron, this internal structure manifests itself as a non-zero transverse charge density that must usually be obtained through the use of theoretical models with various fitting parameters[8,9]. This approach, however, often yields charge densities that vary from one model to another due to the different assumptions made concerning the neutron's internal structure. For this reason, information regarding this quantity must often be extracted by means of experimental methods — typically scattering experiments[10]. As shown in Fig. 1a, this experimental approach reveals that neutrons are negatively charged at their centre and have a transverse charge

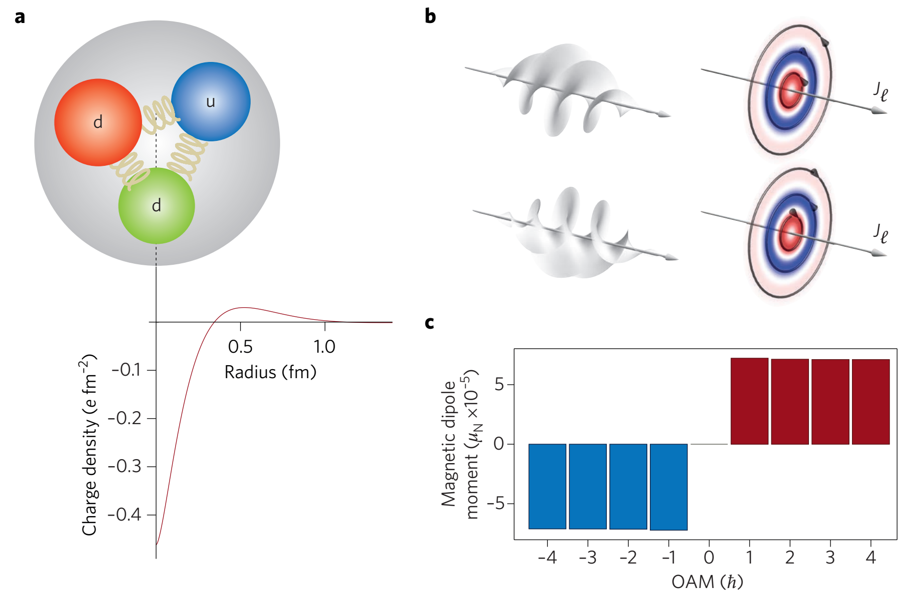

Figure 1 | Charge and current densities of OAM-carrying neutrons. **a**, Schematic of the quark composition of the neutron and the experimentally observed neutron's transverse charge density. **b**, Wavefronts of neutron wavepackets carrying ±2ħ units of OAM along with the associated transverse charge distributions, displayed in red and blue colours, and the direction of the resulting current density, represented by black arrows. Red represents a positive charge density while blue represents a negative one. **c**, Magnetic dipole moment of OAM-carrying neutron wavepackets resulting from the currents shown in **b** expressed in terms of the nuclear magneton μ_N for a neutron wavepacket with a beam waist of 20 fm.

density that varies between positive and negative values. The amplitude of these oscillations decreases as radial distance increases.

When a free neutron wave is imparted with OAM, it acquires a doughnut-shaped transverse profile along with a form of azimuthal motion. In conjunction with the neutron's internal charge distribution, we predict the appearance of OAM-dependent charge and current distributions, as shown in Fig. 1b. These transverse charge and current distributions make OAM-carrying neutrons exhibit several interesting electromagnetic properties.

The charge distribution resulting from the addition of OAM is directly determined by the doughnut-shaped profile of OAM-carrying waves. For regular (non-shaped) neutrons, which are modelled as Gaussian waves that do not carry OAM, the neutron wave's charge distribution directly corresponds to that of the neutron scaled to the relative (coherent) size of the beam. Unlike waves with a Gaussian transverse profile, an OAM-carrying wave is brightest at a certain radial distance from its centre — where the beam holds the negative charge attributed to the centre of the neutron. As we move away from this region, the outer charge distribution of the neutron starts to be more noticeable. Interestingly, the dominant terms describing the electric field at more distant regions have no dependence on the OAM carried by the neutron and depend solely on the neutron's internal charge density.

The current density of the neutron wave comes from its charge distribution experiencing a form of azimuthal motion. In the case of a Gaussian neutron wave, in the absence of OAM there will be no current. However, for OAM-carrying neutrons, the azimuthal motion of its charge distribution ultimately amounts to a sequence of loops of current whose direction alternates from loop to loop. Surprisingly, this alternation does not completely cancel out the magnetic fields that the current generates, resulting in a net magnetic field for OAM-carrying neutrons, as shown in Fig. 1c. Unlike particles that carry a net charge, such as electrons[1,3] or protons, the magnetic field of an OAM-carrying neutron wave does not increase with its OAM, as it gets quickly washed away when the transverse extent of the neutron wave becomes much greater than that of its internal charge density.

The neutron wave's OAM-dependent charge density could prospectively provide new means for probing the internal charge density of neutrons in scattering experiments, which rely on bombarding neutrons with charged or magnetized particles. Because these particles are scattered off the neutrons in a way that is determined by the neutron's internal charge and current densities, imparting OAM on neutrons could provide additional information on the neutron's internal structure by observing how it influences the outcome of the scattering experiment.

Our analysis and its applications can potentially be extended to other types of OAM-carrying free particles with non-trivial internal charge densities, including atoms. In particular, it could motivate the development of methods that can more efficiently characterize atomic and nuclear structure. However, the study of the interaction between such particles and external fields might be complicated by the type of interaction that binds the particle's constituents. ❒

References

1. Bliokh, K. Y., Bliokh, Y. P., Savel'ev, S. & Nori, F. *Phys. Rev. Lett.* **99,** 190404 (2007).
2. Allen, L., Beijersbergen, M. W., Spreeuw, R. J. C. & Woerdman, J. P. *Phys. Rev. A* **45,** 8185–8189 (1992).
3. Harris, J. *et al. Nat. Phys.* **11,** 629–634 (2015).
4. Uchida, M. & Tonomura, A. *Nature* **464,** 737–739 (2010).
5. Verbeeck, J., Tian, H. & Schattschneider, P. *Nature* **467,** 301–304 (2010).
6. Clark, C. W. *et al. Nature* **525,** 504–506 (2015).
7. Kaminer, I., Nemirovsky, J., Rechtsman, M., Bekenstein, R. & Segev, M. *Nat. Phys.* **11,** 261–267 (2015).
8. Isgur, N., Karl, G. & Sprung, D. W. L. *Phys. Rev. D* **23,** 163–164 (1981).
9. Thomas, A. W., Théberge, S. & Miller, G. A. *Phys. Rev. D* **24,** 216–229 (1981).
10. Miller, G. A. *Phys. Rev. Lett.* **99,** 112001 (2007).

Hugo Larocque[1], Ido Kaminer[2], Vincenzo Grillo[3], Robert W. Boyd[1] and Ebrahim Karimi[1]*
[1]Department of Physics, University of Ottawa, 25 Templeton Street, Ottawa, Ontario K1N 6N5, Canada. [2]Faculty of Electrical Engineering, Technion — Israel Institute of Technology, Haifa 32000, Israel. [3]CNR-Istituto Nanoscienze, Centro S3, Via G Campi 213/a, I-41125 Modena, Italy.
*e-mail: ekarimi@uottawa.ca

Chapter 6

Optical polarization knots

In the previous chapters, several means of analyzing the topological features of structured waves were provided. These features primarily consisted of the presence of singularities with varying topological charges in the examined wavefields. Given its importance in numerous applications, most of these methods focused on measuring a wave's OAM which consists of a quantity associated with the presence of a phase singularity at the wave's centre.

This chapter focuses on the generation and the characterization of optical waves defined by more complex topological structures. In particular, it examines beams with polarization singularities that form knots upon free-space propagation.

6.1 Knotted fields

Mathematical fields can be defined by threaded regions forming closed looped trajectories. The nature of these regions can vary from field to field. For instance, in vector fields, these closed regions can be formed by flow lines [67]. In complex fields, they can be formed by singularities in the field's phase [13]. Under certain circumstances, these closed loops consist of rather complex and rich topological structures. The complexity of these looped trajectories is often manifested through a series of crossings in three dimensional space, thus causing such loops to essentially adopt knotted structures as opposed to trivial ones. Such concepts form the basis of knot theory, a field of mathematics studying the topological features of knots [68].

In addition to the knot itself, knots are also defined by a set of oriented surfaces whose boundaries and intersection consist of the knot. These surfaces are known as

Seifert surfaces and their topological features are as rich, if not richer, than what can be solely extracted from the knot's three-dimensional trajectory. For instance, these surfaces can enclose critical points resembling diabolos whose numbers can be used to determine whether or not a knot is fibered [69, 70].

The Seifert surfaces of knots formed by a field's phase singularities can be readily observed in the field itself. Namely, these surfaces consist of the field's phase sheets, i.e. regions defined by a constant phase that form surfaces in three-dimensional space. This correspondence has motivated the development of several mathematical studies providing means of constructing complex fields with knotted singularities [13, 69, 70]. Such a field in which a trefoil knot is formed is shown in Fig. 6.1. Its field consists of a complex polynomial whose formulation is based on the work performed in [13].

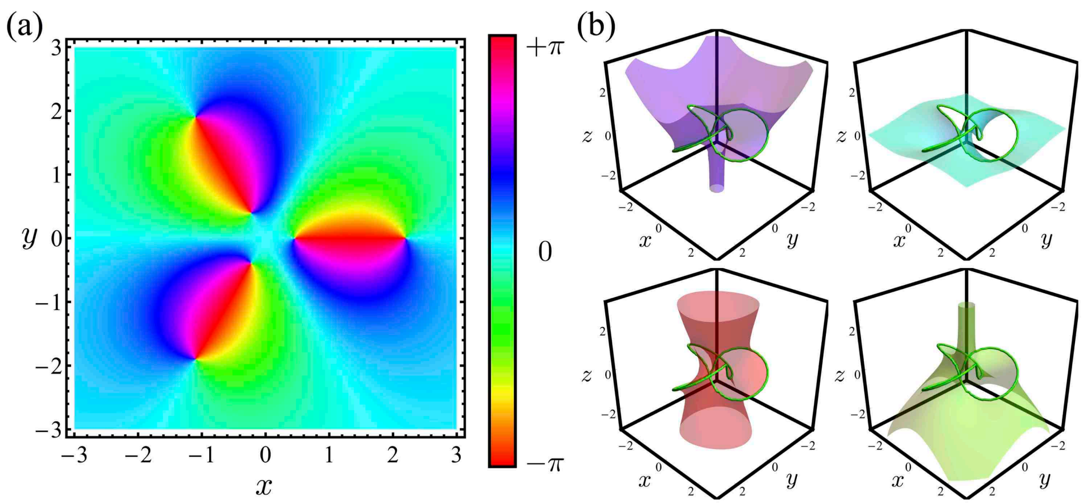

Figure 6.1: **Knotted trefoil field**. (a) The field's phase profile at the $z = 0$ plane. (b) The field's three dimensional phase sheets attributed to phases of $\pm\pi$, $-\pi/2$, 0, and $\pi/2$. Its intersections consist of phase singularities forming a trefoil knot shown in green.

6.1.1 Knotted optical singularities

As introduced in chapter 2, the optical singularities of certain forms of structured light can experience exotic dynamics such as linked or knotted trajectories as shown theoretically in [11] and experimentally in [12, 71, 13]. The success of these works has led to several theoretical endavours exploring the construct of complex fields whose phase vortices form various types of knots [69, 70], hence the motivation for experimental implementations of these structures. However, only a certain class of knots known as torus knots, i.e., knots that lie on the surface of a torus, were able to be generated in optical fields [13]. Moreover, the technical challenge of fully characterizing knotted optical fields has also prevented the full reconstruction of their topological structure. Experimental realizations of optical knots have also been uniquely confined to optical fields carrying phase vortices in spite of the fact that optical fields can also be defined by polarization singularities associated with the vectorial nature of light [8, 9].

6.2 Generating optical polarization knots

The purpose of this chapter is to introduce a method allowing for the generation and the characterization of optical waves carrying knotted optical polarization singularities. In particular, it studies the propagation of beams with knotted C-point polarization singularities. These polarization knots could prospectively be of use in studies pertaining to knotted dynamics in physical systems that are sensitive to optical polarization such as nonlinear media [52]. The physical properties of these optical structures along with the sensitivity of the experimental apparatus used to generate them also allows for the creation of more complex knots, such as figure-eight knots, that are harder to produce than torus knots.

6.2.1 Experimental apparatus

The generation scheme for optical polarization knots presented here consists of coherently superposing two circularly polarized light beams of opposite handedness. The relative phase and intensity between these two beams defines the resulting beam's transverse polarization pattern, which is characterized by the ellipticity and the orientation of the polarization ellipses forming the beam. In particular, the relative spatial intensity profiles of both circular polarization components define the ellipticity profile of the resulting beam. Likewise, the relative spatial phase profiles of both circular components determine the polarization orientation profile. Therefore, beams that carry C-points can readily be produced by superposing a circularly polarized beam carrying phase singularities with an oppositely polarized beam that has a smooth phase profile. Furthermore, when this profile is perfectly uniform, the polarization orientation distribution of the total beam is uniquely determined by the phase of the other component. This concept is illustrated in Fig. 6.2.

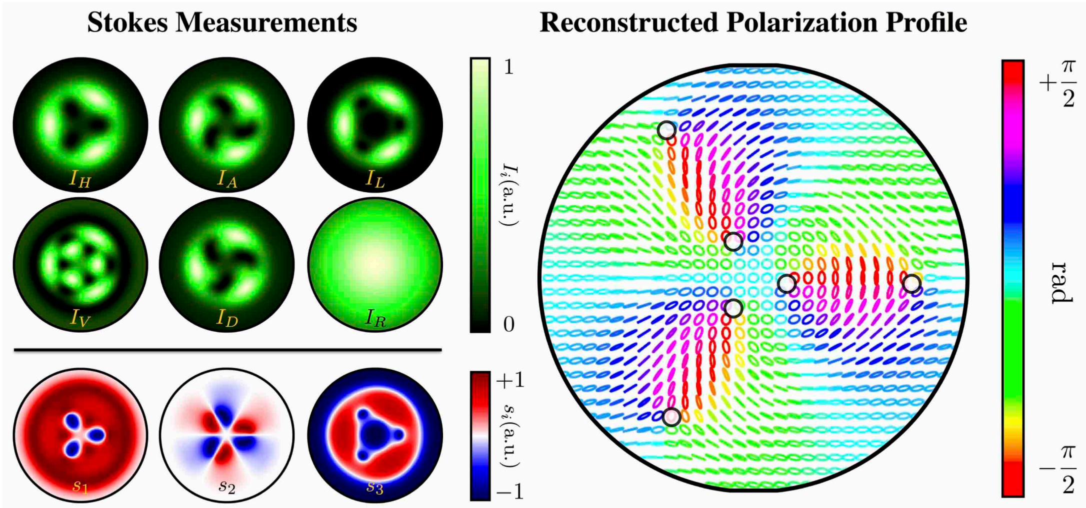

Figure 6.2: **Tomographic reconstruction of an optical polarization knot's polarization profile**. Intensity measurements of the horizontal (I_H), vertical (I_V), anti-diagonal (I_A), diagonal (I_D), left (I_L), and right (I_R) polarization components of the beam can be used to calculate its reduced Stokes parameters s_1, s_2, and s_3. With these quantities, the beam's transverse polarization profile can be reconstructed as shown above. C-points in the above polarization plots are highlighted and polarization ellipses are coloured based on their orientation.

The polarization pattern resulting from the addition of these two beams can be reconstructed by means of polarization tomography measurements to obtain the beam's reduced Stokes parameters $s^{i,j}$. Namely, these parameters can be obtained by a set of projective transverse polarization measurements that include $s_1^{i,j} = (I_H^{i,j} - I_V^{i,j})/(I_H^{i,j} + I_V^{i,j})$, $s_2^{i,j} = (I_A^{i,j} - I_D^{i,j})/(I_A^{i,j} + I_D^{i,j})$ and $s_3^{i,j} = (I_L^{i,j} - I_R^{i,j})/(I_L^{i,j} + I_R^{i,j})$. Here $I_\Pi^{i,j}$ is the transverse intensity associated with a polarization state $\Pi = \{H, V, A, D, L, R\}$ at the transverse position (i,j) and $H, V, A, D, L,$ and R label the horizontal, vertical, anti-diagonal, diagonal, left-handed circular and right-handed circular polarization states, respectively. From these parameters, information pertaining to the orientation and the ellipticity of the polarization ellipse at a specific position can be obtained from the relations $2\,\psi = \arctan{(s_2/s_1)}$ and $2\,\chi = \arctan s_3/(s_1^2 + s_2^2)^{1/2}$, where ψ and χ represent orientation and ellipticity, respectively.

The core of our method to generate optical polarization knots relies on the above superposition principles. As shown in Fig. 6.3, by means of a folded Sagnac interferometer [72, 73], we can produce a beam defined by distinct opposite circular polarizations, one of which defined by phase vortices that experience knotted trajec-

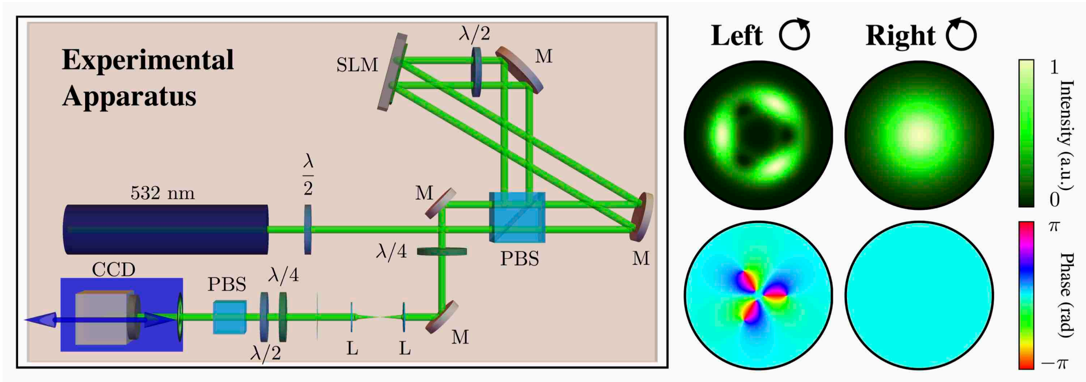

Figure 6.3: **Experimental apparatus for generating optical polarization knots**. A 532 nm linearly polarized laser beam goes through a half-wave plate ($\lambda/2$) that balances the weights of the beam's horizontal and vertical polarization components. These components are then separated by a polarizing beam splitter (PBS), causing them to propagate inside a folded Sagnac interferometer where their intensity and phase profiles are independently modified with a spatial light modulator (SLM). The two modulated components then exit the interferometer and go through a quarter-wave plate ($\lambda/4$) which converts their polarization to left- and right-handed circular states. The beam is then imaged onto a CCD camera in order to examine its propagation. Individual projective polarization measurements are then taken by means of a combination of a quarter-wave plate, a half-wave plate, and a PBS, thus allowing the reconstruction of the beam's polarization profile. Figure legend: lens (L), mirror (M).

tories upon propagation, and the other consisting of a conventional Gaussian beam with a beam waist that is sufficiently large to match the transverse extent of the knotted component. The beam resulting from this superposition therefore consists of a space-varying polarized light beam with C-point singularities that undergo knotted trajectories upon propagation. Using polarization tomography, the beam's polarization orientation profile can be reconstructed, thus revealing the position of its C-points.

Though this technique effectively produces knotted polarization singularities, it can also be perceived as a more accurate way of probing the dynamics of knotted phase singularities by means of polarimetry. More specifically, traditional ways of measuring the phase profile of optical structures with phase vortices, such as interferometry, are often complicated by the varying degree of intensity of the beam's transverse profile. While regions with a smooth phase usually have a high intensity, regions in the proximity of phase vortices are much darker due to the presence of intensity nulls on the vortices themselves. Therefore, getting accurate phase information in the vicinity of phase vortices usually involves increasing the employed detector's exposure time, which in the process saturates intensity measurements in other regions of the beams. This procedure usually prevents an accurate global characterization of the beam's phase structure. The accuracy of the process of converting phase singularities to polarization singularities and characterizing them with polarization tomography relies on the presence of oppositely polarized light in the dark regions enclosing the original phase singularities. This feature thus causes measurements performed in the proximity of the examined C-points to be smoother and to have a higher contrast than what could be obtained from measurements relying on traditional interferometry to examine phase singularities.

6.3 Reconstructing the knots' structures

The fact that the above method provides an accurate rendering of a knotted field's structure allows its use for providing additional information surrounding the knot's topology. One of the important traits that define knots are their Seifert surfaces. These surfaces are topological structures that are bounded by their knot and whose shapes can also be heavily affected by the knot's topological properties such as its genus or the presence of fibrations [69, 70]. The advantage of examining a knot's Seifert surfaces over its trajectory to gain insight on its topological traits arises from the fact that these traits often manifest themselves more clearly in the surfaces. For knots that consist of vortices in a complex field, Seifert surfaces directly correspond to three-dimensional regions defined by a constant phase. In the case of our polarization knots, these surfaces are attributed to regions of constant polarization orientation. To illustrate the interplay between these entities, an integrative depiction of a trefoil knot's structure is provided in Fig. 6.4 where the knot, one of its Seifert surfaces, and cross-sectional images of the knot's polarization orientation profile are shown.

The structural components shown in Fig. 6.4 are reconstructed by means of a series of polarimetric measurements of the beam's reduced Stokes parameters at various transverse planes. With these measurements, each Stokes parameter is interpolated over a three-dimensional region. From these interpolated quantities, the beam's regions of uniform polarization orientation can be obtained to reconstruct its Seifert surfaces. Finally, the intersection of these surfaces is then used to reconstruct the

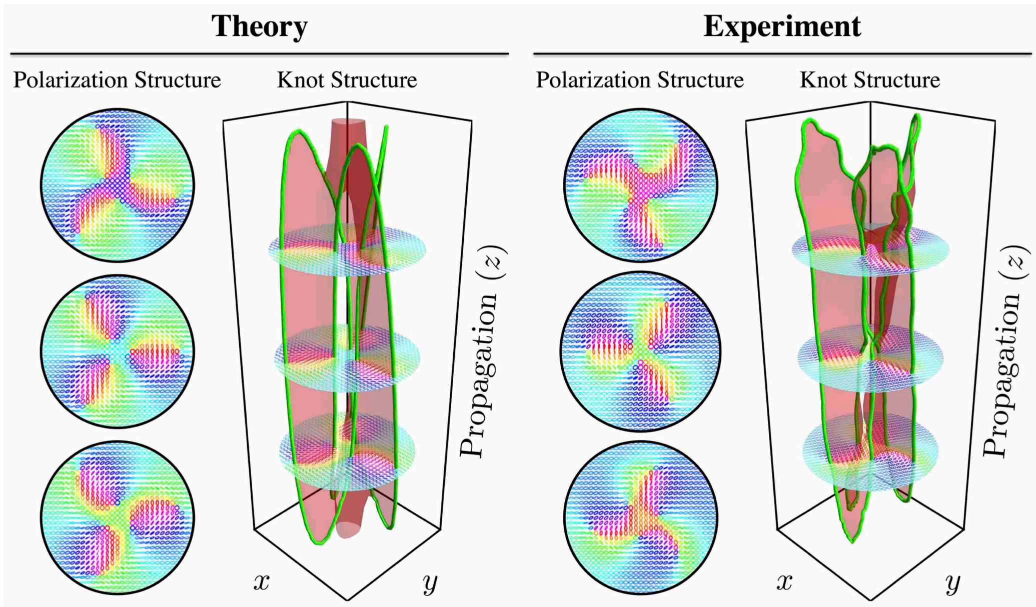

Figure 6.4: **Structural components of optical polarization knots**. By means of polarization measurements at several transverse planes, shown as cross-sectional images, the knot's Seifert surfaces can be reconstructed and their intersection can be used to extract the knotted C-points from the measured polarization field.

knot formed by the beam's polarization singularities.

The full capability of the method can be shown by reconstructing the Seifert surfaces of various types of experimentally generated optical knots and links, the list of which includes a Hopf link, a trefoil knot, a cinquefoil knot, and a figure-eight knot. The results of this reconstruction are displayed in Fig. 6.5. The phase structure required to produce the Hopf link, the trefoil, and the cinquefoil knot, all of which are torus structures, were based on well-known generation schemes [13]. This scheme essentially relies on formulating their fields based on an LG mode decomposition, which can be readily achieved with spatial light modulators (SLM), i.e. $\psi_{\text{Knot}}(\rho,\varphi,z) = \sum_{\ell,p} c^{\text{Knot}}_{\ell,p}\psi^{\text{LG}}_{\ell,p}(\rho,\varphi,z)$. The expansion coefficients required to generate a Hopf link, a trefoil knot, and a cinquefoil knot [13] can be found in Table 6.1. The explicit formulation of LG modes [2] is provided below

$$\psi^{\text{LG}}_{\ell,p}(\rho,\varphi,z) = \left(\frac{2\,p!}{\pi\,(p+|\ell|)!}\right)^{1/2} \frac{1}{w(z)} \left(\frac{\rho\sqrt{2}}{w(z)}\right)^{|\ell|} \exp\left(-\frac{\rho^2}{w^2(z)}\right) L_p^{|\ell|}\left(\frac{2\rho^2}{w^2(z)}\right) \exp\left(i\Phi^{\text{LG}}_{\ell,p}\right), \tag{6.1}$$

Table 6.1: LG expansion coefficients $c_{\ell,p}^{\text{Knot}}$ required to produce torus structures including a Hopf link (2_1), a trefoil knot (3_1), and a cinquefoil knot (5_1).

ℓ	p	Hopf Link $c_{\ell,p}^{2_1}$	Trefoil $c_{\ell,p}^{3_1}$	Cinquefoil $c_{\ell,p}^{5_1}$
0	0	2.63	1.71	0.61
0	1	-6.32	-5.66	-2.56
0	2	4.21	6.38	6.15
0	3	0	-2.3	-6.35
0	4	0	0	2.92
0	5	0	0	-0.61
2	0	-5.95	0	0
3	0	0	-4.36	0
5	0	0	0	-2.45

where (ρ, φ, z) are the cylindrical coordinates, ℓ and p are two integer indices such that $p \geq 0$, w_0 is the mode's beam waist at the focus, $z_R = \pi {w_0}^2/\lambda$ is its Rayleigh range, λ is the beam's wavelength, $w(z) = w_0(1+(z/z_R)^2)^{1/2}$, $L_p^{|\ell|}(.)$ is the associated Laguerre polynomial, and $\Phi_{\ell,p}^{\text{LG}}$ consists of the phase of the beam and is given by

$$\Phi_{\ell,p}^{\text{LG}} = \frac{k\,\rho^2}{2R(z)} + \ell\varphi + kz - (2p + |\ell| + 1)\,\arctan\left(\frac{z}{z_R}\right), \tag{6.2}$$

where $R(z) = z(1 + (z_R/z)^2)$ is related to the beam's wavefront curvature and $k = 2\pi/\lambda$ is the beam's wavevector.

The phase structure that was used to produce the figure-eight knot is based on the formulation of a recently introduced field whose phase vortices form such a knot [69]. Its field formulation is given by

$$\begin{aligned} \psi_{a,b,s}^{\text{Fig-8}}(\varrho, \varphi, z=0) = (&8a^3\varrho^6 e^{-2i\varphi} + 8a^3\varrho^6 e^{2i\varphi} + 16a^3\varrho^4 e^{-2i\varphi} + 16a^3\varrho^4 e^{2i\varphi} \\ &+ 8a^3\varrho^2 e^{-2i\varphi} + 8a^3\varrho^2 e^{2i\varphi} + 12a^2\varrho^8 + 24a^2\varrho^6 - 24a^2\varrho^2 - 12a^2 \\ &+ 6ab^2\varrho^6 e^{-2i\varphi} + 6ab^2\varrho^6 e^{2i\varphi} + 12ab^2\varrho^4 e^{-2i\varphi} + 12ab^2\varrho^4 e^{2i\varphi} \\ &+ 6ab^2\varrho^2 e^{-2i\varphi} + 6ab^2\varrho^2 e^{2i\varphi} - 24ab\varrho^6 e^{-2i\varphi} + 24ab\varrho^6 e^{2i\varphi} \\ &+ 24ab\varrho^2 e^{-2i\varphi} - 24ab\varrho^2 e^{2i\varphi} - 4b^3\varrho^4 e^{-4i\varphi} + 4b^3\varrho^4 e^{4i\varphi} \\ &- 3b^2\varrho^8 - 6b^2\varrho^6 + 6b^2\varrho^2 + 3b^2 - 16\varrho^8 + 32\varrho^6 - 32\varrho^2 + 16)e^{-(\varrho/s)^2} \end{aligned} \tag{6.3}$$

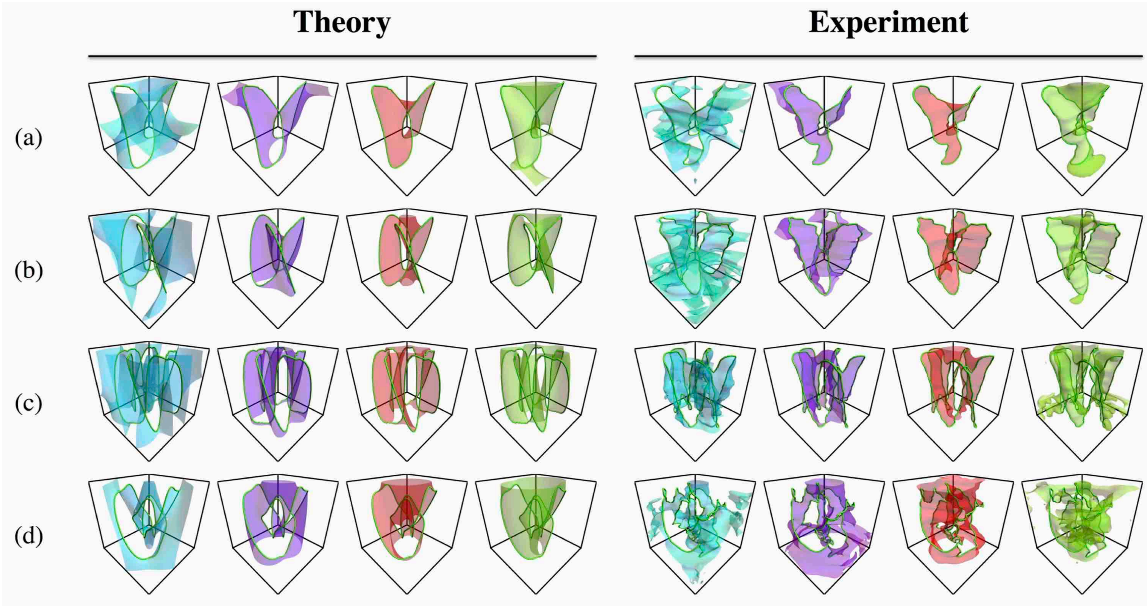

Figure 6.5: **Seifert surfaces**. Seifert surface reconstruction of experimentally generated and numerically simulated optical knots. The considered structures include a Hopf link, a trefoil knot, a cinquefoil knot, and a figure-eight knot.

where ϱ is a scaled dimensionless radial coordinate, φ is the transverse azimuthal coordinate, and a, b, and s are parameters that determine the shape of the knot. The knot presented in Fig. 6.5 was defined by parameters of $a = 0.6$, $b = 1$, and $s = 1.55$. Instead of decomposing this field in the LG basis, the generation scheme for the figure-eight knot relies on a hologram that is directly designed to produce the field in Eq. (6.3) at the $z = 0$ plane.

This field, however, is defined by an extremely low intensity in the region where the knot is formed and as such difficult to generate and observe in the laboratory. However, our polarimetric method is sensitive enough to resolve and characterize its complex pattern. As shown in Fig. 6.5, such a characterization clearly displays the differences between its defining features from those of the torus structures.

The examined knots' Seifert surfaces can also be used to provide useful information regarding their topology. To illustrate this ability, the genus of the figure-eight knot's surfaces, i.e. the number of holes in the surfaces, is numerically extracted from them. As shown in Fig. 6.6, two supplementary holes temporarily appear in the theoretical surfaces in the proximity of those attributed to a polarization orientation of 0. Physically, these holes are caused by instabilities in the knot's wavefield. As a result, these holes lead to a higher genus in the corresponding surfaces. Though the phase fronts, and thus the Seifert surfaces, of the experimentally acquired figure-eight knot are far more detailed due to imperfections in the generation scheme, similar instabilities can be observed in their genus. This is reflected in the plot of Fig. 6.6 where it can be noticed that the genus' dependence on the Seifert surface similarly seems to be centred about the 0 orientation surface. Both the surface analysis of the experimental and theoretical structures unequivocally reveal instabilities in the topological structures of the generated optical figure-eight knot which could be of use when designing custom knotted light fields defined by specific topological properties.

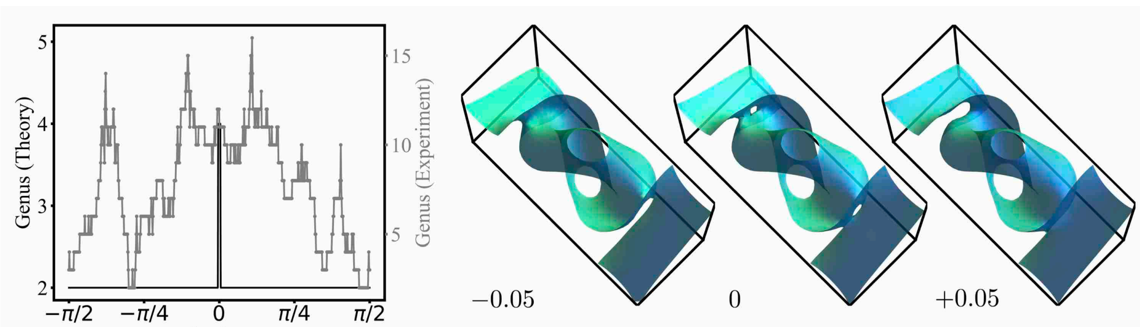

Figure 6.6: **Genus of the figure-eight knot**. Genus of the figure-eight knot's Seifert surfaces acquired both experimentally and theoretically. Theoretical plots of the unstable surfaces around which the two extra holes appear are also shown.

6.4 Prospective Applications

The polarization structure of the optical knots presented in this chapter could be of use within several contexts. For instance, the fact that their knotted wavefield is easily and accurately characterized could lead to experimental works generating polarization structures defined by more interesting topologies such as the ones presented in several theoretical works [69, 70]. Moreover, these optical knots could be used to study knots in physical systems that are sensitive to optical polarization singularities such as the optical nonlinear medium discussed in chapter 5 [52]. One could for instance analyze phenomena regarding nonlinearly induced variations in the topology of the knots' Seifert surfaces by means of a reconstruction process similar to the one presented in this chapter. Such studies would however prospectively require a polarization knot generation scheme that is riddled with less experimental imperfections in order to produce higher quality knots. This could potentially be achieved by scaling down the generation scheme presented in this chapter to one defined by fewer optical components that are routinely used to create beams with polarization singularities. These components could for instance include the liquid crystal devices presented in chapter 2 [25].

Chapter 7

Conclusions

In conclusion, the body of works presented here encompasses several studies pertaining to the topology of structured waves, how it manifests itself in the wave's physical features, and how it can be extracted by means of newly developed characterization methods. In some of the works, this topology was restrained to the central phase singularity of OAM-carrying beams. Other works, however, regarded the generation and the characterization of more complex topological structures such as optical knots.

The generation of structured optical beams by means of geometric phases was first investigated. In this work, devices enclosing arbitrarily aligned liquid crystals were used to generate beams defined by non-trivial phase topologies. By exploiting the birefringence of the liquid crystal molecules, the fabricated devices could also be used to produce beams defined by transverse polarization topologies. This was achieved by either feeding the liquid crystal cells with linearly polarized light or by tuning the birefringence of the liquid crystal molecules with an applied voltage function. The accuracy of the employed fabrication method was demonstrated by making devices defined by complex liquid crystal alignment patterns such as ones used to produce Ince-Gauss modes or optical beams carrying high values of OAM.

New extensions to OAM sorting schemes were then presented and experimentally demonstrated. On one hand, by using nematic liquid crystal cells, a generalized optical angular momentum sorter was fabricated and characterized. In addition to sorting optical OAM states, the device was also able to sort spin angular momentum, or polarization, states thus enabling its use in quantum information protocols operating over a larger basis of quantum optical states. To demonstrate this capability, this sorter was used in a ten-dimensional BB84 quantum key distribution protocol. On the other hand, an OAM sorting scheme for electron waves relying on nano-fabricated SiN holograms was also presented. Its use in materials science was also demonstrated by illustrating its performance in decomposing the OAM spectrum of an electron wave affected by a magnetic nano-structure.

In addition to proposing the above sorting schemes, a proposal to non-destructively measure the OAM carried by an electron was also put forward. This proposal relied on the OAM-dependent magnetic dipole moment carried by electrons which causes them to be defined by an OAM-dependent azimuthal vector potential. This electromagnetic property causes them to induce an OAM-dependent current inside a conductive loop upon propagating through it. The resulting interaction is strong enough to produce an observable current yet too weak to affect the physical properties of the electron itself. In particular, the magnetic fields produced by the induced current are not significant enough to affect the motion of the electron nor change its phase and their symmetry prevents the modification of the passing electron's OAM.

The behaviour of exotic forms of structured waves was explored as well. Namely, the stability of optical beams carrying phase vortices upon propagation through a nonlinear medium was compared to that of beams with polarization singularities. It was observed that beams with polarization singularities experienced a much more stable nonlinear propagation which makes them more desirable for carrying high amounts of optical power through nonlinear media. The effect of twisting a neutron's wavefunction was also investigated. Namely, it was suggested that such effects lead to charge and current densities arising from both the neutron's internal structure and the strength of the phase vortex at the centre of the neutron. These densities in turn manifest themselves in the neutron's multipole moments.

Finally, optical beams carrying knotted polarization singularities were generated. In addition to producing torus knots, which were previously investigated within the framework of optical phase singularities, the generation scheme presented here was also able to create optical figure-eight knots. The wavefield formed by the beams' transverse polarization structures could accurately be characterized given the lower intensity variations across the beams' profile. This characterization enabled the reconstruction of the examined knots' Seifert surfaces, which provided important information regarding the knots' topologies. The usefulness of the investigated structures arises from their ease of characterization, which could motivate the implementation of more complex topological optical structures, and their patterned polarization profile, which could be of use to produce knots in more exotic physical systems.

APPENDICES

Appendix A

Supplementary material: Measuring the orbital angular momentum spectrum of an electron beam

Supplementary Figures

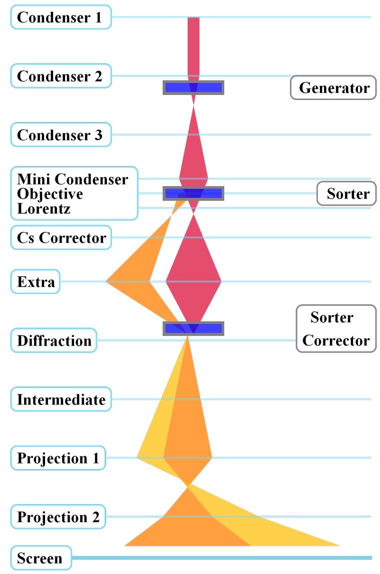

Supplementary Figure 1: **Experimental configuration of the electron sorter depicting the ray path of the electron beam.** Zeroth diffraction orders from our holograms are plotted in the same colour as that of the incident beam's while the first diffraction orders containing the hologram's phase information are plotted in different colours. Light blue lines depict the position of our electron microscope's lenses in our configuration and are labeled on the left side of the figure. Blue rectangles illustrate the phase elements of our sorter as reported in Fig. 1 and are labeled on the right side of the figure. Here, the vertical positions of the lenses are semi-quantitatively accurate and no form of horizontal scaling is considered.

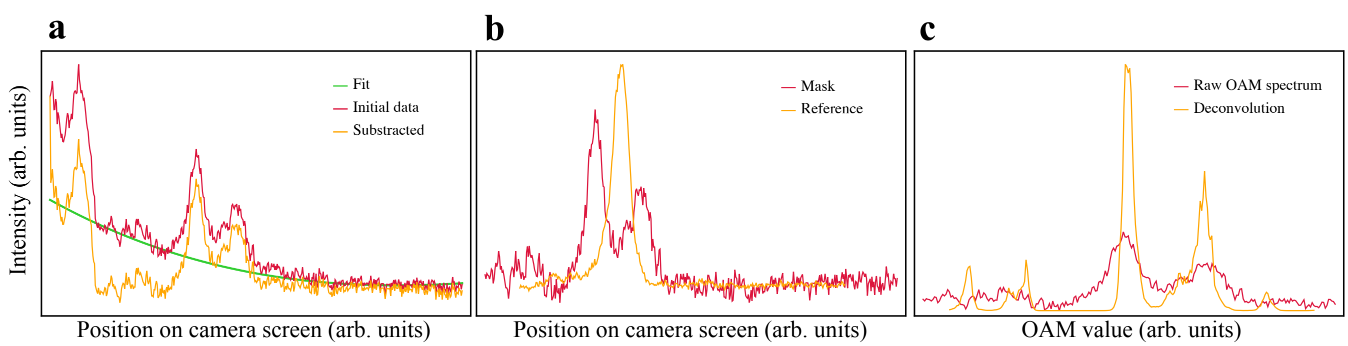

Supplementary Figure 2: **Obtained OAM spectra at various stages of its processing. a** Raw data obtained from the sorter's output along with the fitted background and the background subtracted data. **b** Background subtracted data along with the reference zero-OAM electron beam used for the sorter's calibration. **c** Raw calibrated OAM spectrum and its deconvoluted version.

Supplementary Note 1: Experimental Configuration

Here, we provide a more detailed version of our electron sorter. Our implemention was configured within a FEI Titan HOLO TEM electron miscroscope which has the extra lens required to compensate for the beam's diffraction in the plane of the sorter's phase elements. The position of the microscope's lenses along with the phase elements used to perform the mapping and how they influence the electron beam are provided in Supplementary Figure **1**. Let it be noted that the microscope's Cs lens is in a pass-through configuration. Namely, the electrons exiting the lens are in the same state as when they entered it. That being said, the Cs lens is depicted below as a thin lens with a very long focal length.

The full lens configuration was calculated using the EASYLENS software that is currently under development. The configuration is derived from the microscope's LOW mag configuration and uses an exceptionally large excitation of the Extra lens. The first hologram is placed in the microscope's C2 aperture to produce our test wavefunctions. A second hologram, i.e. the sorter, is placed in the microscope's sample position. In this way the hologram can be easily adjusted in terms of rotations. The third hologram, i.e. the sorter-corrector, is placed in the microscope's SAD (selected area diffraction) aperture. The final OAM spectrum is formed on a CCD camera in image mode where the beam is observed in diffraction mode.

Supplementary Note 2: Sorter and corrector holograms

The required unwrapping process can be achieved by means of a log-polar coordinate transformation through the use of two coupled diffractive holograms. However, due to some differences between the optical sorter and our electron microscope-based apparatus, we must resort to bringing slight adaptive corrections to the phase grating of these holograms. On one hand, the phase corresponding to the first one is modified to

$$\Lambda_1 = \varphi_0 \,\mathrm{sign}\left(\sin\left(2\pi\, a\left[y \arctan\left(\frac{y}{x}\right) + x \ln\left(\frac{\sqrt{x^2+y^2}}{b}\right) + x\right]\right)\right) \tag{1}$$

where a and b are two parameters scaled to optimize the method's experimental efficiency while sign denotes the sign function. On the other hand, the added phase associated with the second hologram becomes

$$\Lambda_2 = \varphi_1 \,\mathrm{sign}\left(\sin\left(2\pi\, a\, b\, \exp\left(-2\pi\frac{u}{a}\right)\cos\left(2\pi\frac{v}{a}\right)\right) + 2\pi\, c\, v\right), \tag{2}$$

where $u = -a \ln\left(\sqrt{x^2+y^2}/b\right)$, $v = a \arctan(y/x)$, and c consists of an additional scaling parameter. For our sorter, we used parameters of $a = 2$, $b = 0.01$, and $c = 0.6$. The factors φ_0 and φ_1 in the phase expressions of both elements should take values of π in order to maximize their respective diffraction efficiencies. Moreover, in order to adapt this method to a transmission electron microscope (TEM), supplementary sets of lenses and apertures were also added.

Supplementary Note 3: Devices to generate test wavefunctions

To generate OAM carrying electrons, a $\exp(i\,\alpha(\varphi))$ term must be added to the formulation of their wavefunctions, where $\alpha(\varphi)$ is a function depending on the azimuthal coordinate ($\varphi \in [0, 2\pi]$). To do so, we employ phase masks which will introduce some losses to the intensity of the electron beam which can be attributed to absorption. We modify the term imparted to the wavefunctions to $\exp(i\,\alpha(\varphi) - a(\varphi))$, where a is a positive constant accounting for any absorption related effects.

Two-level masks

The phase designed to be added by a two level mask is defined by

$$\alpha(\varphi) = \begin{cases} 0 & 0 < \mathrm{mod}(n\varphi, 2\pi) < \pi \\ \delta_0 & \pi < \mathrm{mod}(n\varphi, 2\pi) < 2\pi \end{cases}. \tag{3}$$

where $\mathrm{mod}(x, b)$ yields the remainder of the division of x by b and n is an integer. It thus follows that such a plate's influence on an electron's wavefunction is provided by the terms

$$\widetilde{\psi}(\varphi) = \begin{cases} 1 & 0 < \mathrm{mod}(n\varphi, 2\pi) < \pi \\ \exp(-a + i\,\delta_0) & \pi < \mathrm{mod}(n\varphi, 2\pi) < 2\pi \end{cases}. \tag{4}$$

To obtain the OAM components of a beam generated by such a mask, we must find the expansion coefficients of this term's Fourier series expanded in φ, namely

$$c_\ell = \frac{1}{2\pi}\int_0^{2\pi} \widetilde{\psi}(\varphi)\exp(i\,\ell\varphi)\,d\varphi \tag{5}$$

$$= \begin{cases} \frac{n}{\ell\pi}[-1+\exp(-a+i\,\delta_0)] & \ell = nm \\ 0 & \ell \neq nm \\ \frac{1}{2}[1+\exp(-a+i\,\delta_0)] & \ell = 0 \end{cases} \tag{6}$$

where m is an odd integer. For non-absorptive masks, i.e. $a = 0$, these coefficients become

$$c_\ell = \begin{cases} \frac{2n}{\ell\pi}(\exp(i\,\delta_0/2)\sin(\delta_0/2)) & \ell = nm \\ 0 & \ell \neq nm\ . \\ \exp(i\,\delta_0/2)\cos(\delta_0/2) & \ell = 0 \end{cases} \tag{7}$$

Due to their well-defined periodicity, these holograms have very strong selection rules.

Spiral masks

These masks are designed to add a phase of $\alpha(\varphi) = (\delta_0 \mathrm{mod}(n\varphi, 2\pi))/2\pi$ to electron wavefunctions. As in the case of two-level masks, we use the corresponding Fourier coefficients to determine the OAM content acquired by electrons upon propagation through this type of element. These coefficients are provided by

$$|c_\ell| = \begin{cases} \frac{\sin\left(\frac{2\pi\ell}{n}+\delta_0\right)}{\ell+\delta_0/2\pi}, & \ell = nm \\ 0, & \ell \neq nm \end{cases} \tag{8}$$

where m is a positive integer. For $\delta_0 = 2\pi$, the hologram produces a vortex beam carrying OAM of $\ell = n$.

Supplementary Note 4: OAM spectrum processing

Experimental OAM spectra obtained from the sorter were analyzed using conventional spectroscopy techniques. Background noise is first subtracted from the obtained signal by fitting it to a third order polynomial and then subtracting the fit from the raw data as shown in Supplementary Figure **2-a**. The OAM scale of the spectra is then calibrated using data obtained from a reference beam. In our case, this reference consisted of a superposition of ±4 OAM states and a reference beam carrying no OAM, both of which are depicted in Supplementary Figure **2-b**. The calibrated signal is then deconvoluted using the maximum entropy method after clipping negative values in the spectra. The effect of the employed deconvolution algorithm is shown in Supplementary Figure **2-c**. Finally, a binning procedure is conducted by assembling all pixels between values of $\ell - 0.5$ and $\ell + 0.5$ from which we obtain discretized OAM spectra. Optimizations of the binning offsets are also performed in order position the spectra's maxima in the centre of their respective bins.

Supplementary Note 5: Analysis of the interaction between the dipole and electrons

Phase added by a Magnetic Dipole onto an Electron Beam

Here we provide a rough derivation of the term $g(r, \varphi)$ from Eq. (2)) introduced by a magnetic dipole to an electron wavefunction. Consider an electron traveling along the z axis and a magnetic dipole lying in the x, y plane such that its magnetic dipole moment $\mathbf{m}$ is oriented along the x axis, i.e. $\mathbf{m} = \mathcal{M}\,\mathbf{e}_x$, where $\mathbf{e}_x$ is the unit vector along the x axis. The phase acquired by the electron upon propagating through the dipole's magnetic field is given by the path integral $\chi = (e/\hbar)\int_C \mathbf{A}\cdot d\mathbf{x}$, where $\mathbf{A}$ is the dipole's vector potential which is given by $\mathbf{A}(\mathbf{x}) = (\mu_0\,\mathbf{m}\times\mathbf{x})/(4\pi\,|\mathbf{x}|^3)$, where $\mathbf{x} = r\,\mathbf{e}_r + z\,\mathbf{e}_z$ and (r, φ, z) are the cylindrical coordinates. Because the electron travels along the z direction, then χ is to be calculated along the z axis and only the z component of the vector potential, A_z, becomes relevant to the calculation, i.e. $\chi = (e/\hbar)\int_{-\infty}^{+\infty} A_z\, dz$. Given that $\mathbf{m}\times\mathbf{x} = -\mathcal{M}\, z\, \mathbf{e}_y + \mathcal{M}\, r \sin(\varphi)\, \mathbf{e}_z$, then it follows that our phase is given by

$$\chi = \frac{e}{\hbar}\int_{-\infty}^{+\infty} \frac{\mu_0}{4\pi}\frac{\mathcal{M}\, r \sin(\varphi)}{(r^2+z^2)^{3/2}}\, dz = \frac{e}{\hbar}\frac{\mu_0}{4\pi}\frac{2\mathcal{M}\, r \sin(\varphi)}{r^2} = \frac{e\,\mu_0\,\mathcal{M}}{h\, r}\, \sin(\varphi) \tag{9}$$

which corresponds to Eq. (2).

Predicting the OAM Expansion Coefficients

We can obtain the expansion coefficient c_ℓ attributed to the phase added by a magnetic dipole onto an electron beam by performing a Fourier transform of the term, g as introduced in Eq. (2), added by the dipole onto the wavefunction of the electrons. This transformation must be performed in terms of the Cartesian coordinates (u, v) of the plane in which the beam is unwrapped. It therefore follows that these coefficients are given by

$$c_{p,\ell} = \int_{-\infty}^{+\infty}\int_{-\infty}^{+\infty} \exp(i\chi(r(u))\sin\varphi(v))\exp(i\,\ell v)\exp(i\,up)\, du\, dv \tag{10}$$

Given that our transformed coordinates are defined by $u = -a\ln(r/b)$ and $v = a\varphi$, we perform according variable substitutions in order to obtain an expression for the coefficients in terms of polar coordinates. For simplicity, we assume that a and b are equal to 1 and obtain

$$c_{p,\ell} \;=\; \int_0^{2\pi}\int_0^{\infty} \exp(i\chi(r)\sin\varphi)\exp(i\,\ell\varphi)\exp(-i\;\ln(r)p)\, dr\, d\varphi \tag{11}$$

In the case where an intermediate aperture is added to sorter's configuration, we may model this addition by modulating the above integrand by a Gaussian function or more precisely a radial step-function $W(r)$. In the case where this aperture is sufficiently narrow, we may consider that the main coefficients in the OAM spectrum are for p values satisfying $p \approx 0$ hence allowing us to neglect any other values of p. Based on these considerations, we may further simplify our expansion coefficients to

$$c_\ell \approx c_{0,\ell} \;=\; \int_0^{2\pi}\int_0^{\infty} \exp(i\chi(r)\sin\varphi)\exp(i\,\ell\varphi)W(r)\, dr\, d\varphi. \tag{12}$$

We then expand $\exp(i\chi(r)\sin\varphi)$ using the Jacobi-Anger identity. Due to the orthonormality between the exponentials in the resulting expression, we may further simplify the expansion coefficient to

$$c_{0,\ell} \;=\; \int_0^{\infty} J_\ell(\chi(r))W(r)\, dr \approx \int_{r_0-\sigma}^{r_0+\sigma} J_\ell(\chi(r))\, dr \tag{13}$$

where the bounds of integration $r_0 - \sigma$ and $r_0 + \sigma$ are used to approximate the influence of the modulating apperture function on the expansion coefficients. From this expression, we observe that $c_{0,\ell} \approx 0$ when $\chi(r) \ll \ell$. Likewise, in the case where $\chi(r) \gg \ell$, the integrand oscillates rapidly and integration over these larger r values will likewise yield negligible contributions. Therefore, these $c_{0,\ell}$ coefficients will only hold significant values over a range where $\chi(r)$ is near $|\ell|$.

Appendix B

Supplementary Information: Nondestructive Measurement of Orbital Angular Momentum for an Electron Beam

Supplemental material for "Non-destructive measurement of an electron beam's orbital angular momentum"

Hugo Larocque,[1] Frédéric Bouchard,[1] Vincenzo Grillo,[2] Alicia Sit,[1] Stefano Frabboni,[2,3] Rafal E. Dunin-Borkowski,[4] Miles J. Padgett,[5] Robert W. Boyd,[1,6] and Ebrahim Karimi[1,7,*]

[1]*The Max Planck Centre for Extreme and Quantum Photonics, Department of Physics, University of Ottawa, 25 Templeton St., Ottawa, Ontario, K1N 6N5 Canada*
[2]*CNR-Istituto Nanoscienze, Centro S3, Via G Campi 213/a, I-41125 Modena, Italy*
[3]*Dipartimento FIM Universitá di Modenae Reggio Emilia, Via G Campi 213/a, I-41125 Modena, Italy*
[4]*Ernst Ruska-Centre for Microscopy and Spectroscopy with Electrons, Forschungszentrum Jülich, Jülich 52425, Germany*
[5]*School of Physics and Astronomy, Glasgow University, Glasgow, G12 8QQ, Scotland, UK*
[6]*Institute of Optics, University of Rochester, Rochester, New York, 14627, USA*
[7]*Department of Physics, Institute for Advanced Studies in Basic Sciences, 45137-66731 Zanjan, Iran*

EXPERIMENTAL SCHEMATICS

We propose the following electron microscope-based apparatus, whose schematic is provided in Fig. 1, to non-destructively measure an electron's orbital angular momentum (OAM). The OAM-carrying electron beam passes through an objective lens focusing it through the conductive loop. The latter is held by the microscope's sample holder and also possesses a thin slit in which leads are placed and connected to an ammeter. As the electron passes through the conductive loop, it induces quantized Eddy currents associated with its OAM, given by Eq. (4) of the main text, which are thereafter read out by the ammeter. Should the discontinuity introduced by the thin slit provide any obstacles hindering our proposed measurement, an alternative way of measuring a passing electron's OAM would be to wrap the cylinder with a nanoscale solenoid. Much like the cylinder itself, the solenoid would pickup the electromotive force caused by the passage of the electron, thus resulting in the generation of quantized currents within its coils.

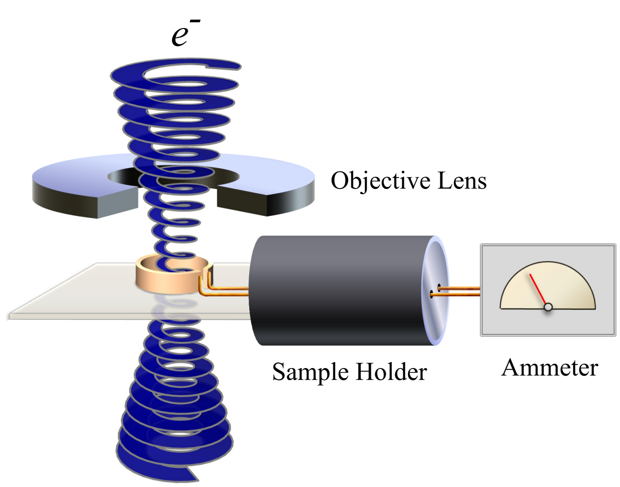

FIG. 1. Proposed experimental schematic for the non-destructive measurement of an electron beam's orbital angular momentum. An OAM-carrying electron beam, which possesses quantized magnetic dipoles, is being focused through a conductive loop. The magnetic dipole induces a quantized current in the loop that is read out by an ammeter.

ASYMMETRICAL CONSIDERATIONS

We now consider how the induced currents are affected by breaking the apparatus' cylindrical symmetry. We assume that the most likely imperfection is that the electron trajectory is offset in the transverse direction from its ideal position on the axis of the cylinder. Placing an interacting element perpendicularly to an electron beam is usually not a practical issue. As illustrated in Fig. 2, where we considered the parameters employed in Fig. 2 of the main text, a simple extension of our analysis reveals that the order of magnitude of the currents related to the electron's OAM is not affected by these offsets. In particular, the currents shown in Fig. 2 are found based on the azimuthal electric field induced in the region of the conductive loop that will experience the lowest induction. The ratio between such currents defined by passing electrons with different OAM values remains constant. Therefore, breaking the

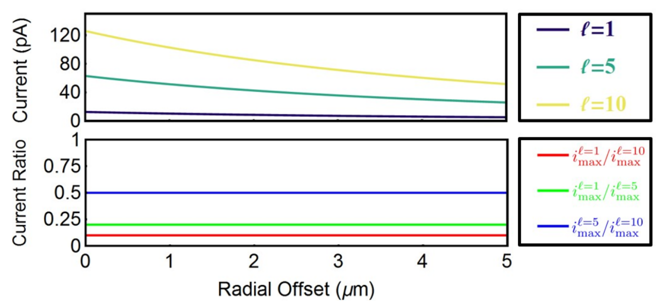

FIG. 2. Maximum induced current induced by the electron upon its propagation as a function of the electron's radial offset along with the corresponding relative ratio between currents induced by electrons defined by different OAM values. These currents correspond to those in the region of the cylinder that will experience the greatest drop in electromotive force upon breaking its symmetry.

apparatus' cylindrical symmetry will not affect the detectable nature of the electrons nor will it change the relative responses associated with electrons of different OAM values.

Though the electron's electric field may also add unwanted contributions to these currents, they do not vary with the electron's OAM. These unwanted contributions may also be suppressed by optimizing certain experimental parameters such as the device's transverse position with respect to the axis along which the electron is displaced.

SUGGESTED MEASUREMENT METHODS

A potential obstacle to our proposed OAM measurement consists of the rather short interaction between the conductive loop and the electron. In particular, for the parameters used in Fig. 2 of the main text, the duration of this interaction is within the order of 0.1 ps, thus making the realizability of this measurement particularly challenging. Though the frequencies of such induced currents can potentially reach high values, e.g. in the order of 10^{13} Hz, the fact that they are significantly below those of optical frequencies refrains the occurence of anomalous phenomena such as the generation of surface plasmons. Therefore, the only obstacle that this short interaction introduces is the challenge of measuring it. However, there are some electronics with ps resolution (e.g. Hydraharp) that can make such a task much easier. Moreover, because the electron's time of passage through the loop scales with the loop's length, a longer cylinder can be used to make the interaction more noticeable. Likewise, lower energy electrons can also be employed to achieve the same effect. Such elementary measures can, to a certain extent, overcome difficulties related to this short interaction. We also propose two additional methods to address issues associated with the electrons's time of passage through the loop.

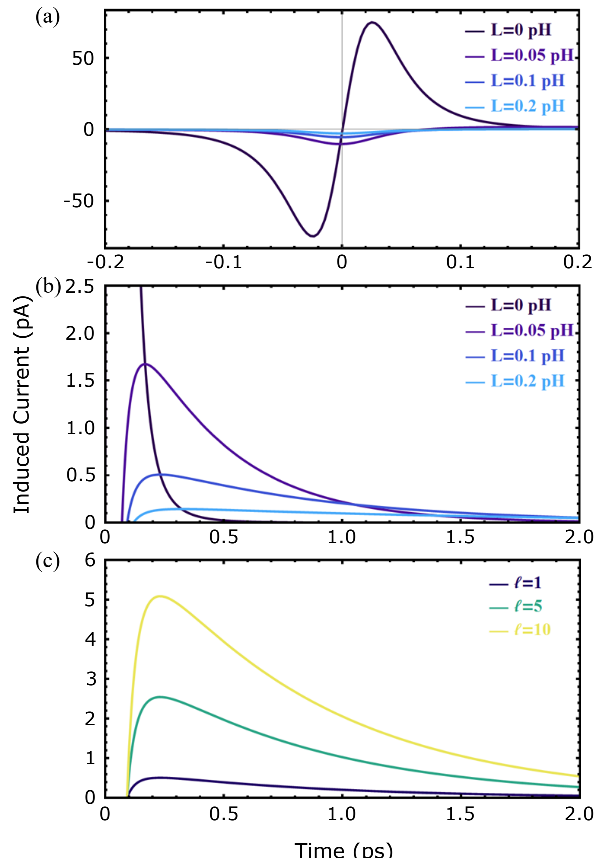

FIG. 4. (a) Currents induced in circuits with inductances of 0, 0.05, 0.1, and 0.2 pH by an electron carrying one unit of OAM. (b) Zoomed in region of (a) over an extended time scale. (c) Currents induced in a circuit with an inductance of 0.1 pH by electrons carrying OAM values of $\ell = 1, 5$, and 10.

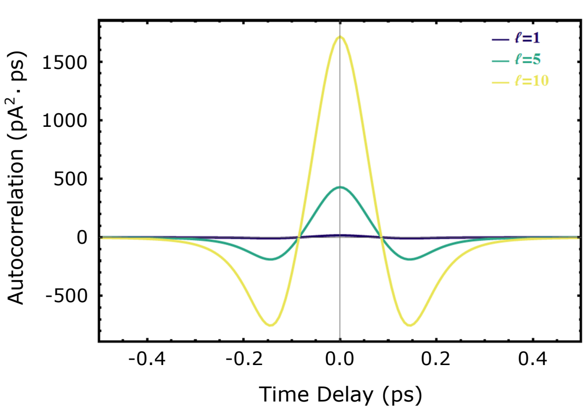

FIG. 3. Autocorrelation functions associated with electrons carrying OAM values of $\ell = 1, 5, 10$. The functions were calculated using the electron and loop parameters employed in Fig. 2 of the main text.

On one hand, the electron's OAM can be measured with an autocorrelation method involving the use of two conductive loops in which currents will be induced by the passage of distinct electrons. With these currents, one can calculate the electron beam's autocorrelation trace, $C(\tau)$, as a function of the time delay between the electrons' passage through their respective loops. This autocorrelation function is provided in Eq. (1)

$$C(\tau) \propto \int_{-\infty}^{\infty} i^{\ell}(t) i^{\ell}(t-\tau)\, dt. \tag{1}$$

This trace will scale with the square of the electron's OAM as depicted in Fig. 3 where we provide the autocorrelation functions calculated using the parameters employed in Fig. 2 of the main text.

On the other hand, methods to "extend" the lifetime of the induced currents would also make them more noticeable. For instance, an inductor could be added to the circuit consisting of the ammeter and the conductive loop. According to Lenz's law, the rate at which the measured current increases as the electron enters the loop will significantly be decreased. However, as the electron exits the loop, the circuit's current will be maintained by the inductor in order to minimize the rate at which the magnetic flux through it decreases. Therefore, though an inductor will lower the registered currents to smaller yet still detectable magnitudes, it will also extend their duration.

We illustrate this concept in the following. First, we assume that the electromotive force induced by the electron's passage inside the loop is not affected by the addition of the inductor. Second, to simplify, we assume that the EMF induced inside the loop is uniform over its length as opposed to what was calculated in the main text. Last, we assume that our system consisting of the loop and the inductor can be represented by a series RL circuit in which the driving voltage is the electromotive force induced inside the cylinder $\mathcal{E}(t)$, the resistance is that associated with the dimensions and the material of the cylinder R, and the inductance is that of the inductor L. The resulting differential equation describing the induced current's $I(t)$ time evolution is thus

$$\mathcal{E}(t) - L\frac{dI}{dt} = I\,R. \tag{2}$$

We numerically solve Eq. (2) for the parameters used in Fig. 2 of the main text for various OAM and inductance values where $t = 0$ corresponds to the moment where the electron is halfway through the loop. The solutions for the currents induced by an electron carrying one unit of OAM and circuits with inductance values of 0, 0.05, 0.1, and 0.2 pH are shown in Fig. 4(a). The same solutions are displayed in Fig. 4(b) over a zoomed in region of Fig. 4(a) (highlighted in blue) corresponding to a longer time interval. We can clearly observe the influence of the inductor's presence in the circuit, i.e., the current varies less abruptly upon the electron's arrival and decays at a much slower rate after the electron exits the loop. More specifically, as the electron enters the loop, the inductor considerably reduces the circuit's current in such a way to minimize any variations in its magnetic flux. Unlike the case where there is no inductor, the current keeps on diminishing as the electron arrives midway through the loop in order to counter the fact that the induced EMF goes back to zero. The current starts to come back up once the electron starts leaving the loop and eventually starts decaying.

Fig 4(c) displays the induced current as the electron leaves the loop for OAM values of $\ell = 1$, 5, and 10 and a circuit with an inductance of 0.1 pH. As in the case where there is no inductor, the currents remain quantized and proportional to the electron's OAM value in addition to keeping observable values over a longer period of time.

Appendix C

Supplementary Information: Polarization Shaping for Control of Nonlinear Propagation

Supplemental material for Polarization shaping for control of nonlinear propagation

Frédéric Bouchard,[1] Hugo Larocque,[1] Alison M. Yao,[2] Christopher Travis,[2] Israel De Leon,[1,3] Andrea Rubano,[4] Ebrahim Karimi,[1,5,*] Gian-Luca Oppo,[2] and Robert W. Boyd[1,6]

[1]*The Max Planck Centre for Extreme and Quantum Photonics, Department of Physics, University of Ottawa, 25 Templeton, Ottawa, Ontario, K1N 6N5 Canada*
[2]*SUPA and Department of Physics, University of Strathclyde, 107 Rottenrow, Glasgow G4 0NG, Scotland, U.K.*
[3]*School of Engineering and Sciences, Tecnológico de Monterrey, Monterrey, Nuevo Leon 64849, Mexico.*
[4]*Dipartimento di Fisica, Università di Napoli Federico II, Compl. Univ. di Monte S. Angelo, via Cintia, 80126 Napoli, Italy*
[5]*Department of Physics, Institute for Advanced Studies in Basic Sciences, 45137-66731 Zanjan, Iran*
[6]*Institute of Optics, University of Rochester, Rochester, New York, 14627, USA*

STABILITY OF VECTOR VORTEX BEAMS

The increased stability of the spiral vector vortex beam observed in the central column of Fig. 3 of the main text is a specific case of the increased stability of vector solitons upon propagation through a self-focusing medium. This stability extends to other equally weighted ($\gamma = \pi/4$) superpositions of orthogonally polarized components carrying opposite values of OAM (i.e. vector vortex beams). In terms of the formalism employed in the main text, the stability of a vector vortex beam is independent of its defining β parameter. We show this experimentally in Fig. 1, where the transverse intensity profiles of several vector vortex beams are depicted prior to and following their propagation through rubidium atomic vapour. Experimental parameters were set to conditions where scalar beams would undergo beam breakup and then held constant throughout. Though their stability is significantly higher than that of their scalar counterpart, minor defects associated with their propagation can still be observed in their transverse polarization profiles.

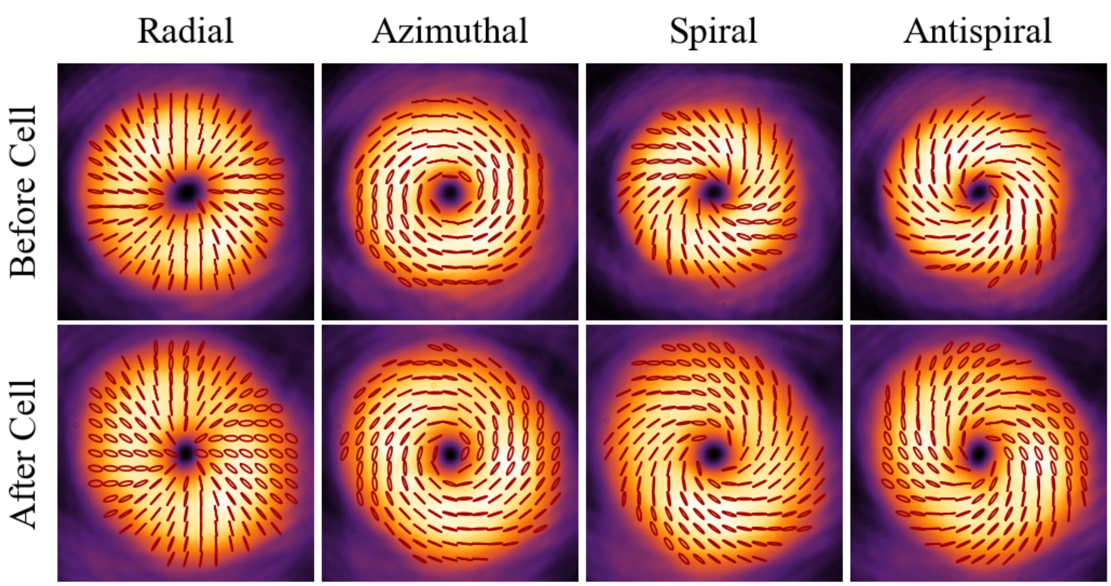

FIG. 1. Transverse intensity profiles of vector vortex beams (radial, azimuthal, spiral, and antispiral), prior and following their propagation through rubidium atomic vapour held under conditions where scalar OAM-carrying beams undergo beam breakup.

PROPAGATION OF SPACE-VARYING POLARIZED LIGHT BEAMS

As observed in Fig. 3 and Fig. 4 of the main text, shaping the polarization profile of an optical beam will make it more stable upon propagation through a self-focusing medium. To increase this stability, the beam must be shaped in a way to equally distribute its intensity into two components that are orthogonally polarized. Doing so will result in the preservation of the beams' transverse profiles over an increased propagation distance. This is clearly depicted in Fig. 2, where we show the longitudinal cross-section of a scalar beam, observed to break up after 9 cm (i.e. the length of the cell used in our experiments), in comparison to vector, lemon, and star

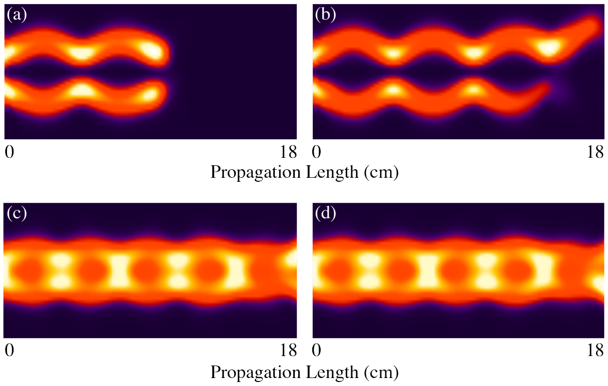

FIG. 2. Numerical data from the integration of Eqs. (2) of the main text showing the cross-section of (a) scalar, (b) vector vortex, (c) lemon topology Poincaré, and (d) star topology Poincaré beams upon propagation through rubidium vapour up to a distance of 18 cm. Parameter values are the same as those of the main text.

Poincaré beams as they propagate through rubidium atomic vapour. This data was obtained from numerical simulations where we consider that the rubidum vapour is held under the conditions used to model the results in Fig. 3 and Fig. 4 of the main text.

Though more stable than their scalar counterpart, the space-varying polarized light beams will experience beam breakup after a certain distance. The transverse profiles of vector vortex, lemon topology, and star topology Poincaré beams after break-up are displayed in Fig. 3. Note that the vector beam breaks at a distance of 13.5 cm while lemon and star Poincaré beams both break at 18 cm. These distances correspond to the final stage of their respective longitudinal cross-sections shown in Fig. 2.

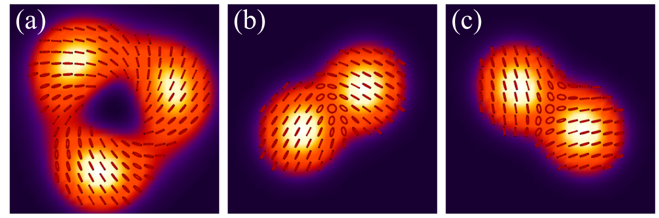

FIG. 3. Transverse profile of (a) vector vortex, (b) lemon topology, and (c) star topology beams after break-up. The profiles of these beams are found at distances of of 13.5 cm, 18 cm, and 18 cm respectively.

The profile of the vortex beam is in good agreement with the results found in reference [2] of the main text. More specifically, we observe, for a beam consisting of components carrying OAM of ± 1, the formation of three lobes consisting of distinct linear polarizations. In contrast lemon and star Poincaré beams break into two lobes, again with distinct linear polarizations.

* ekarimi@uottawa.ca

Bibliography

[1] Hugo Larocque, Ido Kaminer, Vincenzo Grillo, Gerd Leuchs, Miles J. Padgett, Robert W. Boyd, Mordechai Segev, and Ebrahim Karimi, " 'Twisted' electrons," *Contemporary Physics*, 1–19 (2018).

[2] Anthony E. Siegman. Lasers, University Science Books. Mill Valley, CA, 1986.

[3] Miguel A Bandres and Julio C. Gutiérrez-Vega, "Ince–gaussian beams," *Optics letters* **29**, 144–146 (2004).

[4] Ebrahim Karimi, Gianluigi Zito, Bruno Piccirillo, Lorenzo Marrucci, and Enrico Santamato, "Hypergeometric-gaussian modes," *Optics letters* **32**, 3053–3055 (2007).

[5] Halina Rubinsztein-Dunlop, Andrew Forbes, Michael V. Berry, Mark R. Dennis, David L. Andrews, Masud Mansuripur, Cornelia Denz, Christina Alpmann, Peter Banzer, Thomas Bauer, et al., "Roadmap on structured light," *Journal of Optics* **19**, 013001 (2016).

[6] Les Allen, Marco W. Beijersbergen, R. J. C. Spreeuw, and J. P. Woerdman, "Orbital angular momentum of light and the transformation of laguerre-gaussian laser modes," *Physical Review A* **45**, 8185 (1992).

[7] John F. Nye and Michael V. Berry, "Dislocations in wave trains," *Proceedings of the Royal Society of London A* **336**, 165–190 (1974).

[8] John F. Nye. Natural focusing and fine structure of light: caustics and wave dislocations. CRC Press, 1999.

[9] Mark R Dennis, Kevin O'Holleran, and Miles J Padgett, "Singular optics: optical vortices and polarization singularities," *Progress in Optics* **53**, 293–363 (2009).

[10] Michael V. Berry and Mark R. Dennis, "Topological events on wave dislocation lines: birth and death of loops, and reconnection," *Journal of Physics A: Mathematical and Theoretical* **40**, 65 (2006).

[11] Michael V. Berry and Mark R. Dennis, "Knotted and linked phase singularities in monochromatic waves," *Proceedings of the Royal Society of London A* **457**, 2251–2263 (2001).

[12] Jonathan Leach, Mark R. Dennis, Johannes Courtial, and Miles J. Padgett, "Laser beams: knotted threads of darkness," *Nature* **432**, 165 (2004).

[13] Mark R. Dennis, Robert P. King, Barry Jack, Kevin O'Holleran, and Miles J. Padgett, "Isolated optical vortex knots," *Nature Physics* **6**, 118 (2010).

[14] M. W. Beijersbergen, R. P. C. Coerwinkel, M. Kristensen, and J. P. Woerdman, "Helical-wavefront laser beams produced with a spiral phaseplate," *Optics Communications* **112**, 321–327 (1994).

[15] Masaya Uchida and Akira Tonomura, "Generation of electron beams carrying orbital angular momentum," *Nature* **464**, 737 (2010).

[16] Roy Shiloh, Yossi Lereah, Yigal Lilach, and Ady Arie, "Sculpturing the electron wave function using nanoscale phase masks," *Ultramicroscopy* **144**, 26–31 (2014).

[17] N. R. Heckenberg, R. McDuff, C. P. Smith, and A. G. White, "Generation of optical phase singularities by computer-generated holograms," *Optics letters* **17**, 221–223, 1992.

[18] Johan Verbeeck, He Tian, and Peter Schattschneider, "Production and application of electron vortex beams." *Nature*, **467**, 301 (2010).

[19] Vincenzo Grillo, Gian Carlo Gazzadi, Ebrahim Karimi, Erfan Mafakheri, Robert W. Boyd, and Stefano Frabboni, "Highly efficient electron vortex beams generated by nanofabricated phase holograms," *Applied Physics Letters* **104**, 043109 (2014).

[20] Benjamin J. McMorran, Amit Agrawal, Ian M. Anderson, Andrew A. Herzing, Henri J. Lezec, Jabez J. McClelland, and John Unguris, "Electron vortex beams with high quanta of orbital angular momentum," *Science* **331**, 192–195 (2011).

[21] Michael V. Berry, "Quantal phase factors accompanying adiabatic changes," *Proceedings of the Royal Society of London A* **392**, 45–57 (1984).

[22] Shivaramakrishnan Pancharatnam, "Generalized theory of interference and its applications," *Proceedings of the Indian Academy of Sciences A* **44**, 398–417 (1956).

[23] Ze'ev Bomzon, Vladimir Kleiner, and Erez Hasman, "Pancharatnam–Berry phase in space-variant polarization-state manipulations with subwavelength gratings," *Optics letters* **26**, 1424–1426 (2001).

[24] Ebrahim Karimi, Sebastian A. Schulz, Israel De Leon, Hammam Qassim, Jeremy Upham, and Robert W. Boyd, "Generating optical orbital angular momentum at visible wavelengths using a plasmonic metasurface," *Light: Science & Applications* **3**, e167 (2014).

[25] Hugo Larocque, Jérémie Gagnon-Bischoff, Frédéric Bouchard, Robert Fickler, Jeremy Upham, Robert W. Boyd, and Ebrahim Karimi, "Arbitrary optical wavefront shaping via spin-to-orbit coupling," *Journal of Optics* **18**, 124002 (2016).

[26] Lorenzo Marrucci, C. Manzo, and D. Paparo, "Optical spin-to-orbital angular momentum conversion in inhomogeneous anisotropic media," *Physical Review Letters* **96**, 163905 (2006).

[27] Ebrahim Karimi, Lorenzo Marrucci, Vincenzo Grillo, and Enrico Santamato, "Spin-to-orbital angular momentum conversion and spin-polarization filtering in electron beams," *Physical Review Letters* **108**, 044801 (2012).

[28] Yiqiong Zhao, J. Scott Edgar, Gavin D. M. Jeffries, David McGloin, and Daniel T. Chiu, "Spin-to-orbital angular momentum conversion in a strongly focused optical beam," *Physical Review Letters* **99**, 073901 (2007).

[29] Konstantin Y. Bliokh, Mark R. Dennis, and Franco Nori, "Relativistic electron vortex beams: angular momentum and spin-orbit interaction," *Physical Review Letters* **107**, 174802 (2011).

[30] Iwo Bialynicki-Birula and Zofia Bialynicka-Birula, "Relativistic electron wave packets carrying angular momentum," *Physical Review Letters* **118**, 114801 (2017).

[31] Stephen M. Barnett, "Relativistic electron vortices," *Physical Review Letters* **118**, 114802 (2017).

[32] Hugo Larocque and Ebrahim Karimi, "Viewpoint: A new twist on relativistic electron vortices," *Physics* **10** (2017).

[33] Konstantin Y. Bliokh, Mark R. Dennis, and Franco Nori, "Position, spin, and orbital angular momentum of a relativistic electron," *Physical Review A* **96**, 023622 (2017).

[34] Yingwen Zhang, Alicia Sit, Frédéric Bouchard, Hugo Larocque, Eliahu Cohen, Avshalom C. Elitzur, James L. Harden, Robert W. Boyd, and Ebrahim Karimi, "Interaction-free ghost-imaging of structured objects," *arXiv preprint arXiv:1711.09171* (2017).

[35] Alicia Sit, Frédéric Bouchard, Robert Fickler, Jérémie Gagnon-Bischoff, Hugo Larocque, Khabat Heshami, Dominique Elser, Christian Peuntinger, Kevin Günthner, Bettina Heim, et al., "High-dimensional intracity quantum cryptography with structured photons," *Optica* **4**, 1006–1010 (2017).

[36] Hugo Larocque, Jérémie Gagnon-Bischoff, Dominic Mortimer, Yingwen Zhang, Frédéric Bouchard, Jeremy Upham, Vincenzo Grillo, Robert W. Boyd, and Ebrahim Karimi, "Generalized optical angular momentum sorter and its application to high-dimensional quantum cryptography." *Optics Express* **25**, 19832–19843 (2017).

[37] Fanqi Kong, Chunmei Zhang, Frédéric Bouchard, Zhengyan Li, Graham G. Brown, Dong Hyuk Ko, TJ Hammond, Ladan Arissian, Robert W. Boyd, Ebrahim Karimi, et al., "Controlling the orbital angular momentum of high harmonic vortices," *Nature communications* **8**, 14970 (2017).

[38] Alois Mair, Alipasha Vaziri, Gregor Weihs, and Anton Zeilinger, "Entanglement of the orbital angular momentum states of photons," *Nature* **412**, 313 (2001).

[39] Hammam Qassim, Filippo M. Miatto, Juan P. Torres, Miles J. Padgett, Ebrahim Karimi, and Robert W. Boyd, "Limitations to the determination of a laguerre–gauss spectrum via projective, phase-flattening measurement," *Journal of the Optical Society of America B* **31**, A20–A23 (2014).

[40] Gregorius C. G. Berkhout, Martin P. J. Lavery, Johannes Courtial, Marco W. Beijersbergen, and Miles J. Padgett, "Efficient sorting of orbital angular momentum states of light," *Physical Review Letters* **105**, 15360 (2010).

[41] W. J. Hossack, A. M. Darling, and A. Dahdouh, "Coordinate transformations with multiple computer-generated optical elements," *Journal of Modern Optics* **34**, 1235–1250 (1987).

[42] Martin P. J. Lavery, David J. Robertson, Gregorius C. G. Berkhout, Gordon D. Love, Miles J. Padgett, and Johannes Courtial, "Refractive elements for the measurement of the orbital angular momentum of a single photon," *Optics Express* **20**, 2110–2115 (2012).

[43] Mohammad Mirhosseini, Mehul Malik, Zhimin Shi, and Robert W. Boyd, "Efficient separation of the orbital angular momentum eigenstates of light," *Nature Communications* **4**, 2781 (2013).

[44] Damien Prongué, Hans-Peter Herzig, René Dändliker, and Michael T. Gale, "Optimized kinoform structures for highly efficient fan-out elements," *Applied Optics* **31**, 5706–5711 (1992).

[45] Benjamin J. McMorran, Tyler R. Harvey, and Martin P. J. Lavery, "Efficient sorting of free electron orbital angular momentum," *New Journal of Physics* **19**, 023053 (2017).

[46] Vincenzo Grillo, Amir H. Tavabi, Federico Venturi, Hugo Larocque, Roberto Balboni, Gian Carlo Gazzadi, Stefano Frabboni, Peng-Han Lu, Erfan Mafakheri, Frédéric Bouchard, et al., "Measuring the orbital angular momentum spectrum of an electron beam," *Nature Communications* **8**, 15536 (2017).

[47] Maximilian Haider, Stephan Uhlemann, Eugen Schwan, Harald Rose, Bernd Kabius, and Knut Urban, "Electron microscopy image enhanced," *Nature* **392**, 768 (1998).

[48] Vincenzo Grillo, Amir H. Tavabi, Emrah Yucelen, Peng-Han Lu, Federico Venturi, Hugo Larocque, Lei Jin, Aleksei Savenko, Gian Carlo Gazzadi, Roberto Balboni, et al., "Towards a holographic approach to spherical aberration correction in scanning transmission electron microscopy," *Optics express* **25**, 21851–21860 (2017).

[49] Roy Shiloh, Roei Remez, Peng-Han Lu, Lei Jin, Yossi Lereah, Amir H. Tavabi, Rafal E Dunin-Borkowski, and Ady Arie, "Spherical aberration correction in a scanning transmission electron microscope using a sculpted foil," *arXiv preprint arXiv:1705.05232* (2017).

[50] Hugo Larocque, Frédéric Bouchard, Vincenzo Grillo, Alicia Sit, Stefano Frabboni, Rafal E. Dunin-Borkowski, Miles J. Padgett, Robert W. Boyd, and Ebrahim Karimi, "Nondestructive measurement of orbital angular momentum for an electron beam," *Physical Review Letters* **117**, 154801 (2016).

[51] Konstantin Y. Bliokh, Yury P. Bliokh, Sergey Savel'Ev, and Franco Nori, "Semiclassical dynamics of electron wave packet states with phase vortices," *Physical Review Letters* **99**, 190404 (2007).

[52] Frédéric Bouchard, Hugo Larocque, Alison M. Yao, Christopher Travis, Israel De Leon, Andrea Rubano, Ebrahim Karimi, Gian-Luca Oppo, and Robert W. Boyd, "Polarization shaping for control of nonlinear propagation," *Physical Review Letters* **117**, 233903 (2016).

[53] Hugo Larocque, Ido Kaminer, Vincenzo Grillo, Robert W. Boyd, and Ebrahim Karimi, "Twisting neutrons may reveal their internal structure," *Nature Physics* **14**, 1 (2018).

[54] Robert W. Boyd. *Nonlinear optics*. Academic press, 2003.

[55] V. I. Bespalov and V.I. Talanov. "Filamentary structure of light beams in nonlinear liquids," *Journal of Experimental and Theoretical Physics Letters* **3**, 471 (1966).

[56] William J. Firth and Dmitry V. Skryabin, "Optical solitons carrying orbital angular momentum," *Physical Review Letters* **79**, 2450 (1997).

[57] P. D. Maker and R.W. Terhune, "Study of optical effects due to an induced polarization third order in the electric field strength," *Physical Review* **137**, A801 (1965).

[58] Filippo Cardano, Ebrahim Karimi, Sergei Slussarenko, Lorenzo Marrucci, Corrado de Lisio, and Enrico Santamato, "Polarization pattern of vector vortex beams generated by q-plates with different topological charges," *Applied optics* **51**, C1–C6 (2012).

[59] Filippo Cardano, Ebrahim Karimi, Lorenzo Marrucci, Corrado de Lisio, and Enrico Santamato, "Generation and dynamics of optical beams with polarization singularities," *Optics express* **21**, 8815–8820 (2013).

[60] Charles W. Clark, Roman Barankov, Michael G. Huber, Muhammad Arif, David G. Cory, and Dmitry A. Pushin, "Controlling neutron orbital angular momentum," *Nature* **525**, 504 (2015).

[61] Nathan Isgur, Gabriel Karl, and Do W. L. Sprung, "Neutron charge form factor in a quark model with hyperfine interactions," *Physical Review D* **23**, 163 (1981).

[62] Anthony W. Thomas, S. Theberge, and Gerald A. Miller, "Cloudy bag model of the nucleon," *Physical Review D* **24**, 216 (1981).

[63] J. J. Kelly, "Simple parametrization of nucleon form factors," *Physical Review C* **70**, 068202 (2004).

[64] Gerald A. Miller, "Charge densities of the neutron and proton," *Physical Review Letters* **99**,112001 (2007).

[65] Gerald A. Miller, "Electromagnetic form factors and charge densities from hadrons to nuclei," *Physical Review C* **80**, 045210 (2009).

[66] John David Jackson. *Classical electrodynamics*. John Wiley & Sons, 2007.

[67] William T. M. Irvine and Dirk Bouwmeester, "Linked and knotted beams of light',' *Nature Physics* **4**, 716 (2008).

[68] Colin Conrad Adams. *The knot book: an elementary introduction to the mathematical theory of knots*. American Mathematical Soc., 2004.

[69] Benjamin Bode, Mark R. Dennis, David Foster, and Robert P. King, "Knotted fields and explicit fibrations for lemniscate knots," *Proceedings of the Royal Society A* **473**, 20160829 (2017).

[70] Mark R. Dennis and Benjamin Bode, "Constructing a polynomial whose nodal set is the three-twist knot 52," *Journal of Physics A: Mathematical and Theoretical* **50**, 265204 (2017).

[71] Jonathan Leach, Mark R. Dennis, Johannes Courtial, and Miles J. Padgett, "Vortex knots in light," *New Journal of Physics* **7**, 55 (2005).

[72] Robert Fickler, Radek Lapkiewicz, William N. Plick, Mario Krenn, Christoph Schaeff, Sven Ramelow, and Anton Zeilinger, "Quantum entanglement of high angular momenta," *Science* **338**, 640–643 (2012).

[73] Robert Fickler, Radek Lapkiewicz, Sven Ramelow, and Anton Zeilinger, "Quantum entanglement of complex photon polarization patterns in vector beams," *Physical Review A* **89**, 060301 (2014).